Silk fibroin nanostructured materials for biomedical applications

A dissertation submitted by

Alexander N. Mitropoulos
B.S. Biomedical Engineering, Tufts University 2010

In partial fulfillment of the requirements for the degree of

Doctor of Philosophy
in
Biomedical Engineering

Tufts University
Medford, MA, USA

May 2015

© 2015, Alexander N. Mitropoulos

Research Committee:

Prof. Fiorenzo Omenetto
Tufts University, Department of Biomedical Engineering
Prof. David L. Kaplan
Tufts University, Department of Biomedical Engineering
Prof. Marc Hodes
Tufts University, Department of Mechanical Engineering
Prof. Ann M. Anderson
Union College, Department of Mechanical Engineering

Abstract

Nanostructured biopolymers have proven to be promising to develop novel biomedical applications where forming structures at the nanoscale normally occurs by self-assembly. However, synthesizing these structures can also occur by inducing materials to transition into other forms by adding chemical cross-linkers, changing pH, or changing ionic composition. Understanding the generation of nanostructures in fluid environments, such as liquid organic solvents or supercritical fluids, has not been thoroughly examined, particularly those that are based on protein-based block-copolymers. Here, we examine the transformation of reconstituted silk fibroin, which has emerged as a promising biopolymer due to its biocompatibility, biodegradability, and ease of functionalization, into submicron spheres and gel networks which offer applications in tissue engineering and advanced sensors. Two types of gel networks, hydrogels and aerogels, have small pores and large surface areas that are defined by their structure. We design and analyze silk nanoparticle formation using a microfluidic device while offering an application for drug delivery. Additionally, we provide a model and characterize hydrogel formation from micelles to nanoparticles, while investigating cellular response to the hydrogel in an *in vitro* cell culture model. Lastly, we provide a second model of nanofiber formation during near-critical and supercritical drying and characterize the silk fibroin properties at different drying pressures which, when acting as a stabilizing matrix, shows to improve the activity of entrapped enzymes dried at different pressures. This work has created new nanostructured silk fibroin forms to benefit biomedical applications that could be applied to other fibrous proteins.

Acknowledgments

This is for you. To my grandmothers, Eleanor McBride and Venitia Mitropoulos, who were always there with warm smiles. To my mom, Maureen Mitropoulos, who supported me through this endeavor. To my father, Nicholas J. Mitropoulos, who handled my frustration. To my brother Tim, who believed in me and told me to keep looking 20 feet ahead.

For my older brother Chris.

"Remember, no man is a failure who has friends." - It's a Wonderful Life
"The real voyage of discovery is not in seeking new landscapes, but in having new eyes."
　　-Marcel Proust

Table of contents

List of Tables

List of figures

<u>**Chapter 3**</u>

aggregation of silk molecules during sol-gel transition resulted in an increase in the average particle size to 42 nm. The average particles diameter of the forming gels was also found to be dependent on the initial concentration of the silk solution (inset figure). c) SEM micrographs of the silk fibroin hydrogel revealed a nanostructured material, with morphological features of less than 100 nm. d) μRaman spectroscopy of silk fibroin solution and of silk fibroin gels depicted their amorphous (Amide I centered at cm^{-1} and Amide III centered at   cm^{-1}) and crystalline (Amide I centered at cm^{-1} and Amide III centered at   cm^{-1}) structure, respectively 76

Nanostructured materials

There is a need in biomedical engineering to advance current technologies to improve the quality of medicine. Improving the fields of sensing, tissue growth, and chemical delivery is where biomedical research is primarily focused. To improve these areas, topics such as a material's morphology, biology, and chemistry are studied which provides information about a material's structure, cell interaction, and composition respectively. Morphology is one specific topic that has been examined to improve current technology, specifically when using materials that interact with biological systems. Improving the morphology at length scales that are more favorable to cells and molecules (micro to nano) allows for improvement of such materials.

Controlling morphology at the nano length scales is one area to improve biomedical engineering and it determines a material's structure. Forms, such as porous membranes, ordered arrays, wires, and crystalline materials, are some nanostructures that are currently studied for biological applications. Researchers have focused on perfecting the order and orientation of nanostructures for electronic and photonic applications that require long-range arrangement. Additionally, current research also examines finding methods to easily synthesize nanostructures found in a material's bulk.[1] Combining synthesis and orientation to make nanomaterials would improve their morphology for advanced uses for biomedical purposes.

Cells respond to a material's structure at both the micrometer and nanometer scales but general methods of forming structures on both scales are limited. To overcome the

importance of nanostructures, researchers use biomaterials and biopolymers, which offer the chemical composition necessary for biomedical applications. Nanostructured materials are normally based on the self-assembly of block-copolymers to produce new material forms, thereby changing material function.[1] The local fluid condition is a defining feature influencing the nanostructure of block-copolymers while also determining molecular organization. Variables such as temperature, pressure, solvent concentration, and ion concentration are major factors that change fluid conditions thereby influencing the molecules' structure.[2] These variables change the fluid interaction with a suspended polymer and induce modifications such as molecular folding stimulating nanostructure formation resulting in bulk transformed material states.[3] Finding methods to alter the fluid conditions around a material efficiently can be used to easily design the necessary nanofeatures in biopolymers to improve the effectiveness of certain applications.

Materials with nanometer features are becoming increasingly important in biomedical engineering because they offer high surface areas that are difficult to fabricate using conventional techniques.[4–7] The physical structure of a biomaterial is known to be an important factor in cell response. Materials with nanometer features have been explored to improve cell performance since materials organized on several length scales (micro to nano) bear closer resemblance to physiological conditions.[8] Therefore, considerable effort has been made to produce dimensions in biocompatible and biodegradable materials at the nanoscale. Additionally, materials with nanometer features have higher surface area compared to other materials. Therefore, these materials can be used as

sensitive detection platforms because the high surface area improves the responsiveness of a sensor that detects analytes by interacting with molecules on its surface.[7,9]

Fluids determining nanostructured materials

Block-copolymers are materials that depend on their surrounding environment.[10] When considering a molecule, its relationship with the surrounding variables such as concentration and fluid conditions should be evaluated to understand non-covalent self-assembly. The fluid condition provides a basic insight to the construction of nanometer-sized features for new material forms.[10,11] Numerous fibrous proteins (that are block-copolymer like) act as structural building entities, and research has been focused on self-assembling these proteins into engineered functional materials. Fibrous proteins fold into determined secondary structures (beta-sheets and alpha-helices) to distinguish their assembly and improve a material's order.[11] One method to induce determined secondary structures in a protein is by changing the fluid conditions, such as concentration, temperature, ionic concentration, or pH. This can refold the protein molecule and prompt it from a primarily liquid favorable state to a more favorable solid state. **Figure 1** summarizes possible transformations of polymers, all which occur by changes to the fluid environment.
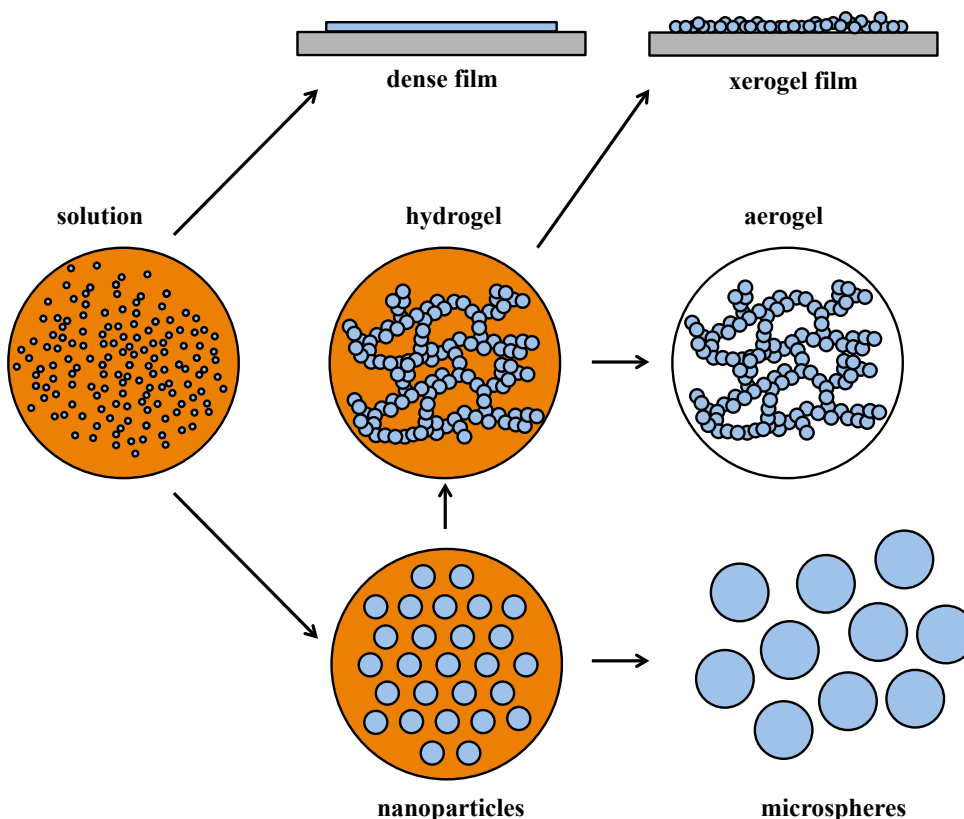
Figure 1. Schematic representation of possible polymer forms induced by changes to the fluid environment.

Fluids are the most important component in a protein's environment because they assist with the movement of ions and the assembly of secondary structures.[12] Liquid water is the major environmental factor in biological systems controlling partial protein refolding determined by variables such as water temperature, pressure, viscosity, surface tension, and dielectric constant.[13] Most proteins maintain a water shell around the molecules resulting in varying degrees of hydration and amino acid folded cavities. This water shell causes imperfect packing in the protein interior and determines protein conformations.[12] Liquid water can change the shape of the protein as depicted in **Figure**

2 separating areas of the protein from the bulk.[12] Therefore, altering the water shell around a protein can change its folded structure into (sometimes) irreversible forms.[12]
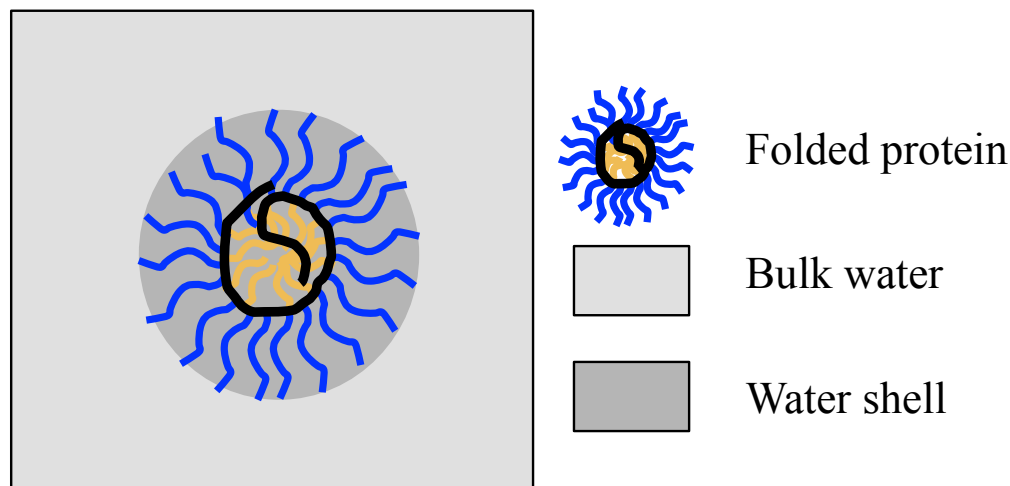
Figure 2. Schematic representation of a protein surrounded by its water shell. Modified from reference [8].

Near-critical and supercritical fluids are states of a material that occur when the pressure and temperature are near or above its critical point respectively. Supercritical fluids offer unique physiochemical properties such as the absence of surface tension allowing supercritical fluids to completely contact structures with micro- and nano-pores to prevent framework collapse. Carbon dioxide (CO_2) has emerged as an attractive material for regenerative medicine in the fields of pharmaceutical, food science, and biomaterials. Processing materials with near-critical or supercritical CO_2 leads to a solvent free product with high purity.[14,15] Supercritical CO_2 is one of the most used supercritical fluids because it is low cost and environmentally benign compared to volatile organic materials and ozone-depleting substances while also capable of solubilizing organic molecules with low polarity.[16,17] Supercritical fluids interact with

polymers in unique ways and can act as a porogenic agent to dissolve amorphous and semi crystalline materials.[18] Nevertheless, near-critical and supercritical fluids interact with polymers (particularly proteins) similarly to other fluids because they fully contact the surface of the polymers resulting in folding changes. Other methods of protein folding can be induced by variables such as pressure, pH, and electrical stimulation. However, pressure offers unique properties that are unobserved in natural conditions.

Pressure on nanomaterials

Pressure is a powerful tool to study the effects of folding and the role of folding intermediates on biopolymers.[12,19,20] The physical variables can induce structural changes to proteins, particularly regarding their function, where high-pressure can perturb macromolecules in solution without causing complete denaturation.[19] Conformational changes in proteins under pressure are similar to changes associated with temperature or treatment with liquid solvents but is more tunable since high pressure can be easily removed.[19,21]

Understanding the role pressure has on polymer chain mobility which results in structural changes would produce protein forms never observed before. Altering pressure conditions to proteins normally does not occur because extreme pressures are uncommon in biological systems. However, research conducted on aquatic life at the bottom of the ocean where pressure is a critical factor has recently examined protein structures to better understand folding and development.[12,22] The morphological changes while using supercritical fluids would not otherwise be observed or discovered with other processing conditions, and it is an interesting variable to treat proteins.

Supercritical fluids occur at pressures much higher than ambient conditions compared to other fluids, which can have an effect on protein secondary structure.[23] Additionally, adding a small amount of compressed gas to a polymer has shown to change its physical properties.[23] Previously researchers believed hydrostatic pressure was the only factor responsible to change the glass transition temperature of a material. However, supercritical CO_2 is a solvent that reduces polymer melt viscosity through thermodynamic effects due to intermolecular interactions between the supercritical CO_2 and the polymer.[23,24] The depression of the glass transition temperature caused by the addition of CO_2 has been investigated with many polymers, and it was shown to change the polymers' crystallization rate while assisting to form nanostructured materials.[21,25,26]

Discussion

The potential for nanostructured materials should be developed for applications in the fields of medicine, energy, electronics, and the environment. The benefits of nanotechnology can be tailored to make essential structures in materials efficiently stronger, lighter, more durable, more reactive, more sieve-like, or better electrical conductors.[1] While the past decade has seen significant advances in scientific applications regarding nanostructured materials, new processing methods on known materials, particularly biomaterials, are necessary to expand and develop new forms. Nanostructured biomaterials brought about by fluid and pressure induced transformations can be used to better produce macrostructures in polymers, particularly those based on fibrous proteins. To improve biomedical applications, nanostructured materials should be developed using biopolymers that can easily degrade and change material morphology.

Biomaterials/Biopolymers

Biomaterials, such as biopolymers, are natural or synthetic substances designed to interact with biological systems to direct medical treatment.[27] Biopolymers possess significant potential because their chemistry gives rise to materials with physical and mechanical diversity.[27] Biopolymers, particularly degradable biopolymers, have been extensively studied due to the diverse populations of potential materials based on their unique chemistries. In addition, generating nanostructures in several different forms offers versatility to these materials benefitting from their unique chemical structure for biomedical applications.

Degradable polymers are of special interest because these biomaterials can be broken down and excreted or resorbed by the body. Structural biomaterials must have the appropriate mechanical properties, produce nontoxic degradable products, degrade at times coinciding with function, and not induce an inflammatory response.[27] These interests are determined by the material's chemical composition, crystal structure, hydrophobicity, and surface charge.[27,28] Although studies indicate that mimicking microporosity and fibrous structures of the extra-cellular matrix (ECM) could improve the biocompatibility of different biomaterials, there are few ways to fabricate suitable nanostructures in bulk simultaneously in these materials.

The processing condition applied to biopolymers causes a transition in the material structure and creates the individual material forms. The change in structure occurs by changing the fluid conditions causing aggregation producing more favorable solid states.

These processing methods produce forms with more favorable nanostructures that can benefit specific biomedical applications.

Nanoparticles

Biodegradable nanoparticles are material forms that provide a compatible matrix for encapsulation and controlled release of drugs. Nanoparticles are useful in biotechnology because they are small enough to effectively travel through tissue, can enter cells to delivery a specific payload, have high surface area to volume ratio, and are easily injectable.[29] Control of particle diameter and dispersion are two important parameters that are considered when synthesizing particles for pharmaceutical applications because the size and dispersion control the drug release rate. It is well known particles made from polymers can be scavenged by organs of the reticuloendothelial system, and it is the diameter of these particles that makes them prone to removal.[30] Different natural and synthetic materials have been explored to make nanoparticles using several formation methods to control monodispersity and particle diameter.

Nanoprecipitation

Nanoprecipitation is one method to form nanoparticles due to its simple approach and gentle formation.[30] Nanoprecipitation occurs by the bulk mixing of different liquids where a polymer in one of the solutions precipitates when it contacts the second fluid. The shape of the particles are normally spherical during precipitation because the polymer is distributed homogeneously throughout the solution.[31] Precipitation occurs from nucleation of individual molecules that continue to grow into larger particles which

stops as soon as colloidal stability is reached.[31] The resulting size is strongly correlated to the polymer concentration and viscosity of the solution, which should prevent the entanglement of polymer chains between particles to prevent the continued growth of the nanoparticles by Ostwald ripening.[31] Precipitation use strategies to exploit the partial miscibility of polymers between the polymer solution and the mixing fluid resulting in particle growth caused by the interfacial turbulence generated during solvent displacement.[32,33] This desolvation can occur via organic fluids or interactions from other polymers inducing particle formation.

Nanoparticles synthesized by microfluidic technology

Microfluidic devices have previously been shown by several researchers to synthesize micron and submicron particles through the formation of controlled emulsions.[30,32] Microfluidics devices use a method that depends on hydrodynamic instability taking advantage of predictable breakup of co-flow systems to break polymeric solutions into droplets. This forms micron and submicron diameter droplets that are normally crosslinked by the continuous fluid.[30,32,34] Additionally, microfluidic devices have proven useful in the generation of monodisperse droplets and particles made of block-copolymers. They offer better advantages compared to random polymers because block-copolymers easily form more predictable droplet diameters. Consistent sized droplets can be formed and tuned using a variety of different microfluidic geometries leveraging the technology of discrete and continuous systems to produce monodisperse polymeric spheres.[35]

<u>Discussion regarding nanoparticles</u>

Submicron- and nano-particles form best using biopolymers made from linear blocks because the molecules interact more efficiently producing organized secondary structures for easier control of particle size.[29] Nanoprecipitation is a simple method to produce relatively tunable size spheres. However, it can also lead to aggregation and gelation depending on the polymer concentration. Combining biomaterials with microfluidic systems controls particle size and dispersity while also using small volumes offering tunability over particle diameter. Additionally, microfluidic systems can be used in parallel with small footprints to generate particles made from different biopolymers.

Nanoparticles are made from a range of different materials all with unique chemistries making them more compatible to deliver different drugs. Several synthetic and natural polymers have been examined yielding different biological responses, different diffusion properties, and different degradation rates. However, nanoparticles are not the only configuration these materials can form. Depending on the processing conditions, such as during fluid exchanges, these materials can aggregate into networks composed of entangled spheres forming gel structures surrounded by water producing structures known as hydrogels.

Hydrogels

Hydrogels hold great promise for the future of biomaterials because they are capable of forming stabile nanostructures in hydrated states.[36] Gels are materials made by transitioning from a solution (sol) to a gel with the main features being high porosity and small skeletal dimensions.[37] The sol-gel process is motivated by generating gels with

potentially higher purity and homogeneity to control the surfaces and interfaces of materials during the earliest stages of formation.[38] Understanding and controlling either the synthesis chemistry or the polymer interactions are important conditions that need to be examined when producing hydrogels.

Despite the utility of hydrogels, their formation mechanism is still poorly understood.[39] Nevertheless, hydrogel formation is believed to be based on intra- and interchain contacts that form junction points in the molecular network surrounding the pore solvent while at the same time preventing precipitation.[39] Normally, liquid precursors are mixed together and interact at the molecular scale resulting in particle nucleation, particle growth, and particle entanglement forming solid networks.[38,40,41] Block-copolymers that consist of relatively short spacer blocks surrounded by hydrophobic blocks form high ordered aggregates and are more favorable materials compared to randomly arranged polymers.[36,42] Under the appropriate conditions of pH, concentration, and temperature, protein polymers can adopt different conformations that expose specific residues to the surface resulting in more uniform gelation and more mechanically robust hydrogels.[43,44]

Hydrogels are an attractive form for tissue engineering applications because they have the necessary feature sizes for cells while maintaining hydration under physiological conditions.[43,45–48] The high hydration and pore structure make hydrogels ideal forms for tissue scaffolds. Due to these characteristics, several natural and synthetic biopolymers have been turned into hydrogels including collagen,[49–53] fibrin,[54] alginate,[42,55] polyethylene glycol (PEG),[56] and polyvinyl alcohol (PVA).[57] Generating hydrated porous structures in different materials utilizes the chemical make up of the material with the

physical properties associated with the hydrogels. However, there are few options for biomaterials that match the nanostructure of native tissue, while also being degradable, biocompatible, and suitable for cell growth without the possibility of toxicity or infection. Therefore, examining hydrogels made from several different materials is necessary to understand their positive and negative characteristics.

Collagen

Collagen is one of the most abundant proteins found in the human body used as a structural material found in mammalian tissues including skin, bone, cartilage, tendon, and ligament.[43,49] Collagen is used for FDA-approved matrices for wound healing in fibrillar extracellular microenvironments because it surrounds cells and is comprised of molecular signals. Collagen purified from natural sources compared to recombinant sources is better because it contains the inherent biological properties such as cell recognition, receptor-binding ligands, triggered proteolytic degradation, and remodeling used for tissue scaffolds.[58] Purified collagen represents a valuable material to form tissue scaffolds because it offers similar biological function compared to its natural counterpart. The efficient attachment of cells to collagen hydrogels makes them ideal for tissue culture since many cell types easily attach to the surface. Additionally, collagen can be altered by chemical modification to improve cell attachment and improve its physical properties such as by chemical cross-linking with glutaraldehyde.

The structure of collagen is a triple-helix of parallel left handed polyproline II-type helices.[59] The tight packing of helices mandates that every third residue is glycine. Individual collagen triple-helices assemble into a complex hierarchical manner that leads

to the macroscopic fiber network observed in tissues.[59] One of the derivatives of collagen, gelatin, is formed by altering the helix structure into a single strand that turns into a hydrogel by altering the temperature allowing it to be used for many tissue engineering applications.[43]

For specific applications, collagen hydrogels have been used for ocular repair and connective tissue. Collagen hydrogels have been used to replace the cornea, the transparent extracellular matrix of the eye's anterior surface which is composed of three layers.[49] Furthermore, collagen's structural integrity due to its fibrous nature make it useful as load bearing tissue scaffolds.[27] Collagen hydrogels have been used as ligament scaffolds due to their ability to withstand high tensile loads while its elastic behavior makes it useful for cartilage and skin.[49]

The chemical composition, regarding the primary amino acid sequence and the secondary and tertiary folding of collagen, makes it one of the most ideal biomaterials for structural repair. However, purification and consistency of collage-based materials increases its cost as a successful material. Additionally, since collagen composes ~70% of mammals, remodeling and deposition of new collagen occurs frequently and easily. Despite the advantages of collagen as a biomaterial for tissue engineering scaffolds, issues regarding mechanical properties and the rate of tissue remodeling have spurred the development and use of other materials.

Fibrin

Fibrin is a critical component in blood and is responsible for clotting making it an ideal material to form hydrogels because it forms a solid gel network in a liquid

environment. Fibrin plays a critical role in wound healing for use as a sealant to promote wound closures.[27] Fibrin is composed of two sets of polypeptide chains joined together by disulfide bridges formed after thrombin-mediated cleavage.[54] The covalent cross-linking produces a stable network that is resist to protease degradation. Fibrin hydrogels have been widely used in tissue engineering applications including engineering of adipose, cardiovascular, ocular, muscle, skin, cartilage, and bone tissues.[27] Additionally, fibrin has been used clinically in cardiac, liver, and spleen surgery as a hemostatic agent. However, fibrin as a hydrogel scaffold has low mechanical stiffness and rapidly degrades in vivo.[27,54] Furthermore, fibrin needs to be combined with other materials to obtain the desired strength to improve the mechanical properties making it less ideal as a biomaterial. Therefore, due to these possible drawbacks, other non-mammalian materials have been studied and researched.

Alginate

Another natural material used for tissue engineering is alginate which forms hydrogels efficiently.[55] As a biomaterial, alginate has favorable properties including biocompatibility, easy chemical modification, and gentle gelling offering easy encapsulation of substances to be used as a drug delivery vehicle. Alginate hydrogels are widely used in the food industry as a stabilizer because of its interaction with proteins and fats. Alginate has also been shown to interact in a favorable manner *in vivo* and has been utilized as hydrogel scaffolds for tissue engineering.[42]

Alginate is a linear polysaccharide copolymer of linked beta-D-mannuronic acid and alpha-L-guluronic acid monomers. The monomers are sequentially distributed in either

repeating or alternating blocks, and the amount and distribution depends on the seaweed species.[42] Alginate hydrogels are formed by cross-linking with cations interacting with the carboxylic groups forming ionic bridges between polymer chains forming nanostructures leading to gelation.[42,55] The mechanical properties and pore size can be manipulated by varying the molecular weight and ratio of mannuronic acid and guluronic acid monomers.[42] Alginate hydrogels have been prepared using a wide range of molecular weights, which changes the gel stiffness.

However, even though alginate has found several uses as a biomaterial, it degrades by hydrolysis that depends on its molecular weight and the number of exposed sites facilitating the degradation rate. Even alginate cannot match the necessary physiological conditions compared to collagen, fibrin, and other natural materials capable for tissue engineering applications. Therefore, other materials are necessary that have more consistent mechanical properties that match the desired purpose and degrade at rates coinciding with function.

Synthetic hydrogels

Synthetic hydrogels offer more advantages compared to natural hydrogels because their chemical composition is a repeating and their mechanical properties can be adjusted to match function.[27] Over the last few decades polymer hydrogels have been extensively studied as cellular scaffolds because of their porous network and efficient exchange of small molecules with the surrounding liquid environment.[56] The synthesis to produce these polymers is well controlled making them ideal to form reproducible hydrogels with consistent chemical and mechanical properties.

Polyethylene glycol (PEG)

One synthetic material that has been explored as a hydrogel for repairing and regenerating tissues is polyethylene glycol (PEG). Synthetic polymers such as PEG have emerged to modulate specific cell responses regarding mechanical properties and chemical surface modifications for biomedical engineering.[56,60] PEG has been regarded as an important hydrophilic polymer for biomedical applications for drug delivery and tissue engineering because of its biocompatibility, resistance to protein absorption, and low immunogenicity.[60] PEG hydrogels have lead to the fundamental knowledge of cell/scaffold interactions evaluating material design and fabrication approaches to develop bioactive hydrogels for tissue engineering.[60] These studies have examined significant information regarding potential hydrogel features and mechanical properties to optimize cell growth.[42,61]

Poly(vinyl) alcohol (PVA)

Poly(vinyl alcohol) (PVA) is another synthetic biomaterial obtained by alcoholysis, hydrolysis, or aminolysis of poly(vinyl acetate).[43] PVA hydrogels have been used for numerous biomedical and pharmaceutical applications because they are non-toxic, non-carcinogenic, and bioadhesive. PVA hydrogels are capable of simulating natural tissue and are easily accepted into the body as soft tissue replacements. Some replacement tissues include articular cartilage, artificial skin, artificial pancreas, and the lining of artificial hearts.[57,62]

One type of PVA hydrogel has mechanical properties that are highly elastic. These hydrogels are formed by freeze/thawing the polymer solution. This process offers more advantages compared to other crosslinking methods such as glutaraldehyde, acetaldehyde, and formaldehyde because it prevents the release of these toxic chemical cross-linkers.[57] However, even with this disadvantage, cross-linked PVA hydrogels show high tensile strength and high oxygen permeability.[63] Additionally, the surface of PVA can be modified with oligopeptides to enhance cell interaction and be used in tissue engineering as artificial cartilage or as cornea substitutes due to PVA's transparency in the visible region.[43] However, PVA hydrogels are useful for permanent implantable scaffolds since PVA is not degradable under physiological conditions and it is difficult to form hydrogels *in situ*.[27] Even though PVA has numerous biomedical and pharmaceutical applications, it is less ideal compared to other synthetic materials used for implantable devices because the body is capable of fully replacing degradable biopolymers for current biomedical applications.

Material	Natural/ Synthetic	Gelation Mechanism	Uses/ Applications	Ref
Collagen	*Natural*	Temperature Δ pH glutaraldehyde	• Liver repair • Skin repair • Blood vessels • Cornea	49–53
Fibrin	*Natural*	Fibrinogen and thrombin	• Adipose tissue • Ocular tissue • Muscle tissue • Liver tissue • Skin tissue • Cartilage tissue • Bone tissue	54
Alginate	*Natural*	Addition of Ca^{2+} Addition of Ba^{2+}	• Bacterial culture material • Food additive	42,55
Polyethylene glycol	*Synthetic*	Cross-linking	• Cell culture material	56,61

		Cross-linking agents	• Tissue mimic	
Poly(vinyl alcohol)	*Synthetic*	Cross-linking agents • Glutaraldehyde • Acetaldehyde • Formaldehyde Freeze/thaw cycle Electron beam γ-irradiation	• Contact lens • Drug delivery • Food additive • Artificial heart • Soft tissue replacement • Articular cartilage • Catheters • Artificial skin • Artificial pancreas • Hemodialysis membrane	43,57,62–64
Silk	*Natural*	Sonication Δ pH Shear Δ temperature electrogelation	• Soft tissue • Articular cartilage • Neural tissue • Fat tissue	65–70

Table 1. List of hydrogel materials and gelation mechanism with uses and applications.

Silk fibroin hydrogels

Recent studies have shown silk fibroin as an ideal candidate for hydrogel systems due to its fibrous protein composition, controlled rate of degradation, and ability to gel by different mechanisms.[65–70] Due to the liquid nature of reconstituted silk fibroin, gelation can occur via many different routes such as changes in electric field, changes in pH, or via shear. Each synthesis provides a different structure to the silk fibroin offering different mechanical properties and dimensions via the sol-gel transition. Silk is an ideal material to form into a hydrogel because of the chemical structure of silk, its ability to tailor to appropriate mechanical properties, produce non-toxic degradable products, degrade at a rate coinciding with function, and its ability to efficiently stabilize biological dopants.

Discussion regarding hydrogels

Several materials have been used to make hydrogels from natural and synthetic sources. Hydrogels are useful forms for tissue engineering because their mechanical properties can be tailored to match specific tissues while remaining hydrated, which are important physiological conditions for cell attachment. Hydrogels offer a solid support in a highly porous material to allow the infiltration of cells regardless of whether the material originated from natural sources or was synthetically created. Naturally derived macromolecules are beneficial in biology because they are biocompatible, degradable, and have the intrinsic surface chemistry resulting in innate cellular interactions.[42,43] However, natural materials exhibit per batch variation and have a narrower mechanical limit compared to synthetic materials that can be controlled to exhibit precisely ordered structures and functions. Even with the controllable mechanical properties depending on cross-linking and molecular weight, synthetic polymers produce unwanted degradable byproducts or do not fully degrade. The amino acid sequence that makes up natural materials, such as collagen and fibrin, is a defining feature for the success of these hydrogels because the chemical sequence and specific protein folding benefit and assist with cell attachment. Combining these specific protein materials with controlled processing methods to form nanostructures, microstructures, and macrostructures produces hydrogels that match the physical and physiological conditions needed for optimal biological applications.

Aerogels

Distinctive gel drying methods have been designed to prevent damage and changes to solid gel networks to create high surface area nanostructured materials.[37,71–73] Removing the pore liquid from a gel without altering the solid network by interfacial forces is challenging and requires conditions at different fluid phases to maintain the gel structure and prevent pore collapse (**Figure 3a**). One method to remove the pore liquid that does not involve a liquid/vapor phase boundary is freeze-drying. The removal of water by freeze-drying is a two-step process that brings gels to very low temperatures followed by pore fluid removal by sublimation. Freeze-drying is widely used for thermosensitive products mainly in pharmaceuticals.[37] Even though freeze-drying is a successful method to remove the liquid from a gel, it is energy intensive and time consuming for complete liquid removal. Additionally, the freezing step destroys the fragile gel structure because of a density change in the pore liquid (normally water) during solidification resulting in structural damage to the gel (**Figure 3b**). For hydrogels composed of water, there can be a 9% volume increase during ice formation.[37]
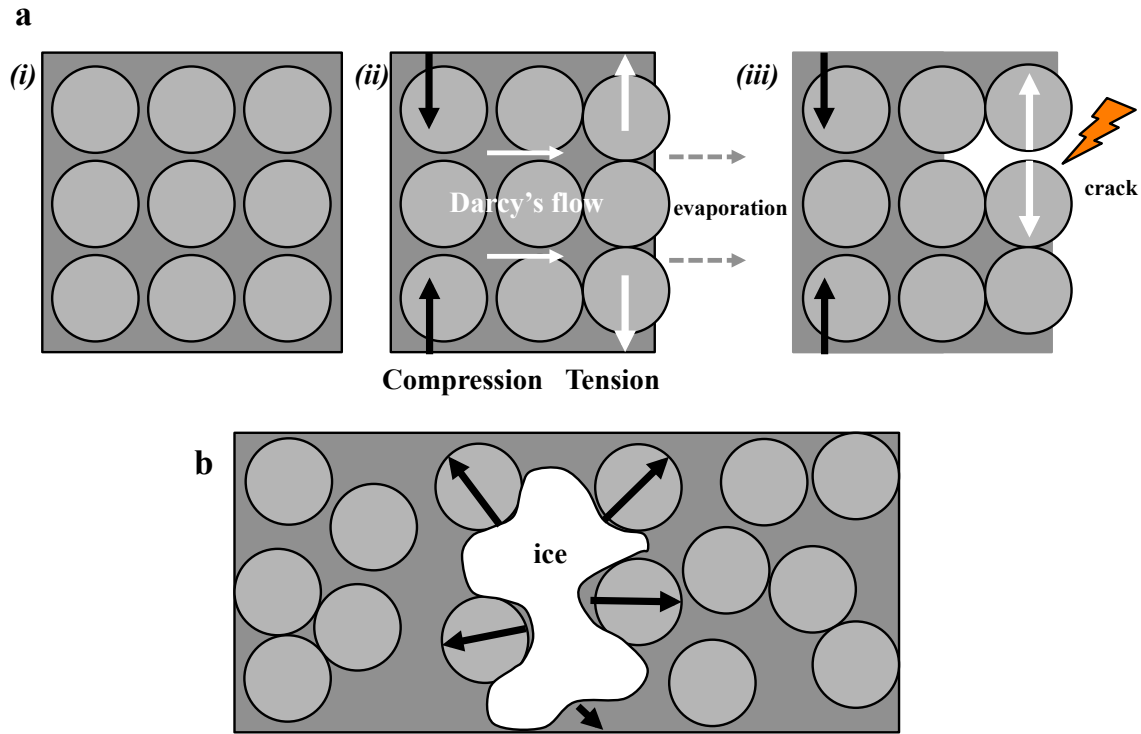
Figure 3. The mechanisms during convective drying and freeze-drying. a) (i) A solid gel matrix composed of particles loses its pore fluid via (ii) evaporation resulting in compression and tension causing (iii) structural damage to the solid skeleton. b) Damage to a particle based hydrogel from the formation of ice crystals. Modified from [34].

One method to remove liquids from gels that prevents crossing the liquid/gas phase boundary is supercritical drying. Supercritical drying is a method to maintain the fragile structure of gels and prevent pore collapse associated with evaporative drying.[17] The high surface area achieved after supercritical drying exploits the chemical inertness and mechanical stability of the material and is a method to fabricate highly porous materials known as aerogels.[5,7,14,17,18,37,74,75] Unlike freeze-drying, which requires materials to cross two phase boundaries (freezing followed by sublimation), supercritical drying consists of conditioning a gel until the pressure and temperature exceed the critical point of the entrapped fluid.[37,73] At temperatures and pressures above the critical point, known as the

supercritical region, no phase boundary exists between liquid and gas (**Figure 4**).[37] This prevents the formation of liquid-vapor meniscuses at pore regions where mechanical tensions induced by capillary forces can break the solid skeleton while replacing the liquid with a gas.[37] The aerogels that are generated by this process have an extremely low-density and a large inner surface area that contain cavities and channels that are deeper than they are wide.[7]
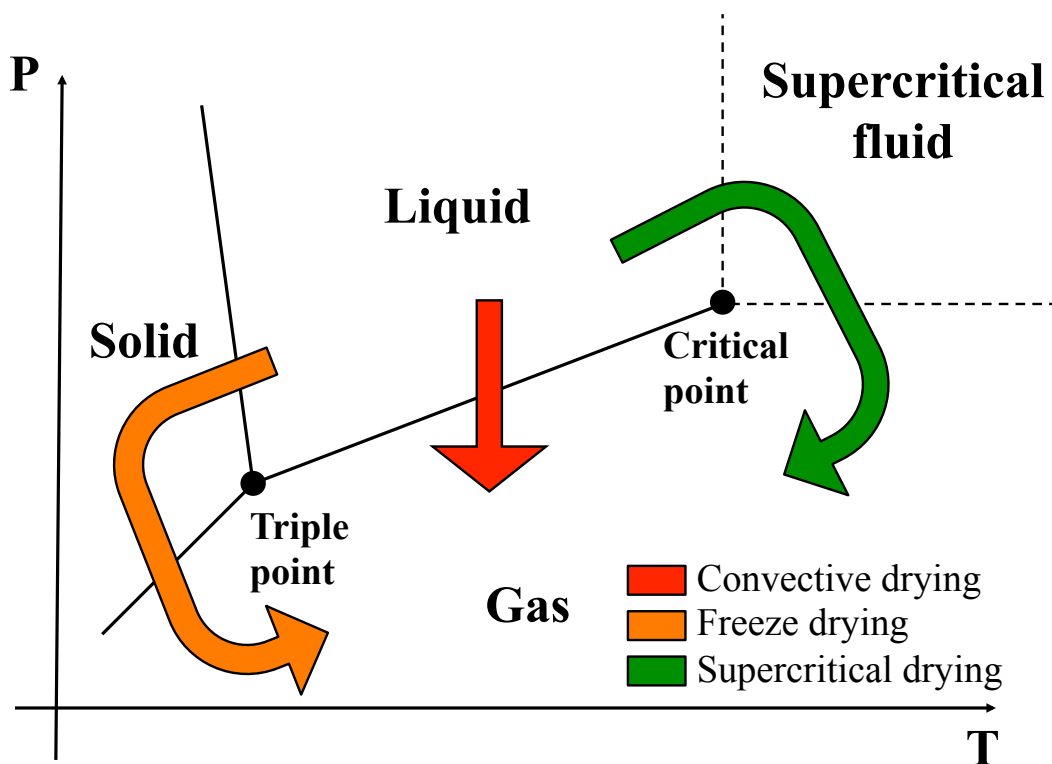
Figure 4. Phase diagram depicting possible routes of drying.

Dry gels have outstanding physical properties determined by their solid nanostructure. The following properties only apply to aerogels after supercritical drying because they have the highest porosity that cannot be made by other drying methods.[37] Aerogels have the highest surface area and lowest density of all solid materials, which

can be varied depending on the initial gel synthesis. Aerogels have large inner surface area per gram of material making them ideal as catalyst supports for liquid and gas sensing because a functionalized surface will be easily contacted by analytes. Additionally, the low density of aerogels offers materials with low refractive indices and low dielectric constants because up to ~90% of an aerogel is a gas thereby lowering the material's bulk properties.[37]

Highly porous gels have a number of potential applications because of their unique physical properties, as briefly mentioned above. Over the past few decades there have been specific applications to utilize low density and high surface area materials, and developing aerogels made from different materials can create opportunities that have not been previously considered. The most important and largest commercial application for aerogels is thermal insulation.[37] Additionally, aerogels are suitable materials because of their low electrical resistance. If the voids of an aerogel are filled with an electrolyte, a super-capacitor can be formed making the device suitable for bridging short power failures.[37] Furthermore, aerogels can be used for high-performance liquid chromatography and catalysis based on the tunable microstructure exhibiting high internal surface area. The major physical properties of aerogels and their applications are highlighted in **Table 2**.

Physical property	Application
High porosity/low density	• Sound insulation • Catalysis • Sensors • Fuel storage • Ion exchange • X-ray lasers
High surface area	• Chromatography • Sensors

Low thermal conductivity	• Thermal insulation • Transparent windows • Coatings for solar heat collectors • High temperature storage • Low temperature storage • Space technology
Low refractive index	• Chernkov detectors • Optical coatings • Lightweight optics • Light guides
Low dielectric constant	• Electrodes for supercapacitors • Spacer vacuum for electrodes • Dielectrics for ICs • Desalination
Mechanical properties	• Energy absorber • Hypervelocity particle trap • Space science

Table 2. Identification of aerogel properties, features, and their applications. [23,25,71].

To date, aerogels have been made from several different materials including silica,[76–79] resorcinol-formaldehyde,[80–84] cellulose,[85–92] and chitosan.[93,94] Each aerogel offers a unique technological advantage relating to its chemical structure combined with the physical properties of aerogels. Currently, aerogels have been used for applications such as catalyst supports, chemical sensors, particle detectors, thermal insulation, energy absorbers, drug delivery vehicles, and tissue scaffolds.[5,7,95] Below are some common aerogel materials and their applications.

Silica

Silica was one of the first known materials formed into aerogels, and it has been studied extensively since its discovery in 1931 by Kistler.[96] Due to their extensive use, the physical properties of silica aerogels are considered as the standards. Silica aerogels typically have low bulk densities around 80 kg/m^3, porosity of 90% or more, and a

surface area as high as 1000 m^2/g.[76] Silica aerogels are prepared in a two-step process resulting in a silica gel skeleton made from the hydrolysis of silicon alkoxide precursors, tetramethoxysilane (TMOS), producing uniform pores ~5-100 nm immersed in ethanol followed by supercritical drying.[78] The pore network and skeletal structure that was defined by the hydrolysis chemistry remains intact after supercritical drying and offers the potential applications mentioned above.

Methods of formation of silica aerogels have been studied significantly and vary depending on the desired application. Depending on the synthesis method, silica aerogels can be made with alterations to pore size, density, and hydrophobicity.[7] Additionally, changing the gelation procedure to silica aerogels can make them hydrophobic to prevent pore collapse in high humidity environments since silica aerogels formed using TMOS are naturally hygroscopic and susceptible to water damage.[7]

Silica aerogels are seen in many different applications ranging from the physical sciences to biology.[6,7,78] However, the most prominent application is in thermal insulation.[7,75] Silica aerogels are used as insulation in space shuttles and space suits, high-energy electronics, and commercial buildings.[7] Due to silica aerogels transparency, monolithic silica aerogels might be used as windows since common glass windows are the largest loss of heat in most buildings.[7] This has not prevented silica aerogels from being looked at for other applications such as tissue scaffolds or chemical gas sensors.[7] Nevertheless, even though silica is an ideal material to make into aerogels, other less brittle organic materials are more beneficial for biomedical applications.

Resorcinol-formaldehyde (RF)

Resorcinol-formaldehyde (RF) aerogels are an important class of organic aerogels and are extensively studied for their use in thermal insulation, catalysis, and as electrically conducting carbon aerogels in energy storage and filtration.[82,83] Organic aerogels and carbon aerogels have received interest due to their controllable properties via the catalyzed reaction mechanism tailoring pore properties.[82] RF aerogels are synthesized by base-catalyzed polycondensation of resorcinol with formaldehyde forming a wet gel followed by supercritical drying.[7]

RF aerogels offer applications as electrodes in supercapacitors and back up power systems because they have a high surface area and are simple to produce. To change and optimize these carbon aerogels for supercapcitor applications, changes in the synthesis parameters have been investigated to alter the mesopores, micropores, and surface area activated by temperature and chemical modification.[7] However, even though RF aerogels are formed from an organic material there is not much discussion using RF aerogels in biological applications.

Cellulose

Cellulose can be prepared as a gel from de-esterfied cellulose acetate cross-linked with acetone.[7,88] Cellulose is an abundant and sustainable organic polymer obtained from cotton, hemp, and wood.[7] Cellulose aerogels represent an organic material made from a biodegradable source combined with the morphology associated with aerogels but offer a different chemical composition and morphology.[85] One of the approaches of making these aerogels is the cross-linking of cellulose species followed by supercritical drying

with CO_2.[7,88] Additionally, the biological nature of cellulose makes these aerogels useful for potential scaffolds for tissue engineering. Therefore, cellulose aerogels represent a highly porous material made from a natural material that can have mechanical properties that exceed the strength of RF aerogels.[7]

Native cellulose can organize into fibrils containing areas of crystalline order intermixed with amorphous regions. However, even though cellulose can be organizing into nanofibers, it requires toxic chemical processing to produce into elementary fibrils to make it suitable for low density, open porous, dry gel networks.[7,88] The chemical process is not environmentally friendly and other materials need to be considered for biological applications.

Chitosan

Another natural material that can be formed into an aerogel is chitosan, a polymer soluble in dilute aqueous acid.[94] Chitosan is an attractive material because it is a natural precursor derived from chitin, a polyglucosamine, which is one of the most abundant organic compounds on earth found in the exoskeleton of insects, the cell walls of fungi and yeasts, and the shells of crustaceans.[93,94] Chitosan is used in current applications including pharmacology, medicine, agriculture, and waste management due to its chemical properties and biocompatibility.[93]

Chitosan was examined for aerogel applications because of its chemical composition and abundance. However, chitosan aerogels have yielded unsuccessful because it contraction and deformation after supercritical CO_2 drying due to the hydrogen bonds formed between adjacent chains in low-density structures. To prevent shrinkage, chitosan

aerogels are made by mixing with silica since both materials are prepared in acidic solutions which is required to catalyze the hydrolysis and condensation of TMOS.[93]

Chitosan is a common biomaterial for cardiovascular devices, but silica-chitosan hybrid aerogels are not compatible with red blood cells and induce hemolysis.[7] Nevertheless, chitosan aerogels are natural materials and maybe ideal candidates as tissue engineering scaffolds. Their high porosity on the order of 80% is difficult to mimic with other biomaterials. However, producing composite aerogels from two degradable substances is better for biological applications.

Material	Gelation Process	Uses/ Applications	Reference
Silica	• Polymerization of siloxane	• Thermal insulation • Sound insulation • Optical coatings • Catalyst supports	5,7,76,78,79,97
Resorcinol-Formaldehyde	• Base catalyzed polycondensation of resorcinol with formaldehyde	• Supercapcitors • Back up power systems • Charge storage	7,80–84
Cellulose	• Calcium thiocyanate • Isocyanate/tin based catalyst	• Precision filtration • Biomedical applications • Filler materials	7,85,88–92,98
Chitosan	• Glutaraldehyde • Glyoxal • Formaldehyde	• Tissue engineered scaffolds • Adsorption/desorption	7,93,94
Silk	• pH induced gelation	• Drug delivery	99,100

Table 3. Identification of aerogel materials and gelation processes with uses and applications.

Silk aerogels

Recently silk aerogels have been synthesized by supercritical CO_2 drying.[99,100] The initial hydrogel to produce a silk aerogel was formed by assisted gelation after pumping CO_2 into a silk solution producing carbonic acid, lowering the pH while foaming the

solution at the same time.[99] Lowering the pH of the silk solution using CO_2 is beneficial compared to conventional mineral acids such as sulfuric acid and hydrochloric acid because it does not require any additional downstream processing to remove the acid components from the gel.[99,101] Silk fibroin aerogels have been used for drug delivery applications which offer a better release rate compared to silk films.[100] For drug delivery applications, the silk aerogels were loaded with ibuprofen after supercritical drying and submerged into phosphate buffered saline solution to determine the release rate. The researchers experimentally showed the formation of silk aerogels and the change in volume of the aerogels after ibuprofen release. However, the control of the porosity and density were not examined and the effect of supercritical CO_2 on the silk manipulation was not considered.

Reconstituted silk fibroin aerogels were also used to produce supercapacitors when mixed with graphene oxide followed by freeze-drying.[102] The authors stated the synthesis of a nanostructured silk-based aerogel, however, literature states the term aerogel should only be reserved for supercritical drying of gels.[37] Forming hydrogels by freeze-drying produces forms known as cryogels.[37] The form is different because during freezing of a silk hydrogel, ice crystals form and damage the solid network which is prevented during supercritical drying. Additionally, in protein materials, freezing causes denaturing of the molecules and forms ribbon-like structures, which may be nanometer in one dimension but have micron dimensions in the other two.[103]

Silk aerogels are a new material form that needs thorough examination because it combines the material properties associated with silk fibroin and the physical properties of aerogels. The low bulk density, high porosity, and high surface area are physical

nanostructures that are difficult to attain in bulk 3D samples and have only recently been shown by supercritical CO_2 drying of silk gels. Additionally, even though supercritical CO_2 drying is designed to prevent structural damage to the skeletal matrix, the pressure required to reach supercritical conditions may have the potential to alter the physical structure and crystal structure producing new silk forms. These forms will provide a new set of potential applications to an already expanding material toolbox.

Discussion regarding aerogels

Aerogels are unique solids because of their physical properties such as low bulk density, high porosity, and large inner surface area.[7,75] Silica is the most common material used to make aerogels, however, silica is an inert, brittle material that can lead to problems when trying to interface with biology.[7] Naturally derived macromolecules are more advantageous in biology due to their chemical structure and biodegradability and have only recently appeared as aerogels.[42,43] However, several natural materials perform differently under supercritical drying conditions. Additionally, it is also difficult to form nanostructured materials in bulk solids. Therefore, it is necessary to attempt to synthesize nanostructures in biologically relevant materials to improve biomedical applications.

Silk as a biomaterial

Over the past decade, silk fibroin, the natural protein from the *Bombyx mori* caterpillar, has emerged as a promising biopolymer to stabilize biological material activity (such as enzyme,[104] vaccines, and drugs[105]) and as a material to make novel biomedical devices due to its biocompatibility,[106] ease of functionalization,[107] robust

mechanical properties,[108] and biodegradability.[109] It has been processed into several forms including fibers, films, sponges, and gels under benign conditions in an all water-based process.[45,107,110,111] The advent of silk as a biomaterial has inspired the development of a new class of bioactive sensors and imparted functionality on protein-based optical devices.[45,112] Silk has been used for sensing platforms, including photonic crystals[113] and microlens arrays fabricated by casting an aqueous silk solution on patterned molds. Furthermore, by changing the processing conditions, new forms made from silk fibroin can be achieved as bioactive sensors and tissue engineering applications.

Fibrous proteins are the structural building blocks of many biological networks and exist in many different forms. Silk fibroin is one of the strongest natural materials and has shown great potential as a future degradable material.[106] It consists of a heavy chain (~390 kDa) and a light chain (~26 kDa) linked together in a disulfide bond[106] where the primary sequence is composed of glycine (43%), alanine (30%), and serine (12%). Silk fibroin is composed of several repetitive amino acid sequences forming beta-sheet structures due to hydrophobic domains in the primary amino acid sequence.[106,114,115] The resulting hydrogen bonds create parallel and anti-parallel chains providing the strength observed in bulk silk materials.[116]
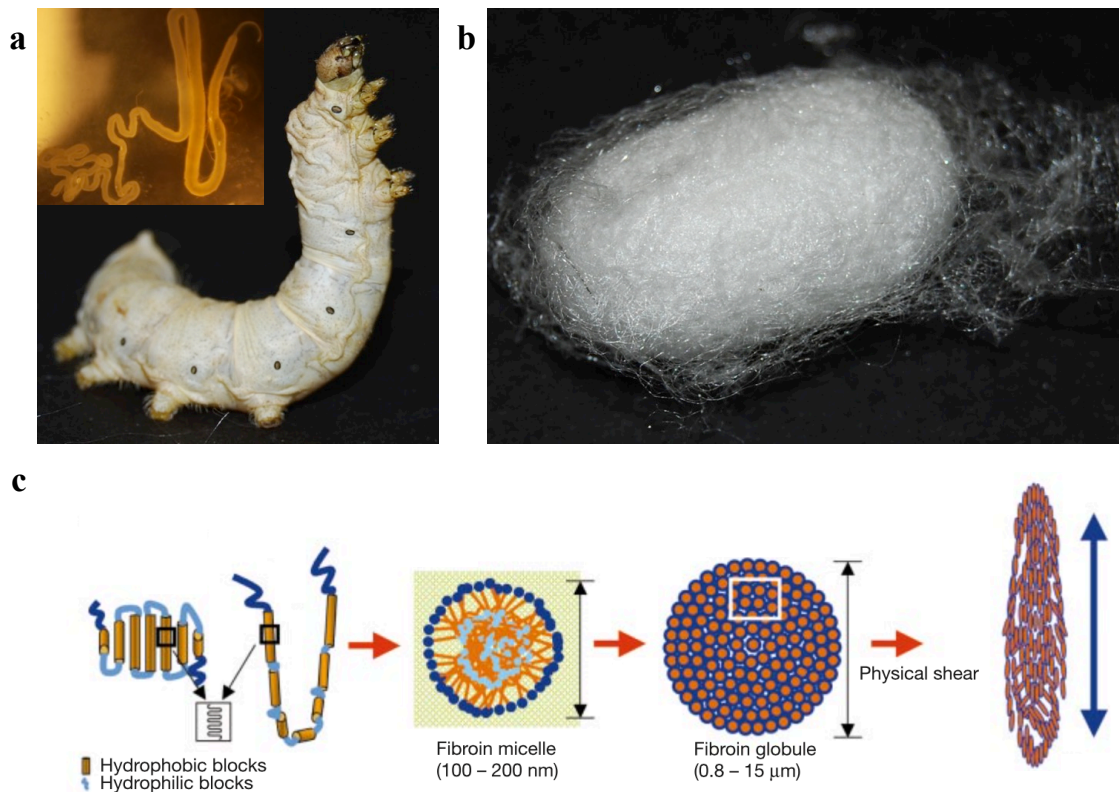
Figure 5. The different scales of silk fibroin. a) Silk worm caterpillar. Inset graph is silk gland. b) Silk cocoon. c) The molecular structure of silk fibroin in water solution (borrowed from [103]).

Before the formation of hydrogen bonds the amphiphilic nature of silk fibroin in water leads to the collapse of molecules into unimer micelles via intramolecular hydrophobic interaction.[115,117] Water is a unique fluid as it stabilizes self-folding hydrophobic conformations, and the replacement of water molecules around proteins can result in destabilization of native protein folds and changes to the micelle structure. When the water content is low, such as during the addition of other solvents or during drying, the surrounding environment induces stresses on the protein molecule resulting in different responses and property changes.[118] Replacing water with an organic solvent creates a competition with the protein for water uptake inducing partial dehydration and

partitioning of water that remains absorbed on the hydrophilic protein side groups.[118] This induces transformations that result in nanostructures producing different material forms as the normal liquid solution converts into a more solid state.

Developing nanostructure in silk fibroin has been limited after extraction from the *B. mori* silk gland. The nanostructure that promotes silk fibroin strength and flexibility is destroyed in the reconstituted form and there have been few processes to control nanostructures in bulk silk fibroin substances such as rapidly changing temperature, applying shear stress, changing pH, or altering osmolarity in order to recreate the nanostructure.[108] The formation of nanostructured materials using reconstituted silk fibroin solution is incomplete and is limited by processes such as direct molding of surface features, e-beam writing, electrospinning, or casting around a sacrificial mold.[45,113,119,120] By controlling the silk molecular weight during gelation, the solvent surrounding the molecule, and the concentration of the silk, it is possible to produce different silk forms limited in dimension to reestablish similar native properties not observed using previous methods.

Problem statement

In this dissertation, we investigate silk fibroin nanostructured materials by exchanging the fluid environment around silk molecules to generate different forms for biomedical applications. Specifically, this work will establish an empirical model of silk nanoparticle formation using a microfluidic device and establish two gel networks and examine their physical and chemical structures. We *hypothesize* that microfluidic devices have the ability to produce micron and submicron particles, and mixing reconstituted silk

fibroin solution with organic solvents will produce a colloidal suspension followed by gelation as a result of water removal inducing particle growth and aggregation, while supercritical drying of silk hydrogels will form nanofiber networks to be used for sensing and open pore structure applications.

Conclusions

Developing new methods to synthesize and control nanostructures using silk fibroin are capable of producing new forms for biomedical applications. By controlling processing conditions, it is also possible to identify structural alteration assisted by changes to secondary structures to examine how the material transforms.

Specifically, this dissertation provides an empirical model of nanosphere formation in reconstituted silk fibroin using nanoprecipitation and a microfluidic device. Additionally, it characterizes the formation of nanostructured hydrogels from silk fibroin micelles to particles after the addition of organic solvents. In particular it investigates cellular response to the nanostructured hydrogel in an *in vitro* cell culture model. Lastly, this dissertation provides a model regarding silk nanofiber formation during supercritical drying and characterizes its physical properties at near-critical and supercritical pressures while providing specific liquid and gas sensing applications which rely on the physical characteristics associated with aerogels and the stabilizing ability of silk fibroin.

There is a significant need in the academic and industrial fields to find a new generation of naturally derived biomaterial forms to interface with biology, physics, and engineering regarding nanotechnology applications. While today there are materials that provide biocompatibility and degradability, the future of biomaterials is to develop forms

that actively interact with their environment at the smallest possible dimension. Developing structures in silk fibroin will offer new areas of research regarding biomedical applications due to the unique combination of material properties and physical properties as an excellent candidate for augmented functionality demonstrating the utility and versatility of nanotechnology in biomaterials.

Abstract

Microfluidic flow focusing is a promising route for the synthesis of controlled emulsions and particles. Flow focusing is necessary to control consistent droplet formation to produce monodisperse particles. Controlling particle size distribution at the micron- and submicron scale is reproducible and improves the release kinetics for drug delivery applications. Silk fibroin, from the *Bombyx mori* caterpillar, is a well-know biopolymer maintained as a regenerated solution and is capable to be used with microfluidic devices. Here we evaluate flowing a silk solution through microfluidic channels and show the synthesis of consistent micron and submicron spheres with sphere diameter as small as 200 nm with low dispersion. Additionally, this synthesis method allows for the addition of drug molecules for controlled release of pharmaceuticals.

Introduction

Microfluidic devices have gained popularity in recent years due to their ease of fabrication and handling of small volumes of liquids, making them useful for high-throughput applications.[121–126] Microfluidic systems have a small footprint and are easily scalable providing cost effective, small, reproducible devices. Microfluidic devices have been the subject of significant research to produce consistent droplets (and spheres) exploiting fluid hydrodynamics.[34,122–130] In particular, capillary devices successfully generate controlled emulsions because of the dependence of the droplet size on the flow rates of immiscible fluids used in the synthesis of monodispersed particles[125,126] on the micron- and submicron scales that can be used for drug delivery,[130,131] sensing applications (e.g. magnetic particles[131]), contrast agents in MRI,[132] and core/shell nanosphere technologies.[133]

The ability to control particle size distribution on the micron scale is important in these contexts, to improve reproducibility of release kinetics for drug delivery applications where monodisperse particles have more uniform release kinetics than polydisperse particles.[129] Particle diameter as controls the plasmonic resonance of core/shell nanospheres and their tunable, size-dependent, optical properties.[133] The use of protein-based materials provides additional utility for these systems, since they can be absorbed by the body with safe degradation.[130]

Silk fibroin, the natural protein extracted from the caterpillar *Bombxy mori*, is an appealing biopolymer due to its natural self-assembly, ease of conforming to nanoscale sizes, biocompatibility, and lack of toxicity and immunogenicity.[108,134] Silk has been shown to maintain the function of entrained biological dopants, allowing silk to act as a

carrier for the preservation and delivery of drugs.[108,134,135] Moreover it is possible to control the kinetics of silk degradation by managing the degree of crystallinity, thereby regulating the breakdown of the material which, for drug delivery applications, allows for controllable release kinetics of encapsulated drugs in contrast to bulk release.[135–139]

We present here a simple and effective approach for the synthesis of silk fibroin micro- and submicron spheres using a co-flow capillary device where a continuous phase (PVA) is flowed over a discrete phase (silk solution). The device allows the generation of uniform silk spheres without filtering, with simple purification steps, and with the possibility to generate consistently sized micron- and submicron spheres with tunable diameters. Sphere diameter was controlled by varying the concentration of PVA, silk concentration, the flow rate ratios, and silk molecular weight distribution.

Silk micron- and submicron spheres have been prepared using spray drying and freeze drying,[140–143] chemical modification by nucleation of eADF4(C16),[144,145] adding organic solvents such as ethanol or methanol in a drop wise fashion,[146–148] water/oil emulsions,[35,149–153] and blending with immiscible polymers such as poly(vinyl) alcohol (PVA).[154] To date, there has been little study using microfluidic technologies to synthesize uniform microspheres and submicron spheres. Polymers such as alginate, poly(lactic-co-glycolic acid) (PLGA), and poly(L-lactide) (PLA) have been used in microfluidic devices to generate microspheres.[129] A co-flow focusing device was used with silk fibroin and oleic acid to synthesize large microspheres with diameters between 145-200 μm.[35] Such particles may be difficult to purify because oleic acid leaves unwanted residues. Moreover, this synthesis requires an additional step to stabilize the

particles by physically crosslinking (beta-sheet formation) the silk fibroin with methanol, ethanol, or isopropanol.

Experimental

Materials

Silk processing

Production of silk fibroin solution was previously described.[108] The purification of silk fibroin from *Bombyx mori* cocoons initially involves the removal of sericin, by boiling the cocoons in 0.02 M aqueous solution of sodium carbonate for 30 or 60 minutes. The remaining fibroin bundle is washed in deionized water and dried overnight, and then dissolved in 9.3 M aqueous lithium bromide at 60°C for three hours. Dialysis of the solution against deionized water (dialysis cassettes Slide-a-Lyzer, Pierce, MWCO 3.5K) enables the production of 6% w/v silk fibroin solution.

Methods

Viscosity measurements

Viscometer measurements were measured using a Brookfield viscometer (Brookfield engineering laboratories, Middleboro, MA, USA). Silk concentrations of 10 mg/ml, 30 mg/ml, and 60 mg/ml solutions were measured for 30 minute and 60 minute boiled silk. An up-down rate ramp was conducted on 500 μl of individual solutions on shear rates from 37 to 750 Hz. Three measurements of shear stress were averaged at 5 second increments for individual shear rates. The plastic viscosity was calculated for each solution using the Bingham model for viscoplastic materials.

Microfluidic device and fabrication

The PDMS flow focusing device molds were fabricated on a silicon wafer using photolithography with 30 μm thick SU-8 resist which determined the channel height. The silicon wafer was used to pattern liquid polydimethylsiloxane (PDMS) and was cured creating a negative mold. The PDMS negative was oxidized in a plasma chamber and bonded to a glass surface. The hydrophobic nature of PDMS is lost through oxygen plasma treatment during the bonding process making the surface hydrophilic. Surface modification such as silanization of the PDMS makes the surface hydrophobic and changes the performance of the microfluidic device.

The co-flow capillary device was made from type 304 reusable stainless steel needles purchased from McMaster-Carr with luer lock fittings. Luer lock fittings were machined and screwed into machined holders creating the coaxial needle. Silicone tubing attached the needles to two individual syringe pumps from New Era Pump Systems Inc. The continuous phase was a 2 % to 5% (w/v) mixture of poly(vinyl alcohol) (PVA) in water (M_w 30,000-70,000, 99+% hydrolyzed from Aldrich) and the discrete phase was silk concentrations of 10, 30, and 60 mg/ml. The continuous phase flow rate was kept constant for all experiments (4 ml/hr) while the discrete phase varied from 0.4 ml/hr to 0.04 ml/hr. All solutions were filtered through a 5 μm filter before use.

The solution collected from the device was cast onto a polydimethylsiloxane (PDMS) surface and left to dry for 24 hours. To remove the PVA the dried films were dissolved in ultrapure water at room temperature. The solution was centrifuged at 11,000xg for 10 minutes at 4 °C. The supernatant was discarded and the pellet was resuspended in the

same volume of ultrapure water and centrifuged again. The final pellet was suspended and stored in 1 ml of ultrapure water at 4 °C.

Scanning Electron Microscope images

Images of each batch of microspheres were examined under a Zeiss EVO MA 10 (Carl Zeiss SMT, UK) Scanning Electron Microscope (SEM) at 3keV. Each sample was sputter coated with palladium/gold before imaging.

Dynamic light scattering (DLS)

DLS analysis of the silk nanoparticles was previously described.[154] DLS experiments were conducted using a Brookhaven Instrument BI200-SM goniometer (Holtsville, NY) equipped with a diode laser operated at a wavelength of 532 nm. Quantitative analysis of the distribution of relaxation times and corresponding size distributions were obtained using the non-negative least squares: Multiple Pass (NNLS) method.[155,156] To analyze sphere size the size distribution extrapolated by the DLS was fitted with a Gaussian function; the center of the Gaussian was used to estimate the average size and the sigma value to estimate the variance.

Fourier transform infrared spectroscopy (FTIR)

FTIR analysis of microsphere samples was performed in a JASCO FTIR 6200 spectrometer (JASCO, Tokyo, Japan) in transmission. A drop of the microsphere solution was let to dry on a silicon wafer. For each sample, 32 scans were coded with a resolution of 4 cm^{-1}, with a wavenumber range from 4000-400 cm^{-1}. Fourier self-deconvolution of

the infrared spectra covering the amide I region (1595-1705 cm^{-1}) was performed by Opus 5.0 software.

Albumin-fluorescein isothiocyanate conjugate release kinetics

The release kinetics of FITC-BSA from silk spheres was studied using three different diameter microspheres. Silk solution was loaded with 2% FITC-BSA per mass of silk. Three concentrations of silk solution using unloaded and loaded solutions (60 mg/ml, 30 mg/ml, and 15 mg/ml) were used with a flow rate of 0.4 ml/hr. Samples were purified using the same process as mentioned above and placed into 1.5 ml microvials containing 1 ml pH 7.4 phosphate buffered saline (PBS). All samples were gently agitated at 37°C for various time periods up to 7 days.

At 1 hr, 2 hrs, 3 hrs, 4 hrs, 9 hrs, 24 hrs, 48 hrs, 72 hrs, 96 hrs, 120 hrs, 144 hrs, and 168 hrs, the sphere suspensions were centrifuged and the supernatant was collected for analysis. The pellet was resuspended in fresh PBS. The samples were assayed using fluorescent measurements (ex = 497nm, em = 524 nm) and compared to a standard curve. After the last day, samples were redissolved in 9.3 M LiBr solution to extract the remaining FITC-BSA to measure the total amount of FITC-BSA present.

Results and discussion

Preliminary results were tested with a flow-focusing device made from polydimethylsiloxane (PDMS) because of its ease of fabricating micron-sized features to cast a mold using standard lithographic techniques. The PDMS mold had rectangular channels coming together in flow focusing design as shown in **Figure 6** consisting of a

PVA continuous flow and a silk fibroin discrete flow. Controlling the flow rates of the discrete and continuous flows provided methods to tune particle diameter and determine the effectiveness of PVA/silk through a microfluidic device.
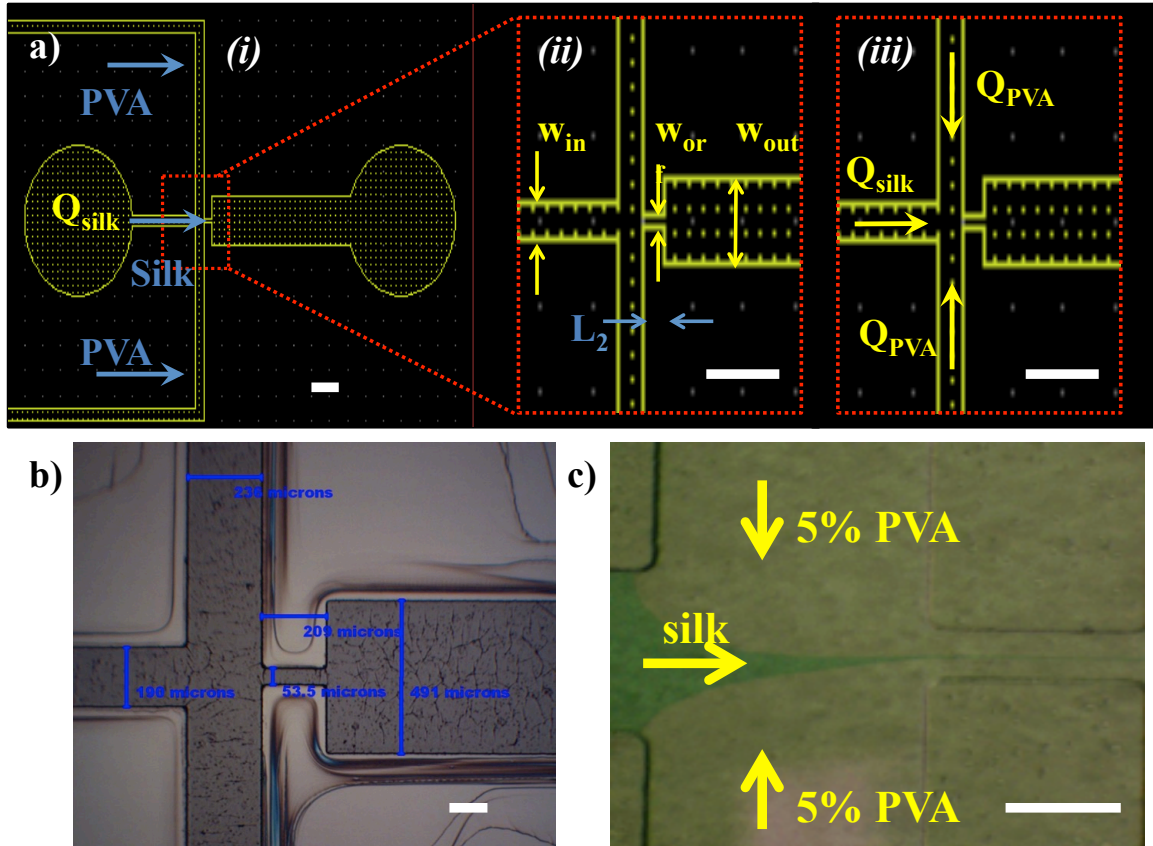
Figure 6. PDMS microfluidic design. a) Schematic image of microchannels used for the lithography master. b) Channels of SU8 molded on a silicon wafer used as the master to cast PDMS and prepare the microfluidic device. c) Silk flow-focusing device in action. Silk is dyed green and pumped through the channel producing silk droplets and spheres. Scale bar is 100 μm.

Monodisperse spheres were synthesized from the PDMS flow-focusing device and the diameter of the spheres varied depending on the flow rate ratio, silk concentration, and silk molecular weight. **Figure 7** shows SEM images of the spheres at the different

conditions and how their size depends on flow rate. The SEM images also show the morphology and dispersion of the particles after purification.
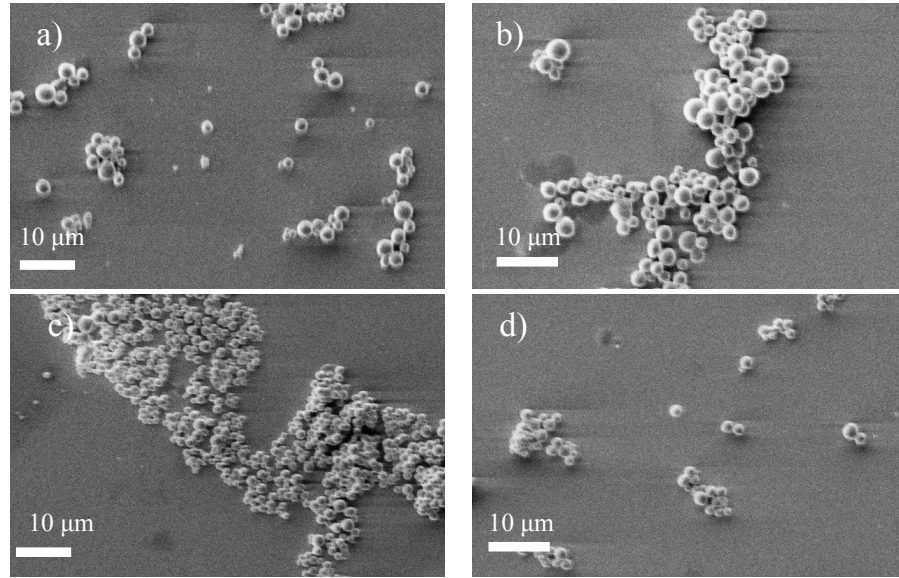
Figure 7. Scanning electron microscope (SEM) images of silk microspheres. Solution had a silk concentration of 10 mg/ml. The continuous flow rate of PVA was held constant at 1.3 ml/hr. The silk flow rate varied from (a) 275 ml/hr, (b) 225 ml/hr, (c) 175 ml/hr, and (d) 125 ml/hr.

Effect of surface wettability on sphere formation

However, even though spheres are generated, there were observable inconsistencies regarding sphere diameter and dispersity depending on when the PDMS device was used. To fabricate the microfluidic chip, the PDMS mold and glass slide are treated with oxygen plasma to bind the two (PDMS and glass) substrates together. Treating PDMS with oxygen plasma alters its wettability, but recovers after exposure to air for several hours (**Figure 8**). The contact angle of the PDMS in response to water, and silk solutions at different concentrations after exposure to air were measured and plotted. Additionally,

surface treatment with the silanizing agent tridecafluoro-1,1,2,2 tetrahydrooctyl

trichlorosilane (FOTS) to increase the contact angle after oxygen plasma. All surface

contact angles are plotted in **Figure 9**.
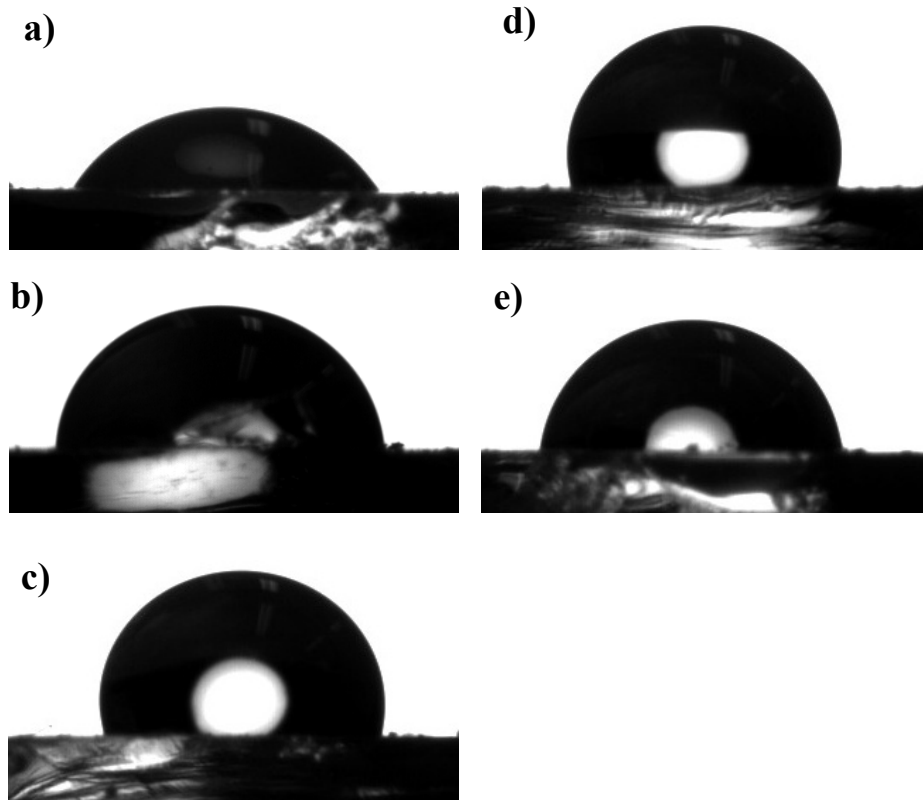
Figure 8. Images of different droplet contact angles on different treated PDMS surfaces. The contact angle increases as the PDMS becomes more hydrophobic. a) After O_2 plasma treatment. b) 8 hours after O_2 plasma. c) Days after O_2 plasma. d) Silanized PDMS. e) PDMS submerged in Poly-L-lysine.
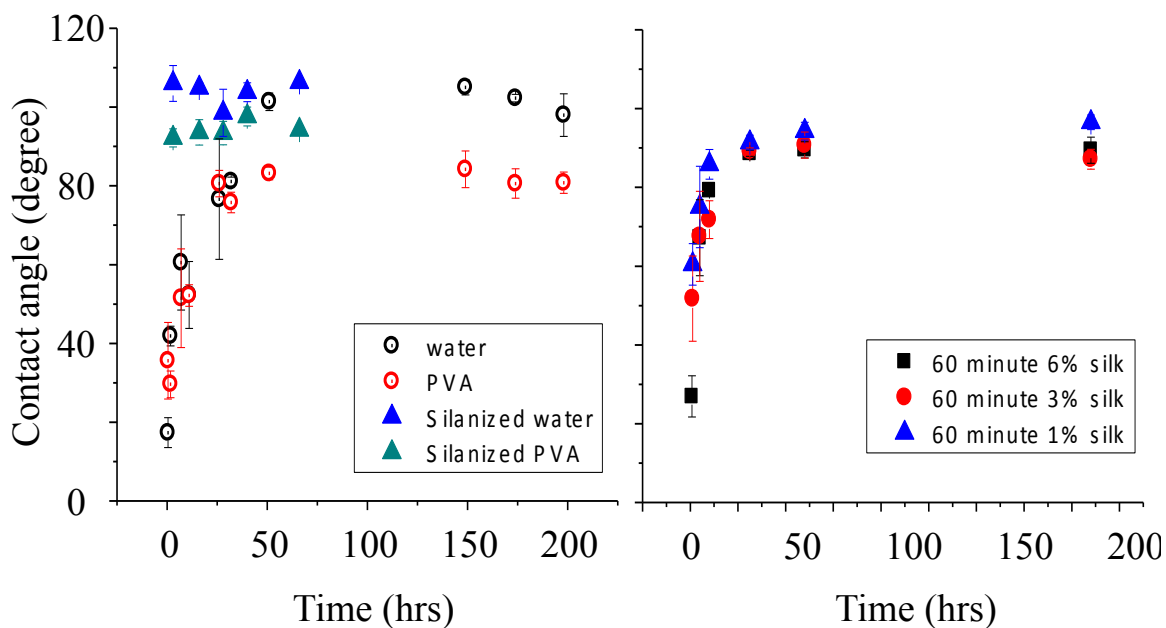
Figure 9. Graphs show the plotted contact angle of droplets on PDMS surfaces after plasma cleaning for different solutions at different times. Examination reveals how the PDMS returns to a hydrophobic state.

Since capillary forces associated with wettability of a material are significant regarding flow focusing, small changes to the surface contact angle alters the size and dispersion of the spheres. **Figure 10** shows sphere diameter as a function of concentration, flow rate ratio, and contact angle of the flow-focusing device as measured by DLS. Devices with more hydrophilic PDMS sidewalls produce smaller spheres compared to more hydrophobic devices. Nevertheless, the trend associated with changes in concentration and flow rate ratio remains the same.
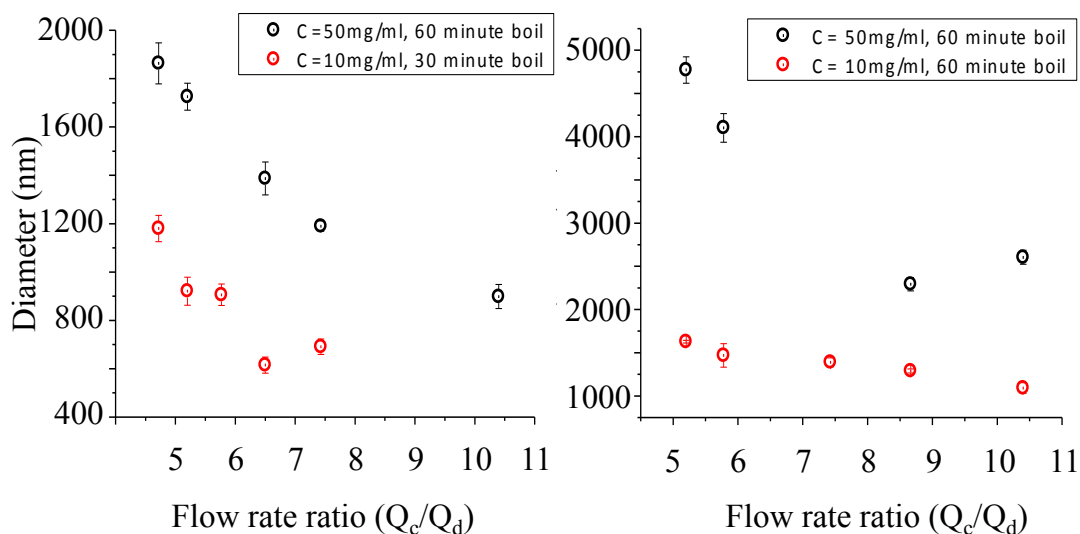
Figure 10. Plot of sphere diameter as a function of flow rate ratio for different silk concentrations. (Left) Diameter of sphere when PDMS is hydrophilic (10 hours after O_2 plasma) and (right) when PDMS is hydrophilic (days after O_2 plasma).

We examined the wettability of PDMS flow focusing devices to control the size and dispersion of silk fibroin particles using extremely small fluidic volumes. Due to silk's ability to act as a biologically favorable carrier that enables bio-dopants to maintain their functionalities, this device can be used to produce functionalized, controllable monodisperse nano- and micro-particles for biological applications. However, the inconsistencies found in this device are not desirable for scale-up operation of silk micron- and submicron sphere synthesis. Therefore, it is necessary to create a device with more consistent wettable surfaces to create monodisperse spheres. Additionally, creating a device where the silk solution is completely surrounded by the continuous phase should be required to produce more repeatable and consistent spheres for drug delivery applications with more controlled release.

Co-flow focusing device

In the work described here, a coaxial device composed of two dispensing needles to form a concentric needle system was designed (**Figure 11**). The outer channel consisted of a 16-gauge needle with an inner diameter of 1.2 mm, while the inner channel was a 30-gauge needle with an inner diameter of 152 μm. The resulting device is versatile, reusable, and cost-effective, relying on stainless steel needles that are easily interchangeable and available in many diameters. This improves ease of use with respect to conventional microfluidic devices given the ability to control flow rates in spite of the limitation imposed by the available fixed diameter range of stainless steel luer-lock needles. Additionally, stainless steel can be sterilized without damaging the integrity of the device therefore allowing this system to be used for biological and biomedical applications.
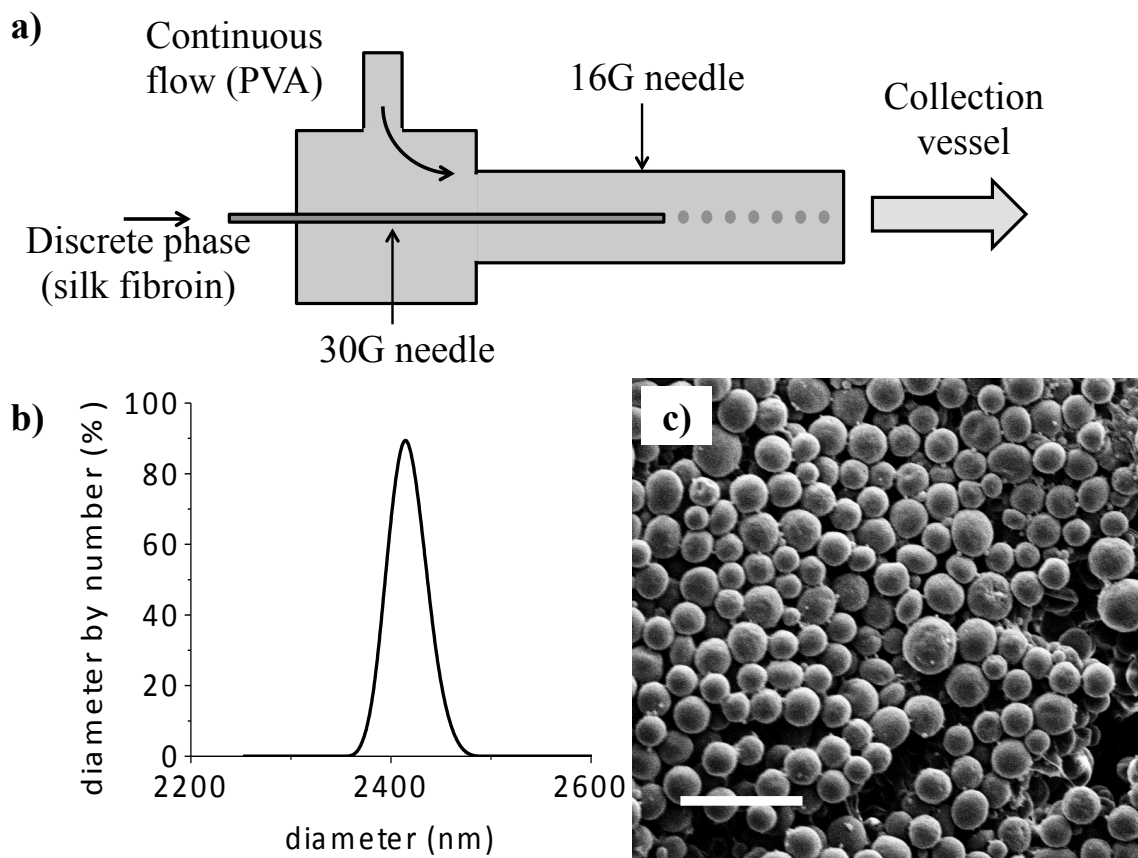
Figure 11. a) A schematic diagram of the fluidic device fabricated from stainless steel components. The dark spheres represent the silk droplets before drying in a PVA film. b) Sample distribution of particles found after purification from PVA film. The concentration of silk was 60 mg/ml with a continuous flow rate of 4 ml/hr and a discrete flow rate of 0.4 ml/hr. c) Typical SEM image of a collection of dried microspheres. Scale bar is 10 μm.

Sphere generation occurs by break-off of the discrete phase in the bulk fluid stream leading to the formation of monodisperse droplets.[128] Self-assembly of silk fibroin in the droplets produces consistently sized spheres in the micron or submicron range. The type of break-off of the droplet is determined by the volumetric flow rates of the continuous and discrete flows of the two immiscible fluids, the interfacial tension, and viscosity of the fluids. This in turn determines the size of the droplets that break-off from the initial stream. Two droplet forming regimes are known in co-flow devices, dripping and

50

jetting.[35,122,128] Dripping is based on the difference between viscous drag forces and the surface tension holding the drop to the bulk fluid stream, while jetting is caused by the Rayleigh-Plateau instability within the inner stream.[35,128] In this case, we hypothesize that silk submicron spheres are generated in the jetting regime. Devices operating in the jetting regime have been shown to generate smaller diameter particles compared to the dimensions of the outlet orifice, in agreement with what is observed here.[128] In the case described here, both fluids are aqueous solutions with a low interfacial tension that leads to a reduction in the driving force for liquid jets to break-off into droplets. The mechanism for droplet formation in co-flow devices has been already addressed.[123] In the particular case of a coaxial device operating in the narrowing jet regime the equation that predicts the droplet size as function of the fluid parameters is: $d_d = a \cdot \left(\frac{6Q_d d_j}{k^* U_c}\right)^{\frac{1}{3}} - b$; where d_d is the droplet diameter, a and b are parameters that depend on the geometry of the device, Q_d is the discrete phase flow rate, U_c is the continuous phase velocity, d_j is the jet diameters, that is a function of (Q_d/U_c), and k^* is a dimensionless wavenumber that is a function of the viscosity ratio between the two fluids $k^* = k^*(\eta_d/\eta_c)$, with η_d is the viscosity of the discrete phase and η_c is the viscosity of the continuous phase.[123] Once the droplet of the discrete phase is formed silk will condense because it's immiscible with PVA, following the same mechanism reported previously.[154] With respect to the previous work on the silk spheres formation in a PVA solution bath the possibility to condense the sphere from a droplet of defined and consistent size allows the possibility to produce silk micron- and submicron spheres with better control on the size distribution. Since the droplet diameter can be controlled by changing fluid parameters like flow rate and viscosity, spheres with controlled and tunable size can be synthesized.

In the case of silk solution an increase in either the molecular weight of the silk solution or in its concentration results in an increase to its viscosity. The viscosity affects the break-off condition (k^* term in the equation), and a larger discrete phase viscosity will generate smaller particles. Control of the silk fibroin molecular weight can be achieved during silk solution preparation by using different boil times when processing the native silk fibers. Different silk concentrations can be obtained by dilution of the reconstituted silk with water. For 30 minute-boil silk, the measured viscosities are 1.12 cP, 2.53 cP, and 7.01 cP for 10 mg/ml, 30 mg/ml, and 60 mg/ml samples respectively, whereas for 60 minute-boil silk, the viscosities are 1.25 cP, 1.98 cP, and 4.18 cP for 10 mg/ml, 30 mg/ml, and 60 mg/ml samples respectively as measured by a Brookfield viscometer. The viscosity was calculated using the Bingham model for viscoplastic materials defined as $\tau = \tau_0 + \eta D$ where τ is the shear stress, τ_0 is the yield stress, D is the shear rate, and η is the viscosity. Solving for the slope of the graph plotted with shear stress vs. shear rate provides the measured viscosity (**Figure 12**). Ultimately, the combined control of fluid viscosity and flow rates enables generation of monodisperse silk spheres with tunable diameters.
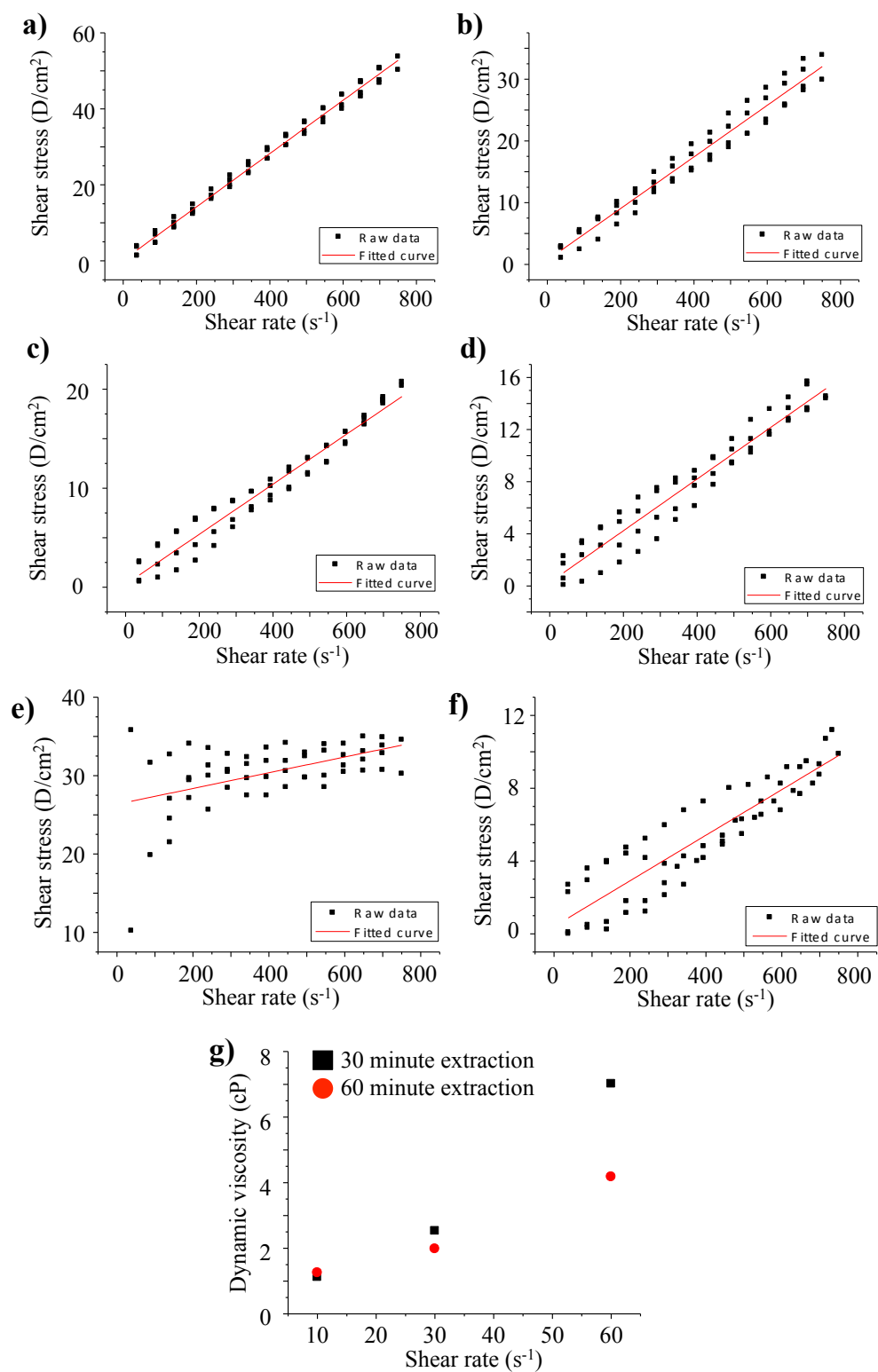
Figure 12. Viscosity measurements using a Brookfield viscometer. Shear stress vs. shear rate plots for 30 and 60 minute boil times for 60 mg/ml solutions (a-b), 30 mg/ml

solutions (c-d), and 10 mg/ml solutions (e-f). g) Calculated plastic viscosities for 30 minute and 60 minute boiled silk at different concentrations.

Figure 11b-c shows a histogram and a scanning-electron microscope (SEM) image of a typical unfiltered sample of silk nanospheres. The sample was obtained using a continuous phase of 5% PVA at 4 ml/hr flow rate and a discrete phase of 60 mg/ml silk boiled for 60 minutes at 0.4 ml/hr flow rate. The SEM image showed monodisperse, spherical particles with a smooth surface morphology. The distribution was centered at 2410 ± 20 nm as measured by DLS.

The diameter observed with SEM images agrees with DLS measurement implying that there is no shrinkage of the spheres upon drying as shown by other synthesis methods.[35] This supports that the spheres are made of densely assembled silk fibroin molecules. Maintaining the sphere diameter is relevant for applications such as controlled release kinetics of encapsulated drugs where the size distribution is the contributing release mechanism.

In order to assess the interplay between continuous phase flow and discrete phase flow on the resulting particle diameter, both the concentration of PVA and of silk were independently varied. The viscosity of both PVA and the silk solutions alters the size of the droplet.[157] At first, concentrations of PVA ranging between 2-5% were used to evaluate size variation while maintaining constant both the flow rates (continuous flow rate: $Q_c = 4$ ml/hr and discrete flow rate: $Q_d = 0.4$ ml/hr) and silk concentration (60 mg/ml). **Figure 13** shows SEM images of the resulting silk spheres as a function of the different PVA concentrations used. The results show that at lower PVA concentrations, smaller spheres were synthesized. Particles with sizes from 850 ± 10 nm to 2410 ± 20 nm

were generated as shown in **Figure 13d**. The plot shows that microsphere diameter decreased monotonically with a decrease in PVA concentration. The decrease in sphere diameter can be attributed to the viscosity ratio term $k^{*}(\eta_d/\eta_c)$ in the droplet size equation.[123]
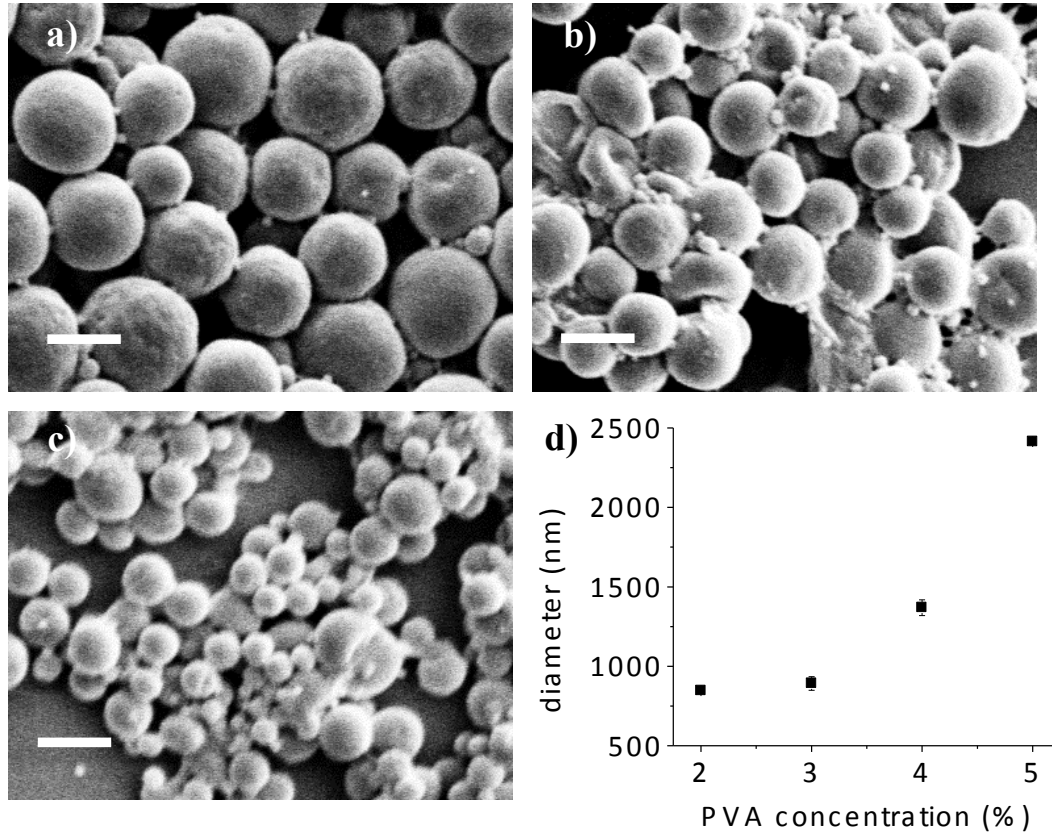
Figure 13. SEM images of varying PVA concentrations for a) 5%, b) 4%, and c) 2% PVA concentration. d) Average sphere diameter measured by DLS as a function of PVA concentration. Scale bars are 2 μm.

Previous work in similar systems shows that decreasing the concentration of the polymer solution will result in the formation of smaller spheres.[34,127] Here silk solutions of different concentrations were evaluated while keeping continuous and discrete phase flows constant. Silk solutions of 10 mg/ml, 30 mg/ml and 60 mg/ml were fed at a

constant flow rate of 0.4 ml/hr into a continuous phase of 5% PVA solution flowing at Q_c=4 ml/hr. **Figure 14** shows the resulting spheres indicating a correlation between diameter decrease and decrease in silk concentration. DLS measurements performed on these samples gave sphere diameters of 850 ± 20 nm, 1400 ± 40 nm, and 2410 ± 20 nm for silk concentrations of 10 mg/ml, 30 mg/ml, and 60 mg/ml, respectively as shown in **Figure 14d**. The change in sphere diameter was not solely attributable to the reduction in silk mass per droplet. Decreasing the concentration of silk will decrease the solution viscosity and the total mass of silk in the discrete phase. In this case two antagonist effects are expected: from the droplet equation a decrease in viscosity of the discrete phase should result in an increased droplet size; from the decreasing in concentration a decrease in mass per droplet and so a decrease in spheres' size is expected. From a simple mass balance a radius factors assuming only a decrease in concentration for droplet of the same size can be calculated: $\frac{r_1}{r_2} = \sqrt[3]{\frac{m_1}{m_2}}$, where r_1 and r_2 represent the two silk sphere radii and m_1 and m_2 represent the mass of silk in the different droplets associated with different concentrations. For spheres with different concentration radius values of 0.794, 0.693, and 0.550 for spheres with a mass ratio of 1/2, 1/3, and 1/6 respectively (associated with 60 mg/ml and 30 mg/ml samples, 30 mg/ml and 10 mg/ml samples, and 60 mg/ml and 10 mg/ml samples). However, measured values from the observations did not match the theoretical factors: when decreasing concentration silk spheres showed size smaller than expected from the pure mass balance, while an increase of the droplet size has to be expected. This different behavior can be explained not solely in term of variation of the microfluidic parameters. As a confirmation the yield of particles when changing concentration of silk was measured and the results are presented in the inset of

Figure 14d. The measured yield was found to be 42 ± 5 % when using 60 mg/ml, 31 ± 3

% when using 30 mg/ml and 5 ± 2 % when using 10 mg/ml. It can be hypothesized that

when diminishing the concentration of silk in the discrete phase the nucleation and

growth of new silk spheres becomes less efficient which can justify our observation of

smaller spheres than expected.
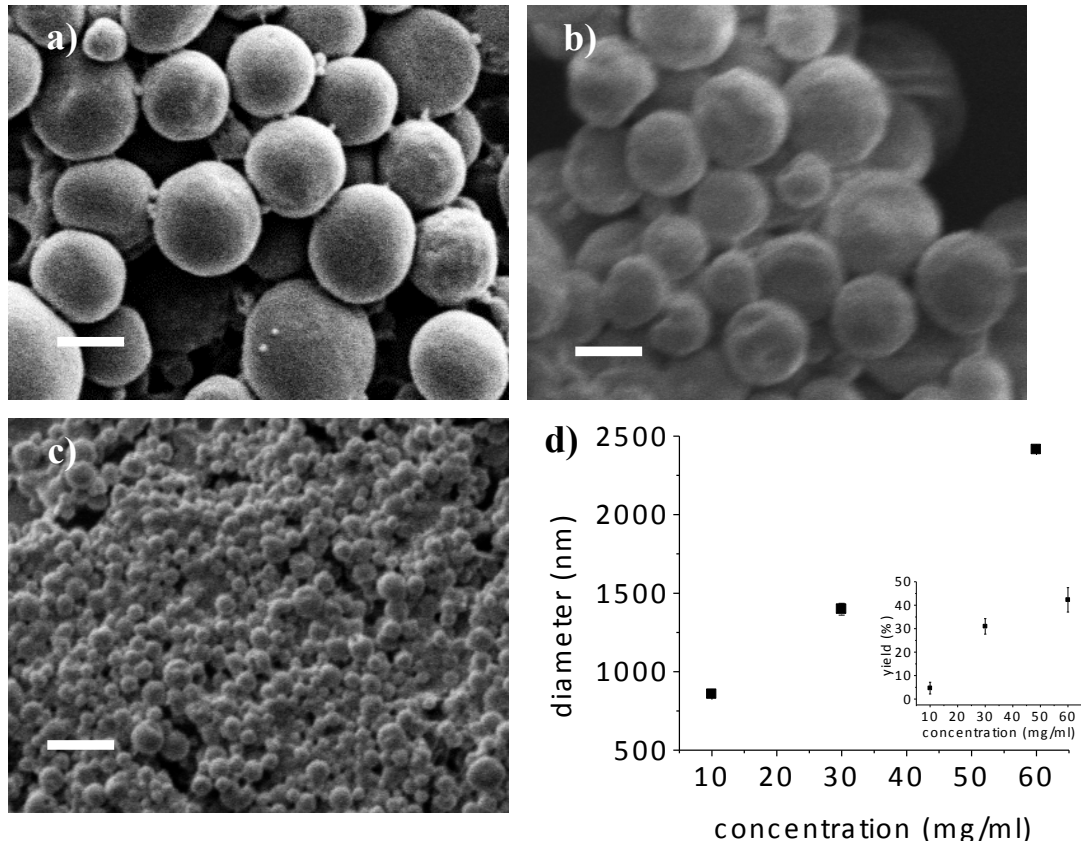
Figure 14. SEM images of silk spheres synthesized by changing silk concentrations: a) 60 mg/ml, b) 30 mg/ml, and c) 10 mg/ml concentrations. Scale bars are 2 μm. The continuous phase was 5% PVA and the flow rate ratio was 10. d) Average sphere diameter measured by DLS as a function of silk concentration. Bar represents variance. Bars represent variance.

The interplay between continuous and discrete phases can also be modulated through

the adjustment of the flow rate ratio Q_c/Q_d. For co-flow capillary devices smaller droplet

sizes are obtained as the flow rate ratio increases.[35,122–124,128] Keeping silk and PVA concentrations fixed, the silk flow rate was varied from 0.04 ml/hr to 0.4 ml/hr while Q_c was held constant at 4 ml/hr. Flow rate ratios Q_c/Q_d from 100 to 10 were evaluated yielding particles with sizes ranging from 1170 ± 20 nm to 2410 ± 20 nm (for a silk solution concentration of 60 mg/ml with 60 minute boil time) as illustrated in **Figure 15a**. As expected, microsphere diameter decreased with a decrease in the discrete phase flow rate. By reducing the concentration of silk fibroin to 10 mg/ml and 30 mg/ml, it was possible to generate submicron spheres with diameters ranging from 210 ± 20 nm to 860 ± 20, and 640 ± 20nm to 1400 ± 40nm, respectively for the same flow rate ratios above, as shown in **Figure 15b**.

Increasing the molecular weight of the silk fibroin chains can be achieved by reducing the boiling time of the protein.[108,134,139,158] To determine the effect of molecular weight on sphere synthesis, three boiling times (10, 30 and 60 minutes) were examined, which correspond to an average molecular weight distribution of 400 kDa, 150 kDa, and 50 kDa respectively.[158] As shown in **Figure 15** thirty minute boiled silk with a concentration of 60 mg/ml produced spheres with diameters ranging from 600 ± 40 nm to 2120 ± 20 nm at 100 and 10 flow rate ratios respectively. Sixty minute boiled silk with a concentration of 60 mg/ml produced spheres ranging from 1170 ± 20 nm to 2410 ± 20 nm with the same flow rate ratio. Ten min boiled silk solution was unsuccessful because it clogged the inner needle and produce spheres of inconsistent size. From the droplet model a decrease in the droplet diameter was expected as the viscosity of the discrete phase increases because the k^* term in the equation is a function of the viscosity ratio $k^*=k^*(\eta_d/\eta_c)$. While in the case of silk solution with a concentration of 10 mg/ml a similar

viscosity was measured (1.12 cP for 30 minute boiled, 1.25 cP for 60 minute boiled) and

particles of similar size were generated over the flow rate ratios used.
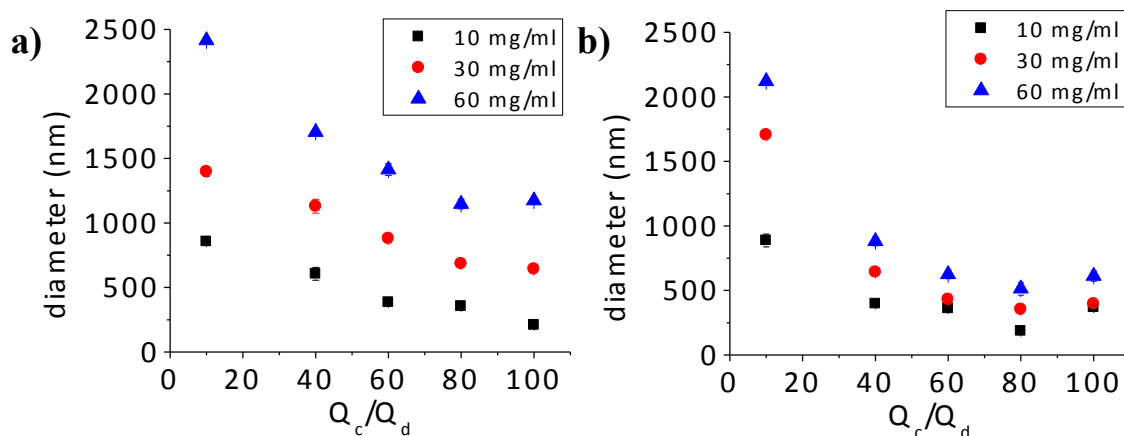
Figure 15. a) Average diameter of particles for 10 mg/ml, 30 mg/ml, and 60 mg/ml solutions of 60 minute boil silk. The continuous phase (Q_c) was held constant at 4 ml/hr and the discrete phase (Q_d) was varied giving different flow rate ratios. b) Average diameter of particles for 10 mg/ml, 30 mg/ml, and 60 mg/ml solutions of 30 minute boil silk. The continuous phase (Q_c) was held constant at 4 ml/hr and the discrete phase (Q_d) was varied giving different flow rate ratios.

Silk microparticles have been used in the past for drug release applications. In the

previous literature, especially in the case of silk films, the control on the degradation

kinetics was achieved by controlling the crystallinity of silk. Silk fibroin crystallization

leads to the formation of beta-sheet structures that have absorption features in the 1616

cm^{-1} – 1637 cm^{-1} region.[159] To characterize the structure of silk fibroin in the

microspheres the Amide I absorption band in the 1605 cm^{-1} - 1705 cm^{-1} region was

analyzed. In the case of silk spheres the absorption spectrum (**Figure 16**) was overlapped

with the scattering of the infrared light which resulted in a shift of about 15 cm^{-1} to lower

wavenumber of the features. This shift was determined using the so called side chain

band (1605 cm^{-1} – 1615 cm^{-1}) that was observed at 1595 cm^{-1} in our sample. Because of

the scattering a quantitative analysis of the Amide I band wasn't possible, but from a qualitative point of view silk microspheres showed an intense absorption peak in the 1606 cm^{-1} – 1629 cm^{-1} region which can be related to the presence of beta-sheet structure in the nanoparticles (reference value for the beta-sheet band are 1622 cm^{-1} – 1637 cm^{-1}).[159] However in the present work crystallization of silk fibroin was not being used as a mean to control particles' degradation kinetics. The monodispersity and the tunability of the spheres' diameter made possible to use the spheres' size to control the release kinetics.
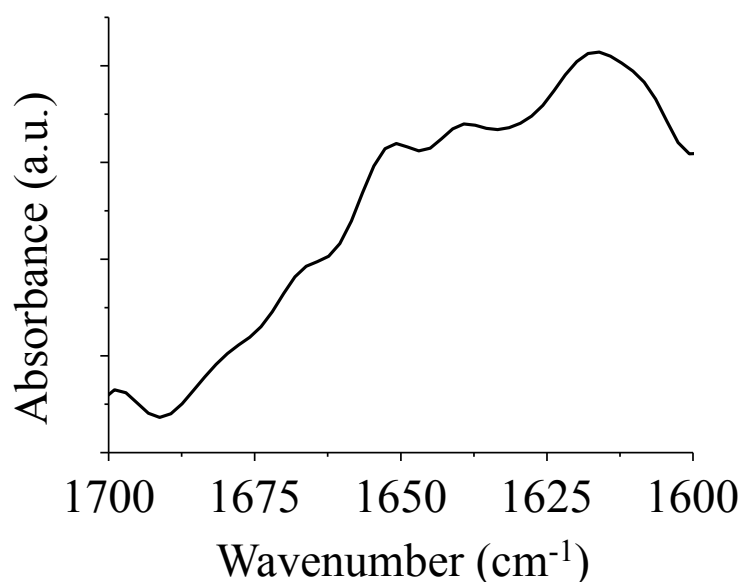
Figure 16. Self deconvolved FTIR spectrum of a collection of silk particles.

As a model drugs, albumin-fluorescein isothiocyanate conjugate (FITC-BSA) and fluorescein iscothiocyante conjugated dextran MW=70,000 kDa and MW=2,000-5,000 kDa were used. Each model drug was mixed with the silk solution prior to flowing through the co-flow device. Three different sphere sizes were examined (1000 nm, 1400

nm, 2410 nm) to characterize different release profiles. Loading efficiency was poor (5%) for dextran samples compared to loading with FITC-BSA (95%). These results were similar to ones reported in a previous study and in this case too it was determined by the molecular weight and the hydrophobicities of the loading molecules and their interaction with silk.[154]
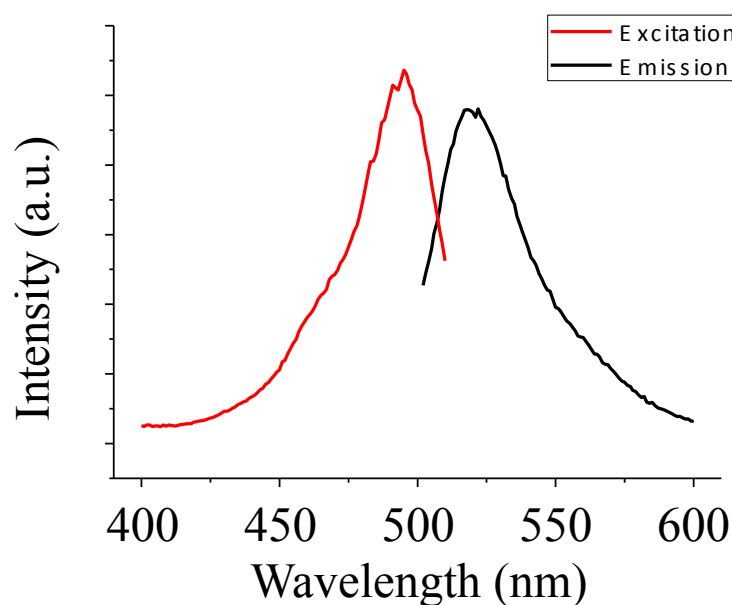
Figure 17. Excitation and emission spectra of FITC-BSA loaded silk microspheres.

We used the fluorescence at 524 nm of FITC-BSA to monitor the release of our model drug over time (**Figure 17**). The degradation study was performed in PBS at 37 ºC for one week, measuring the fluorescence of supernatant at the designated time points. In **Figure 18** the release profile of the nanoparticles is presented. Release percent is calculated by the accumulative release measured from the supernatant divided by the total amount of FITC-albumin loaded into the spheres. Following a burst release after the initial 24 hrs (40% of the total), the remaining drug was released more slowly. Spheres of

smaller diameter showed faster release: at the 7th day spheres with diameter of 1000 nm released 94% of total loading, while spheres with a diameter of 1400 nm and 2410 nm showed a release of 88% and 73% respectively. The difference in release is almost linear with the different surface to volume ratio of the spheres, as we can see on the inset of **Figure 18**.
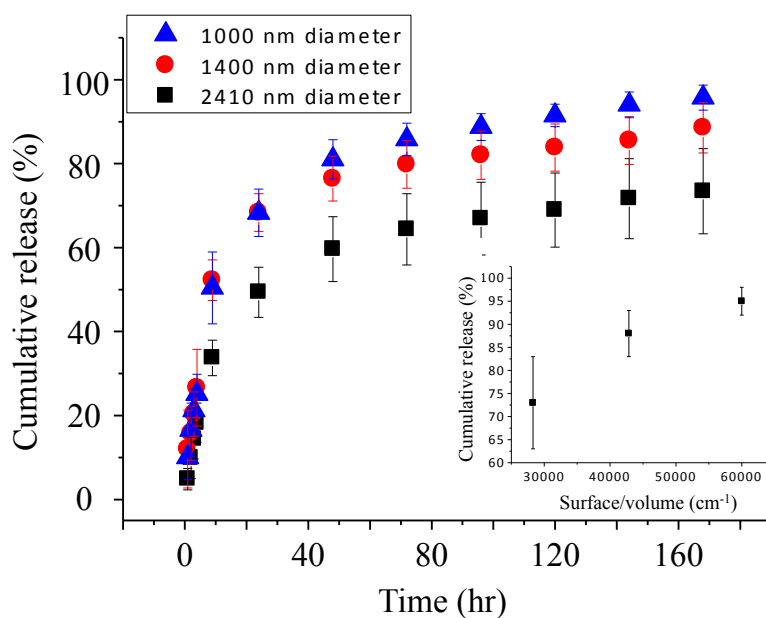
Figure 18. Cumulative release kinetics for silk spheres. Silk spheres showed a burst release of the drug over the first 24 hrs followed by a steady release. Smaller spheres (blue triangles) showed a faster release compared to larger spheres (black squares). Inset of the figure shows the correlation between the cumulative release at 168 hrs and the surface volume ratio.

Conclusion

In summary, a synthesis method for the formation of dense, monodisperse micron-submicron spheres of tunable size prepared from silk fibroin using a co-flow capillary

device was demonstrated. Control of the diameter was achieved using the flow rate ratio, the concentration of the silk protein, the concentration of PVA, and silk molecular weight. Using 60 mg/ml, 60 min boiled silk and a flow rate ratio of 10 it was possible to synthesize spheres greater than 2000 nm in diameter, while using 10 mg/ml, 60 min boiled silk and a flow rate ratio of 100 it was possible to synthesize spheres as small as 210 nm. Spheres were loaded with a model drug and the control on the release kinetics was obtained by changing the spheres' size. This approach can be used to generate tunable micron to submicron spheres for a variety of biological and chemical applications, including encapsulation of medicines for delivery of drugs and as contrast agents for non-invasive sensing.

Abstract

Silk fibroin is a well-known biopolymer that can be processed into many material formats, with potential applications in many areas ranging from optoelectronic to regenerative medicine. In the hydrogel form, silk fibroin has been proposed as substrates for the engineering, modeling and regeneration of soft tissues, ranging from nerves to cartilage. Current fabrication methods of silk fibroin produce microstructured materials that lack transparency, which has been of hindrance to fully capitalize on this material format. Light is in fact becoming an increasingly important mean of communication for instruction, sensing, diagnosis and visualization of biological entities, light sensitive molecules and in the use of optogenetic tools. Transparency is also the main characteristic of some human tissues (e.g. cornea) where silk fibroin in the film format has shown potential as scaffolding material. With the present chapter, we introduce a new method for the fabrication of transparent silk hydrogels that were shaped with convex or concave geometries to fabricate optical components. The mechanical properties of silk fibroin hydrogels were modulated within physiological ranges through an unprecedented metal chelation method, which also controlled the protein crystallinity. Silk fibroin hydrogels obtained through this method were indeed biocompatible and promoted attachment and infiltration of human dermal fibroblasts without any biochemical functionalization. In addition, seeding of human cornea epithelial cells (HCECs) on the hydrogel surface resulted in the formation of an epithelium, which did not alter the gels'

transparency and showed enhanced results when compared to HCECs-seeded collagen hydrogels.

Introduction

The reinvention of silk fibroin as a sustainable material for biomedical, optics, photonics and electronics applications has been predicated on the numerous material formats (*e.g.* fibers, foams, particles, films, hydrogels) in which the protein can be processed after regeneration in aqueous solution.[160] Additionally, silk fibroin materials can be engineered with tunable morphological, physical, mechanical and biological properties by fine regulation of molecular weight at the point of protein extraction from silk fibers during the removal of sericin and by controlling the degree of crystallinity through exposure to heat, water vapor or polar solvents.[111,160] For optics and photonics applications, the film format for silk has generated interest due to its transparency, robust mechanical properties, and preservation of heat-labile sensing molecules encapsulated within the protein, allowing for the fabrication of optic and photonic devices with unprecedented features that can be interfaced with biology.[107] Conversely, other commonly used material formats of silk fibroin, such as foams and hydrogels are characterized by high optical loss due to internal light scattering.[67,108,110]

Silk hydrogels have been proposed as substrates for the engineering, modeling and regeneration of soft tissues, ranging from nerves to cartilage.[69,70] There is in fact a need for soft biomaterials that match the physical and mechanical properties of human tissues by mimicking the hydrated nature of the extracellular space.[42,44,161] In addition, silk hydrogels can be easily modified to provide appropriate morphological, biochemical and mechanical cues and can be functionalized with stabilized heat-labile compounds.[103] Silk fibroin sol-gel transition occurs through inter- and intra-molecular interactions (mainly formation of hydrogen bonds and hydrophobic interactions) among protein chains, which

fold from amorphous to thermodynamically stable beta-sheets, driven by exposure of silk solutions to shear forces, electric fields, pH near or below the isoelectric point (pI=3.8-3.9), polar solvents, heat, and water removal.[67,110] The soft-micelle assembly process is also regulated by the strong amphiphilic (hydrophobic and hydrophilic domains) nature of the protein, where short hydrophilic (amorphous) spacers intervene between large hydrophobic (crystallizable) blocks and play a critical role in preventing premature beta-sheet formation and in modulating water solubility.[115] Development of inter-molecular bonds results in aggregation of silk fibroin micelles into interconnected micron-sized particles with progressive loss of transparency of the silk solution, ultimately becoming a white hydrogel due to light scattering. Despite numerous applications of silk fibroin hydrogels in biomedical engineering, the lack of transparency has been of hindrance to fully capitalize on this material format.[56] For example, biological entities (e.g. cells), light sensitive molecules (e.g. fluorescent, bioluminescent, photoactive macromolecules), and optogenetic tools can be incorporated into hydrogels for sensing and diagnostic applications, to generate biomimetic biological systems or to build optical interfaces with living tissues. Transparent hydrogels have been obtained with globular proteins by changing the molecular conformation to linear networks by heat denaturation but is an unsuccessful approach with silk fibroin.[110] Transparency is also the main characteristic of cornea tissue where silk fibroin has shown potential as scaffolding material for cornea replacements.[112,162–168] Indeed, the possibility of combining optical clarity in the visible spectrum with the well-established, tunable biophysical, biochemical and biological properties of silk fibroin hydrogels would shine a new light on this material format,

enabling the engineering of highly tunable tissue-equivalent constructs with enhanced optical and photonic functionalities.

In this study we report a new gelation method to induce the formation of a silk fibroin gel where the protein vesicles present in solution aggregate into nanosized particles during the sol-gel transition of the material, forming a transparent gel with defined shape and dimensions that are maintained upon removal from a mold. In addition, the method allows for the fabrication of hydrogels with convex or concave geometries that enable the formation of optical components such as a lens.

Experimental

<u>Materials</u>

Silk fibroin solution preparation

Silk fibroin solution was prepared as previously described by Rockwood et al. *Bombyx mori* caterpillar cocoons were boiled for 30 minutes in a solution of 0.02 M Na_2CO_3 to remove the sericin glycoprotein. The extracted fibroin was rinsed in deionized water and set to dry for 12 h. The dried fibroin was dissolved in 9.3 M LiBr solution at 60°C for 3 h. The solution was dialyzed against deionized water using a dialysis cassette (Slide-a-Lyzer, Pierce, MWCO 3.5KDa) at room temperature for 2 days until the solution reached a concentration of ~60 mg/ml. The obtained solution was purified to remove large aggregates using centrifugation and filtered through a syringe filter.

Hydrogel preparation

Acetone Optima (Fisher Scientific) was used to synthesize the hydrogels. Acetone was set in a glass Petri dish and silk solution with a concentration of 10 mg/ml was added to an acetone bath. The ratio of silk solution to acetone was of 2:1. The acetone was evaporated at room temperature while adding deionized water to exchange with the gels and to prevent gel collapse. To improve the mechanical properties of the hydrogels, the hydrogels were soaked in a 20 mM solution of ethylenediaminetetraacetic acid (EDTA) (pH=8.5 with Trizma base, Sigma Aldrich) for different time lengths from 1 h, 2 h, 7 h, 19 h, and 24 h. The hydrogels were rinsed in deionized water to remove any excess EDTA.

Type I collagen hydrogels (FirstLink UK, 2.1 mg/ml) were prepared as previously described and were used as a control for cell culture.

Measurements

Morphological characterization

SEM was used to evaluate scaffold morphology. All SEM micrographs were taken with a Supra55VP FESEM (Zeiss) using the in-lens SE detector. Morphological characterization of the hydrogels was obtained by drying the samples in hexamethyldisilazane (HMDS). Samples were first dehydrated in a series of ethanol rinses at concentrations of 50%, 70%, 80%, 90%, 95%, 100%, and 100% for 30 minutes and then exposed to a series of HMDS baths at 70%, 90%, 100%, and 100% for 30 minutes to ensure complete saturation in HMDS. Samples were then left to dry in a

chemical hood for 12 h to allow complete evaporation of HMDS and then immediately sputter coated and imaged at 3kV.

Physical characterization

For light transmission measurements, visible spectra were taken using a vis/near-infrared fiber-optic spectrometer (USB-2000, Ocean Optics). White light was propagated through the fiber to pass through the sample, and the transmitted light was coupled into a fiber tip guided to the spectrometer. The distance between the illumination source and the collection tip was fixed at 10 mm. All samples had a thickness of 4 mm.

Dynamic light scattering (DLS) experiments were conducted using a Brookhaven Instrument BI200-SM goniometer (Holtsville, NY, USA) equipped with a diode laser operated at a wavelength of 532 nm. DLS analysis of the silk nanoparticles were mixed in glass vials at concentrations of 10 mg/ml, 20 mg/ml, 40 mg/ml, and 60 mg/ml and analyzed before gelation. Quantitative analysis of the distribution of relaxation times and corresponding size distributions were obtained using the Non-Negative Least Squares: Multiple Pass (NNLS) method.[45] The size distribution extrapolated by the DLS was set to a weighted average to calculate the average diameter.

μRaman microscopy measurements

μRaman spectra were collected using a JASCO NRS 3100 laser Raman spectrophotometer (JASCO, Tokyo, Japan). Hydrogels were mounted on a glass microscope slide and excited at 784 nm with a laser focused using a 100x objective.

Spectra were obtained by measuring from 1800 cm^{-1} to 200 cm^{-1} using a resolution of 0.5 cm^{-1}, and 5 accumulations per sample with an exposure time of 20 s.

Mechanical characterization

Compressive properties of silk fibroin hydrogel were measured using an Instron 3366 testing frame (Instron, Norwood, MA) with crosshead rates of 0.100 mm/min, 0.200 mm/min, and 2.000 mm/min with a 10 N capacity load cell. Samples were conducted in air between displacement plates until maximum compression was reached (load limit set at 7 N). Compressive modulus was calculated using a least-squared fitting in the linear region of initial compression in the 5- 20% strain range or before the yield strength was reached.

Cell culture

Human dermal fibroblasts (HDFa, Invitrogen) were cultured on the silk hydrogels after treatment in ethanol for 24 h. Samples were rinsed in 3 subsequent PBS baths, pH=7.4 before cell seeding at a density of 20,000 cells/cm^2. Cultures were grown to confluence in Dulbecco's Modified Eagle Medium (DMEM), high glucose, GlutaMAX™ Supplement (Invitrogen), 10% fetal bovine serum (FBS), and 1% penicillin/streptomycin antibiotic (Invitrogen) maintained at 37°C in humidified atmosphere of 5% CO_2.

Human corneal epithelial cells (HCEC), isolated from the progenitor-rich limbal region of the eye, were purchased from Invitrogen. HCECs were cultured in Keratinocyte Serum Free Medium (Invitrogen) supplemented with 1% penicillin/streptomycin

antibiotic at 37°C in humidified atmosphere of 5% CO_2. HCECs at passage 3 were detached from tissue culture plastic using TrypLE™ Express (Invitrogen) and then reseeded on silk hydrogels and collagen hydrogels at a density of 25,000 cells/cm^2. Cultures were incubated at 37 °C for 3 h allowing the cells to attach to the hydrogel surface before the addition of media.

Metabolic activity

AlamarBlue^{TM} reagent was used to assess HCECs metabolic activity on silk fibroin hydrogel surfaces at days 1, 3, 7, and 10 in culture. Type I collagen hydrogels were used as a control. For metabolic activity, samples were incubated in complete culture medium with 10% AlamarBlue^{TM} reagent (Invitrogen, USA) at 37°C for 4 h. Post incubation, 100 ml aliquots of media were collected in triplicate from quadruple samples and the fluorescence detection, indicative of cellular reduction of resazurin indicator, was measured at 590 nm using 530 excitation using a microplate reader (SpectraMax M2, Molecular Devices, Sunnyvale, CA, USA). Acellular scaffolds were used as the background reference.

Cell imaging

Confocal images were taken with a Leica DMIRE2 confocal laser-scanning microscope (Wetzlar, Germany). Live/dead sample staining was conducted using a LIVE/DEAD$^®$ Cell Viability/Cytotoxicity Kit (Life Technologies, Grand Island, NY, USA) by incubating a solution containing 2 mM calcein AM and 4 mM Ethidium homodimer-1 (EthD-1) for 60 minutes at 37 °C. Samples were excited at 488 nm and

emission at 510-530 nm for live cells (green) and excitation at 543 nm and emission for dead cells at 610-640 nm (red).

For SEM analysis, cellular hydrogels were removed from each culture well and fixed in 10% buffered formalin and let to sit for 12 h at 4 °C. Samples were then removed and washed with 3 subsequent PBS (pH 7.4) rinses before dehydration in a series of ethanol solutions at 50%, 70%, 80%, 90%, 95%, 100%, and 100% for 30 minutes. Samples were then critically point dried using an Auto Samdri 815 Series A (Tousimis, Rockville, MD) operating above the critical point of liquid carbon dioxide. All samples were sputter coated using platinum/palladium and imaged at 3 kV.

Statistical analysis

All data were statistically compared with one way ANOVA tests using *one way Anova tool* (significance level = 0.05) using Origin Pro v. 8 Software (OriginLab, USA).
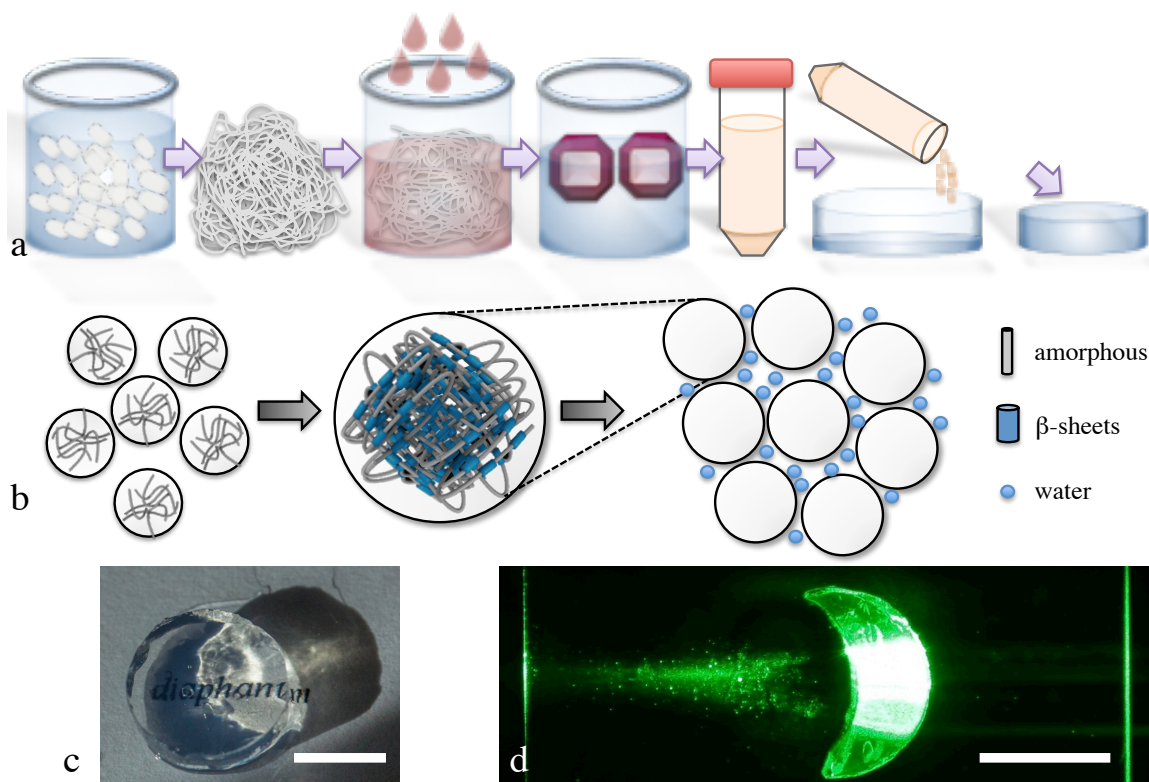
Figure 19. Fabrication of a silk fibroin hydrogel. a) Schematic representation of the processing steps required to fabricate transparent gels, starting from raw material (silk cocoon). The process starts with silk fibroin purification, which requires boiling silk cocoons in 0.02 M Na_2CO_3, to remove the outer layers of sericin. During cooling, cocoons are unraveled into fibroin fibers. Highly concentrated solution of chaotropic ions (i.e. LiBr) are then used to solubilize silk fibroin fibers. A dialysis step is then used to remove the chaotropic salts from the solution, yielding a pure fibroin solution. Free standing silk fibroin hydrogel are then formed by mixing silk fibroin solution with a ketone (e.g. acetone). b) Schematic representation of conformational changes within silk fibroin during sol-gel transition. Silk fibroin in solution possesses an amorphous structure (mostly random coils) and is arranged in micelles. When the silk fibroin solution is exposed to polar solvents, a combination of amorphous-to-crystalline conformational changes together with aggregation results in the formation of silk particles, which arrange together in the presence of water forming a free standing hydrogel structure. c) An image of a silk fibroin hydrogel produced through gelation methodology, which enabled the fabrication of an optically clear material. d) Fabrication of a concave silk fibroin hydrogel through gelation and its application as a lens. Scale bars are 5 mm.

Results and discussion

Physical characterization of hydrogels

By leveraging the sol-gel transition, a fast and robust method was developed to form nanoparticle-based silk hydrogels by mixing two parts of silk fibroin solution (average molecular weight of 100kDa, 10 mg/ml) with one part of acetone, where the choice of organic solvent, silk fibroin solution parameters, and the relative concentration of silk fibroin to organic solvent were selected to maximize gel integrity and transparency (**Figures 19-24**). Acetone was successfully removed during processing, and gelation in acetone provided enhanced transparency when compared to other silk gelation methods (**Figure 24**). In addition, silk fibroin concentration dictated the dimension of the silk particles within the forming hydrogel, and only silk solutions $\leq$ 15 mg/ml allowed to control silk fibroin particle diameter under 200 nm, resulting in optically clear hydrogels (**Figure 20-23**).
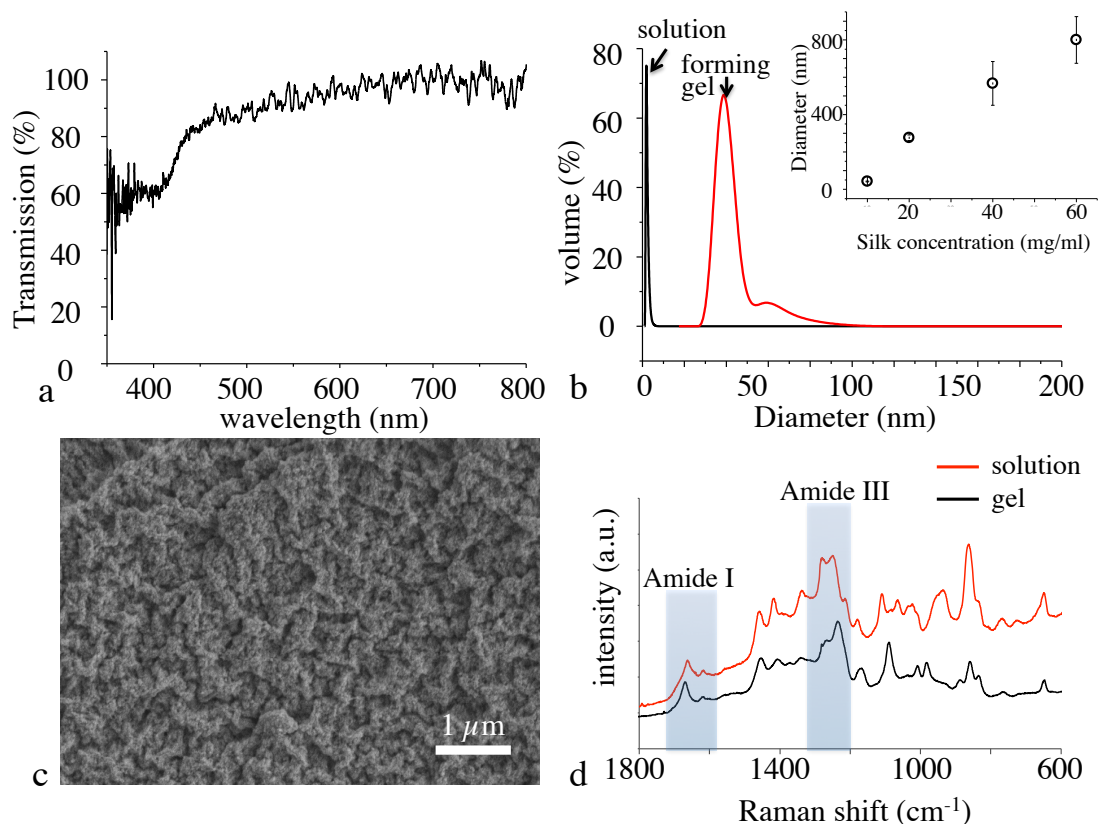
Figure 20. Optical, morphological, and chemical characterization of silk fibroin hydrogels. a) Measurements of light transmission within a silk fibroin hydrogel (4 mm in thickness) showed transparency in the visible spectrum. b) Dynamic light scattering measurements of silk fibroin solution (10 mg/ml) (black line) and of the forming silk fibroin gel (red line) were used to evaluate particle size within the two silk fibroin materials. While silk fibroin micelles (solution state) were sharply centered at circa 2 nm, aggregation of silk molecules during sol-gel transition resulted in an increase in the average particle size to 42 nm. The average particles diameter of the forming gels was also found to be dependent on the initial concentration of the silk solution (inset figure). c) SEM micrographs of the silk fibroin hydrogel revealed a nanostructured material, with morphological features of less than 100 nm. d) µRaman spectroscopy of silk fibroin solution and of silk fibroin gels depicted their amorphous (Amide I centered at cm⁻¹ and Amide III centered at cm⁻¹) and crystalline (Amide I centered at cm⁻¹ and Amide III centered at cm⁻¹) structure, respectively.

Dynamic light scattering (DLS) measurements showed that mixing silk fibroin solution at concentrations ranging from 10 to 15 mg/ml with various polar organic solvents (i.e. acetone, ethanol, methanol, isopropanol) drives the assembly of silk

micelles into submicron-sized particles (<100 nm) (**Figure 20b**), which is a unique feature when compared to previously reported larger fibroin particles (in the 100-5,000 nm range) obtained through the exposure of silk solutions at higher concentrations (>20 mg/ml) to alcohols and ketones. These data are also consistent with a previously reported study, where silk fibroin precipitation in an acetone reservoir allowed for the formation of uniform silk nanoparticles (98 nm diameter, polydispersity index 0.109), which were used as a controlled drug release system for chemotherapeutics.[169] By leveraging the sol-gel transition, we developed an easy, fast and robust method to form nanoparticle-based silk hydrogels by mixing two parts of silk fibroin solution (average molecular weight of 100 kDa, 10 mg/ml) with one part of acetone, where the choice of organic solvent, silk fibroin solution parameters, and the relative concentration of silk fibroin to organic solvent were selected to maximize gel integrity and transparency (**Figures 21, 22, 23a**).
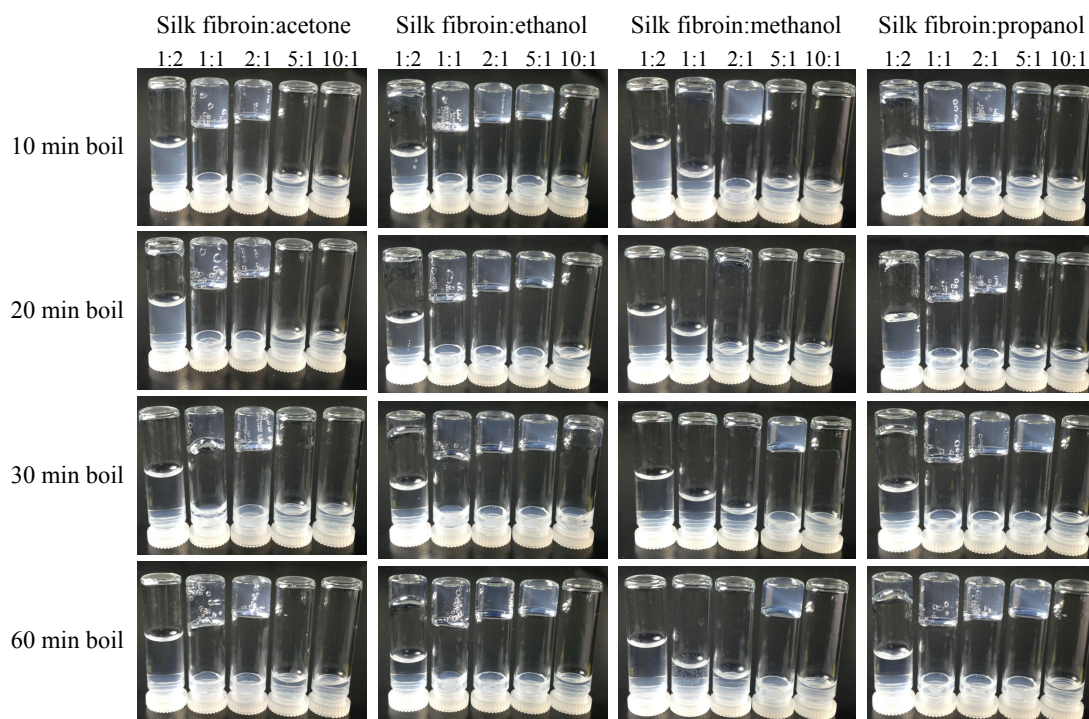
Figure 21. Effects of polar organic solvent treatments and silk fibroin boiling time at the point of sericin removal and silk fibroin:solvent ratios on gel formation. Original concentration of silk fibroin in water solution was 10 mg/ml and pictures were taken after one hour of treatment with organic solvents.
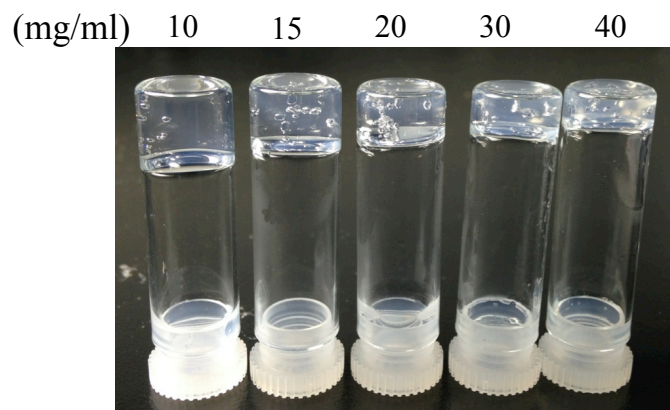
Figure 22. Gelation of silk fibroin solution in acetone at increasing silk fibroin concentrations. A concentration-dependent increase in light scattering was visible. The mass of silk fibroin was maintained constant.
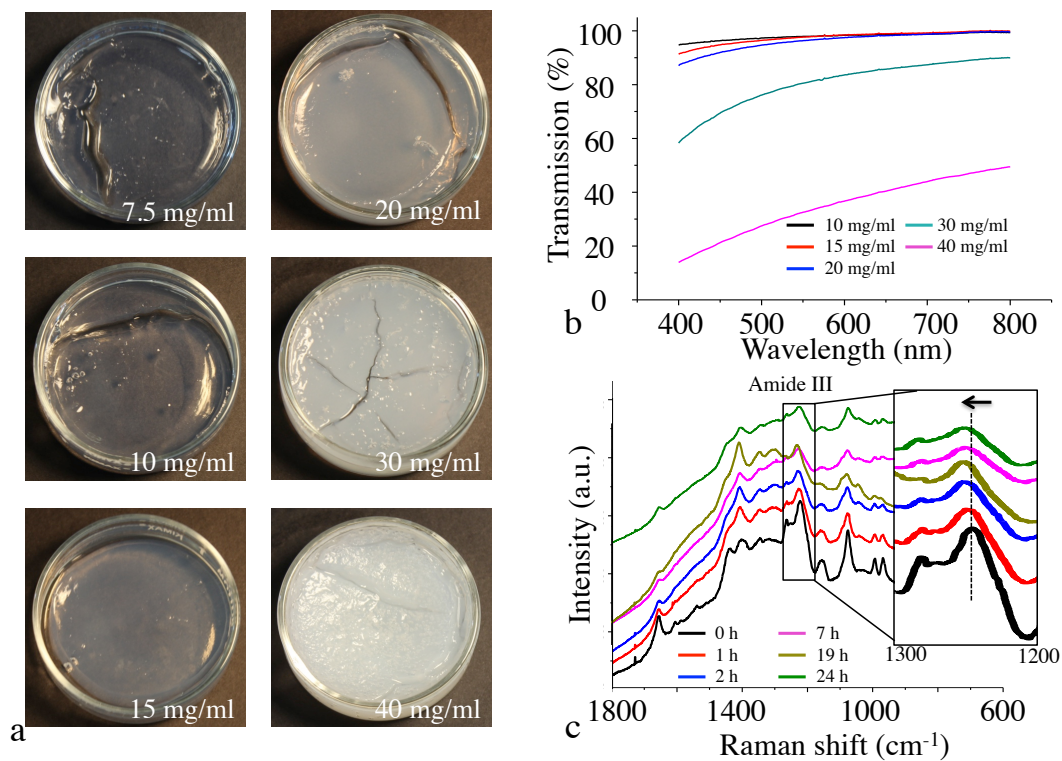
Figure 23. Effect of silk fibroin concentration and EDTA exposure time on silk fibroin hydrogels. a) Photographs of silk fibroin hydrogels obtained through gelation at varying concentrations of silk fibroin solution in a 40 mm wide Petri dish. A concentration dependent increase in light scattering was visible and b) was quantified through optical transmission measurements. Optical clarity was maintained for silk fibroin concentrations < 15 mg/ml. c) Raman spectra of silk fibroin hydrogels at increasing conditioning times in EDTA solution revealed a time dependent blue shift of Amide III beta sheet peak at 1230 cm^{-1}, indicating changes in the structural conformation of the silk protein.

Acetone was successfully removed during processing (**Figure 24**), and gelation in acetone provided enhanced transparency when compared to alcohols (**Figure 21**). In addition, silk fibroin concentration dictated the dimension of the silk particles within the forming hydrogel, and only silk solutions ≤ 15 mg/ml allowed to control silk fibroin particle diameter under 200 nm, resulting in optically clear hydrogels (**Figure 21**). By modulating silk fibroin molecular weight (MW) at the point of sericin removal from the raw fiber, silk fibroin solutions with an average MW of 100 kDa (corresponding to 30 minutes boiling time[158]) provided the best trade-off between gel formation and transparency (**Figures 21, 22**). The nanostructures of transparent silk hydrogels was also evident by scanning electron microscopy, which depicted the assembly of silk fibroin in materials with morphological features less than 100 nm (**Figure 20c**). The significance of material nanotopology has been previously demonstrated for stem cell differentiation,[170] cell adhesion,[171] and metabolic activity[172] and the fabrication of nanostructured silk fibroin hydrogels through this gelation may be useful to probe biological activity.
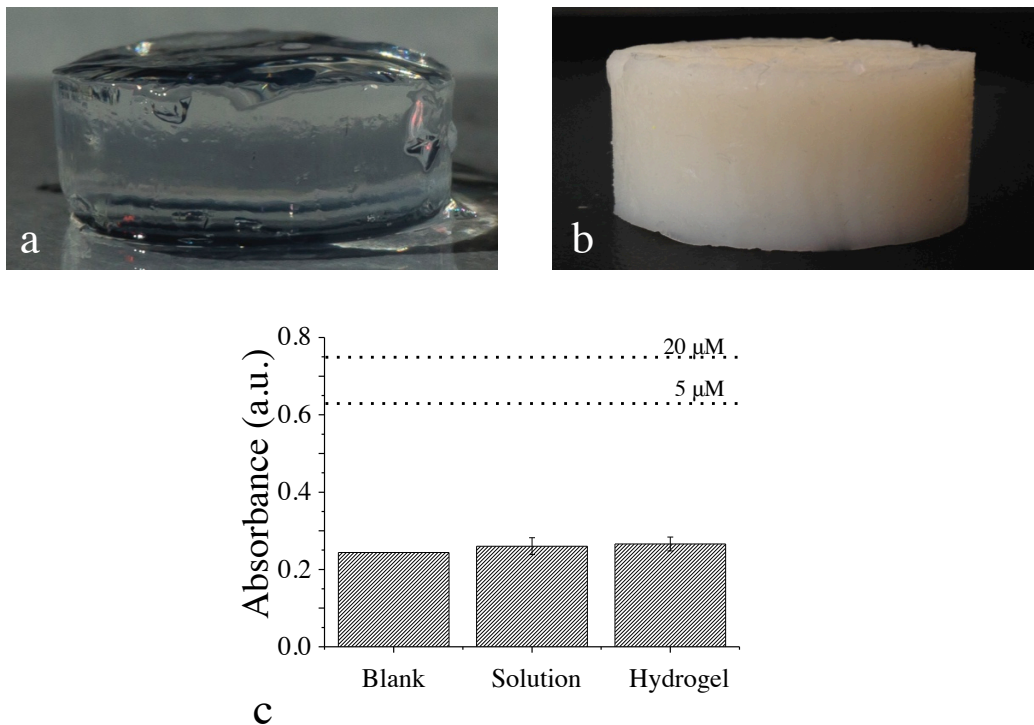
Figure 24. Macroscopic comparison between silk hydrogels obtained through acetone based gelation and through sonication. a) Image of silk hydrogel obtained through acetone based gelation depicts a transparent hydrogel. b) Image of a sonicated silk hydrogel, with the typical white color due light scattering. c) Absorbance measurements of acetone in silk hydrogels compared to silk solution and a water blank. Lowest detected physiological metabolized acetone is 15 µM.

Effect of EDTA conditioning

µRaman measurements corroborated the amorphous to crystalline conformational change of silk fibroin during the sol-gel transition, as the Amide I and III scattering peaks of the protein shifted upon gelation from wavenumbers attributed to the amorphous silk (1661 cm^{-1} for Amide I, 1251 and 1276 cm^{-1} for Amide III) to beta-sheet features (1669 and 1230 cm^{-1} for Amide I and III, respectively) (**Figure 20d**).[173,174] The control of crystallinity enables the modulation of the protein biodegradation *in vivo* and *in vitro* from hours to months and years.[175–179] It is in fact hypothesized that enhanced

crystallinity corresponds to a more packed, hydrophobic, structure that decreases accessibility by metalloproteinases (e.g. MMP1, MMP3, MMP9, MMP 13) and other proteolytic enzymes (e.g. chymotrypsin, trypsin) to cleavage sites in the protein.[180] Concurrently, the modulation of crystallinity allows for the regulation of mechanical properties of the material as the expulsion of water from the protein structure together with the formation of inter-molecular hydrogen bonds result in enhanced elastic modulus and yield strength.[181] To exploit the unique regulation of silk fibroin-based materials properties with hydrogels, it is common to modulate beta-sheet formation by exposing silk fibroin hydrogels to alcohols (e.g. ethanol and methanol).[108] However, this type of treatment did not result in any significant impact effects on the conformation of the protein or on the mechanics of the hydrogels fabricated through gelation (data not shown), as the dehydration of the protein that drives the amorphous to crystalline transition was already achieved during the initial exposure to acetone during the sol-gel transition. Indeed, we pursued an unprecedented methodology to control fibroin crystallinity upon gel formation, which was predicated on the presence of salt bridges formed by metal ions inherently present in the silk fibroin structure and that perturb intermolecular bonding between silk fibroin nanoparticles.[182,183] We hypothesized that the exposure of silk fibroin hydrogels to solutions of aminopolycarboxylic acid, such as EDTA, would chelate the metal ions involved in the formation of salt-bridges, resulting in enhanced intermolecular bonding between the nanoparticles. EDTA has in fact a strong tendency to form stable complexes with metal ions and in particular with four of the six major metallic ions (Na^+, K^+, Mg^{2+}, Ca^{2+}, Cu^{2+}, and Zn^{2+}) in the secretory pathway in *B. mori*.[182] To test this hypothesis, silk fibroin hydrogels were exposed to 20

mM EDTA solution up to 24 hours and the changes in protein secondary and tertiary structures were determined by μRaman spectroscopy. The analysis of the protein μRaman scattering in the Amide III region (1300-1200 cm^{-1}) showed a time-dependent shift of the fibroin crystalline Amide III scattering peak to 1230 cm^{-1} (**Figure 23c**).

Mechanical characterization of hydrogels

Compressive tests were carried out to evaluate the effect of the EDTA treatment on the mechanical properties of the hydrogels. **Figure 25** illustrates representative stress-strain curves at different crosshead speeds for increasing conditioning times in EDTA. All samples showed the densification behavior typical of soft material, where low compressive stress generates high material deformation. The typical viscoelastic behavior of silk hydrogels was also depicted, as increased crosshead speeds corresponded to increased stiffness. Silk fibroin hydrogels exposed to EDTA solution showed a time-dependent enhancement of mechanical properties; both compressive strength (**Figure 25a**) and compressive modulus (**Figure 25b**) increased. The time-dependent enhancement of mechanical strength was associated only with EDTA and not from the trizma base (data not shown). In particular, by controlling the exposure time to EDTA it was possible to regulate the compressive modulus of the hydrogels within a range spanning two orders of magnitude (from 0.4 ± 0.183 to 11.5 ± 2.6 kPa), which correspond to the stiffness of many body tissues ranging from the brain to the muscle.[39-41] Indeed, EDTA treatment of silk fibroin hydrogels not only allows for the modulation of the degree of crystallinity of the protein, which has been previously reported to control

material biodegradation, but also to regulate the hydrogel mechanical properties, which impacts cell differentiation and overall cell behavior.
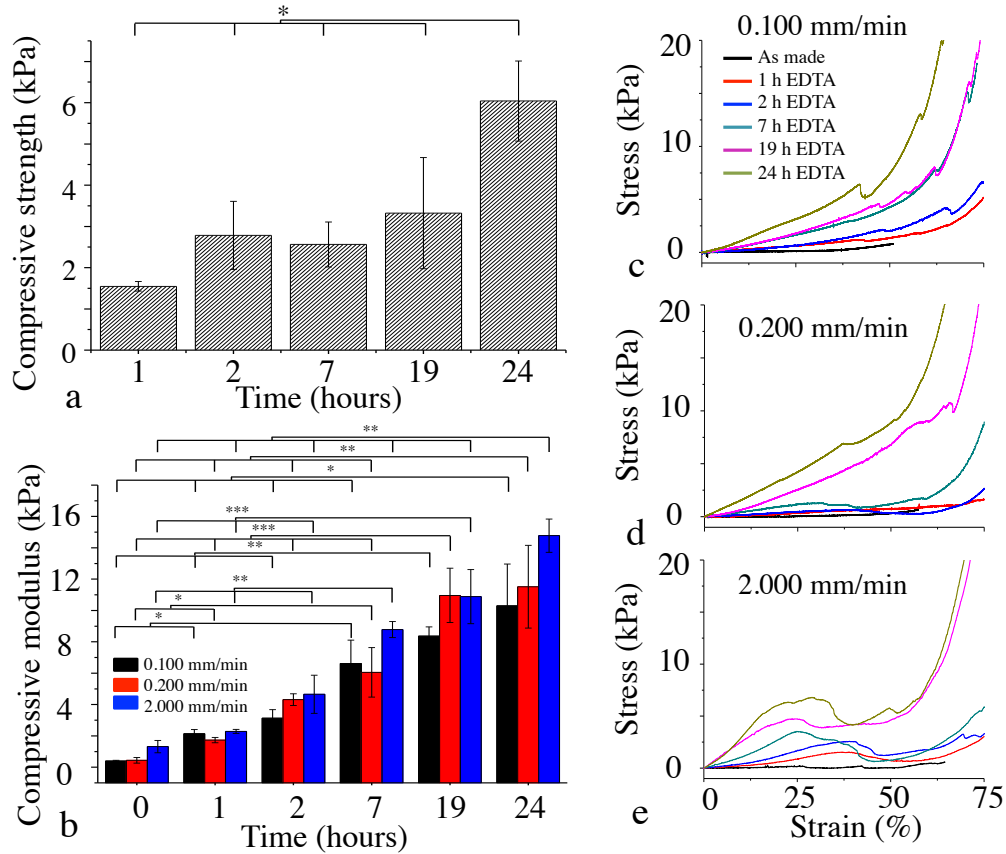
Figure 25. Mechanical characterization of silk fibroin hydrogels. a) Compressive strength of silk fibroin hydrogel at crosshead rate of 2.000 mm/min as a function of treatment in 20 mM EDTA solution. To longer EDTA treatment corresponded an increased compressive strength as a result of the hydrogel crosslinking. b) Compressive modulus of silk fibroin hydrogels as a function of conditioning time in a 20 mM EDTA solution for different crosshead rates (* $p < 0.05$, ** $p < 0.01$, *** $p < 0.001$). c-e) Representative unconfined compressive stress-strain curves of silk colloidal hydrogels at 0, 1, 2, 7, 19, and 24 hours in 20 mM EDTA solution for crosshead rates of (c) 0.100 mm/min, (d) 0.200 mm/min, and (e) 2.000 mm/min. All the specimens tested were 4 mm thick.

Biological characterization of hydrogels

As a preliminary evaluation of biocompatibility, human dermal fibroblasts were cultured up to 28 days on silk fibroin hydrogels obtained by this gelation and conditioned with EDTA for 24 hours. Confocal laser scanning microscopy images were taken of the dermal fibroblasts at day 7, 14 and 28 after staining with calcein-AM fluorescein and EtBr-1 deoxyribonucleic acid binding (live/dead® assay) (**Figures 26 and 27**). At day 7 (**Figure 26**), cells were viable (green) and attached to the surface of the hydrogel with negligible appearance of dead cells (red). Confocal imaging within the scaffolds allowed the visualization of living cells 1 mm into the gels, showing that the human dermal fibroblasts penetrated the hydrogel material and remained viable. In addition, SEM analysis of the cell-seeded hydrogels at day 7 showed deposition of extracellular matrix with a nanofibrillar structure, which can be associated to the formation of type I collagen from a fibroblastic cell-line. Prolonged culture times (days 14 and 28) of human fibroblasts on the silk fibroin hydrogels showed cell alignment and increased production of fibrillar nanostructures in the extracellular space (**Figure 26 and 27**).
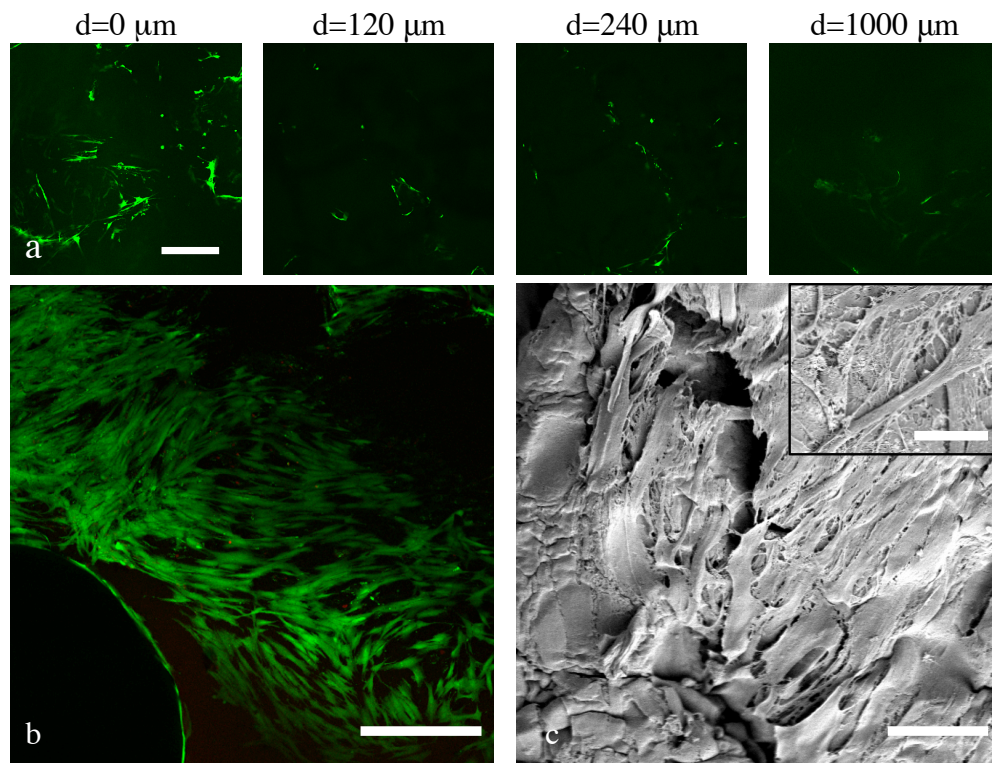
Figure 26. Cytocompatibility of silk fibroin hydrogels. Human dermal fibroblasts (HDFa) were cultured on silk fibroin hydrogels. a) Confocal microscope images using live/dead assay revealed the presence of HDFa at different depths within the hydrogel at day 7 in culture. Subsequent images signify a depth scan at the surface (depth equal to 0 μm), 120 μm from the surface, 240 μm from the surface, and 1000 μm from the surface. Scale bar is 375 μm. b) Maximum intensity projection of HDFa on silk fibroin hydrogels at day 7 in culture showed that fibroblast were well spread on the hydrogel. Scale bar is 375 μm. c) SEM micrograph of HDFa cultured on silk fibroin hydrogel at day 7 showed production of extracellular matrix by cell activity (inset image). Scale bar is 30 μm for the main image and 10 um for the inset one.
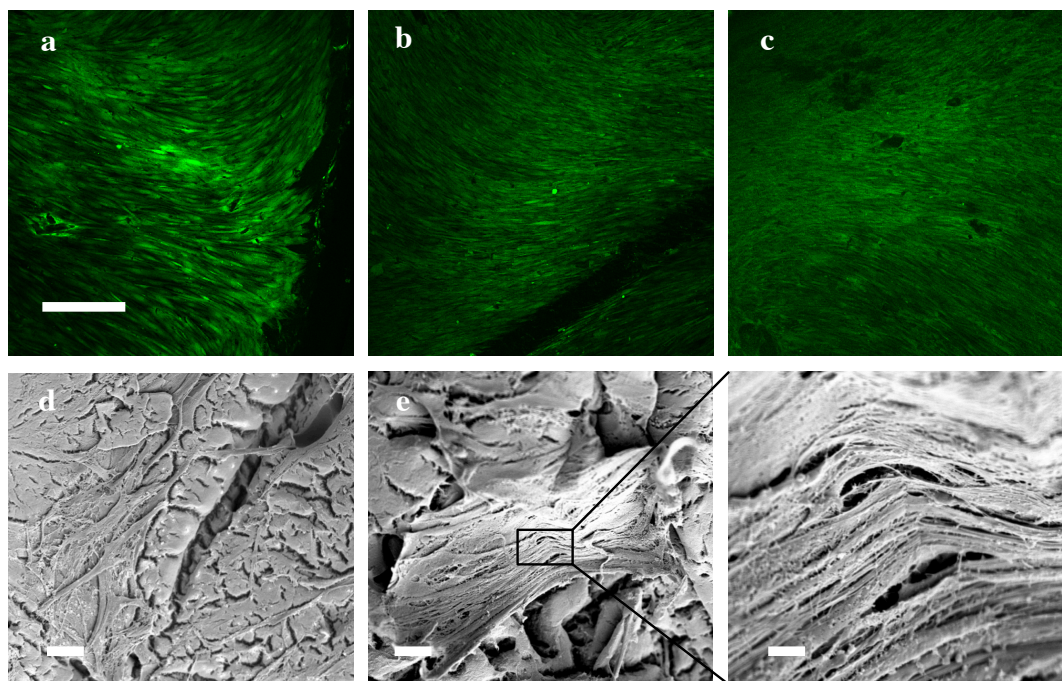
Figure 27. Cytocompatibility of silk fibroin hydrogels. Human dermal fibroblasts (HDFa) were cultured on silk fibroin hydrogels a-c) Maximum intensity projection of HDFa stained with live/dead assay at (a) day 7, (b) day 14, and (c) day 28 in culture showed that fibroblast were well spread on the hydrogel for all the time points considered. Scale bar is 375 μm. SEM micrographs of the cellular gels at d) day 7 and e) day 28 were collected to investigate cell morphology and the production of extracellular matrix. Scale bar is 20 μm. The enlarged micrograph shows close up of extracellular matric deposition. Scale bar is 2 μm.

Optically clear hydrogels can find use in regenerative medicine for transparent tissue scaffolds. As a proof of principle, silk fibroin hydrogels were seeded with human cornea epithelial cells (HCECs) to evaluate potential use as cornea-equivalent materials for epithelium regeneration. Type I collagen was chosen as a positive control material, due to the material track record in human clinical phase (**Figure 28**).[42-44] A combination of confocal laser microscopy and live/dead® assay on HCEC-seeded silk fibroin hydrogels showed cell viability and proliferation over 10 days, with no appreciable difference when compared to collagen hydrogels. HCECs cultured on silk fibroin hydrogels also formed a

visible epithelium at day 7 (**Figure 29**). In addition, metabolic activity of HCECs seeded on silk fibroin and collagen hydrogels was measured as a function of culture time at days 1, 3, 7, and 10 using reduction of AlamarBlue[TM]. The HCECs cultured on the silk fibroin hydrogels showed a similar (days 1, 3, 10, $p > 0.05$) or increased (day 7, $p < 0.05$) metabolic activity, when compared to HCECs cultured on collagen hydrogel counterparts. Optical transmission measurements of HCEC-seeded silk fibroin hydrogels at day 10 showed no appreciable difference to acellular counterparts, indicating that the hydrogels preserve transparency even with the formation of an epithelium (**Figure 30c**) in contrast to similar measurements taken on HCECs-seeded collagen scaffold, which showed decrease in transparency of collagen hydrogels.
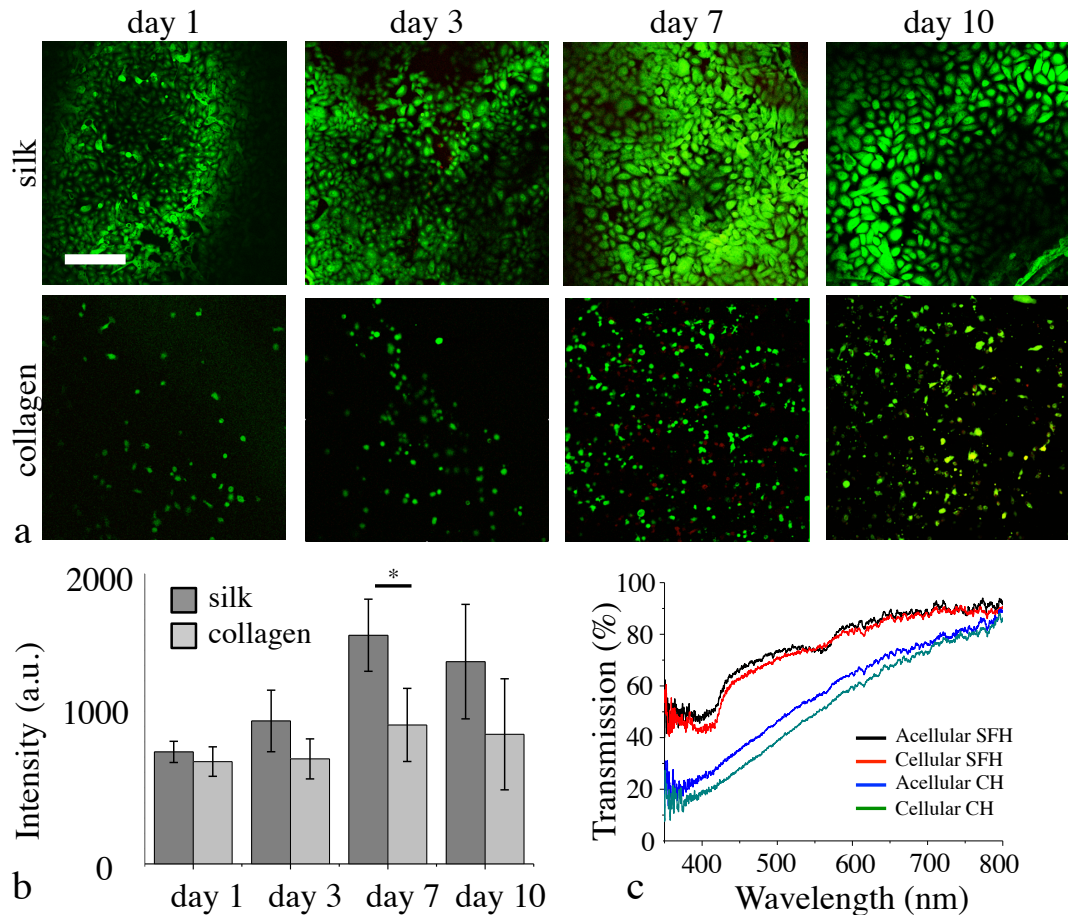
Figure 28. Biological characterization of silk fibroin hydrogels. Human corneal epithelial cells (HCECs) were culture on transparent silk fibroin hydrogels. Collagen hydrogels were used as controls. a) Confocal microscopy of live/dead assay on HCECs cultured on the surface of silk fibroin and collagen hydrogels at day 1, day 3, day 7, and day 10. Cells were viable and proliferated during the culture time considered. Scale bar is 375 μm. b) HCECs metabolic activity as measured by AlamarBlue[TM] reduction up to day 10 in culture (* $p < 0.05$). c) Light transmission of acellular and HCECs seeded silk fibroin and collagen hydrogels (SFH and CH, respectively) at day 10 of culture. The observed decrease in light transmission of the silk hydrogel when compared to the results shown in Figure 21 is associated with loss due to the cell culture media.
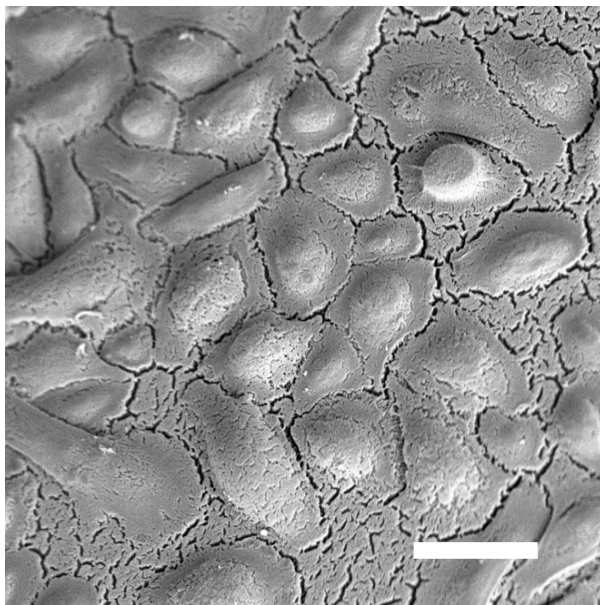
Figure 29. SEM micrograph of epithelial cornea cells cultured on the silk hydrogel at day 7 in culture. Scale bar is 40 μm.

Conclusion

In conclusion we have explored organic solvent gelation as a method to fabricate silk fibroin hydrogels, which possess distinct properties from the previously reported methodologies to induce sol-gel transitions with this macromolecule. Control over hydrogel nanostructure, crystallinity, mechanical properties and transparency provides new options for the use of silk hydrogels in regenerative medicine and added utility for

transparent tissues, as well as uses related to optics-related applications in biosensing, and

optogenetics studies.

CHAPTER 4: NANOSTRUCTURED SILK FIBROIN AFTER NEAR-CRITICAL POINT AND SUPERCRITICAL CO₂ DRYING

Abstract

Silk fibroin, from the *Bombyx mori* silk worm, is a well-known biopolymer that can be processed into several different material forms such as fibers, films, foams, sponges, and hydrogels with potential applications in areas ranging from regenerative medicine to sensors. Functional biomaterials are important in the field of bionanotechnology because of the number of valuable properties including self-assembly, strength, and stability. Current processing with silk fibroin to produce nanostructured materials lacks the capability to create functional 3D forms without using a sacrificial material, conforming to similar surface features, or using direct writing. Nanostructures are also an important characteristic where silk in the nanofiber form has shown sensing potential. Low density and high porosity are two characteristics that are necessary in gas sensing materials since the gas can easily fill the pores and more efficiently contact the solid network/skeleton. Here, we examine the transformation of silk fibroin, which has emerged as a promising polymer material due to its biocompatibility, biodegradability, and ease of functionalization, into nanostructured materials after near-critical point and supercritical carbon dioxide ($SCCO_2$) drying. The high-pressure during $SCCO_2$ drying forces the *B. mori* silk fibroin protein into nanofibers to be used as functional materials for biomedical applications. Applying different pressures while drying with CO_2 to silk gels was used to examine the morphological and semi-crystalline nanostructure changes. Controlling the silk concentration combined with the specific hydrogel synthesis was optimized to

improve the transparency of the silk fibroin aerogels while stabilizing the activity of enzymes to preserve their biological function. In addition, adding PtTFPP as a fluorescent molecule was added to enhance the silk fibroin aerogel's ability to measure gaseous oxygen and showed sensing ability that was more advanced compared to silk films and dried xerogels.

Introduction

The use of silk fibroin as a material for biomedical, optical, and electronic applications has been established by its different material forms such as fibers, films, foams, particles, and hydrogels depending on the processing conditions of the regenerated aqueous formulation.[160,184] Depending on the self-assembly of the crystalline solid or solution, silk fibroin materials can form nanostructures to be used for optics, electronics, and biomaterial applications.[119,120] For sensing applications, the film format of silk fibroin has been used due to its preservation of heat-labile biomolecules, transparency, and robust mechanical properties allowing the fabrication of nanostructured patterns to interface features with biology.[45,108] Other common forms that provide nanodimensions, such as electrospun mats, are characterized by high optical loss due to scattering making them less ideal as sensing platforms.[4,119,185]

Despite several applications of silk fibroin in biomedical engineering, the unique nanofiber structure defining the superior mechanical properties of silk are completely destroyed during silk dissolution in traditional solvents and lack the regeneration of fibers.[186] The process is regulated by the transitions occurring in the amphiphilic domains of the protein where long hydrophobic crystallizable blocks and short hydrophilic spacers modulate intermolecular hydrogen bonded beta-sheet formation in the presence of water.[115] The encouragement of macromolecular interactions from the hydrophobic side chains initiating hydrogen bonding occurs after exposure of silk solution to electric fields,[187] changes in pH, heat, water removal, shear forces, or polar solvents.[67] However, alterations also respond to changes in pressure forming intermolecular bonded nanofibers during water removal.[186] The pressure used to form these changes can occur during near-

critical point drying and supercritical drying of gels to produce forms with nanofiber structures.

Pressure is one physical parameter that is not a common variable used to examine changes in protein nanostructure, particularly at standard pressure and temperature.[12] A protein's structure is altered by changes to its environment, whether it is changes in liquid conditions (as discussed in previous chapters), changes in temperature, changes in shear stress, or changes in pressure. Pressure is a unique variable to probe molecules in unfolded and folded states as perturbations depend solely on volume changes relating to the free energy of biomolecules.[101,188] Pressure is a powerful variable to study protein folding, protein stability, and the dynamics of folded protein intermediates that has the ability to alter the morphology of specific structures.[19]

Protein stability and function are based upon its ordered folding structure.[189] The ordered structure of proteins involves specific folds to minimize free energy, while also organizing into a three-dimensional form to maximize function. While function is an important component, folding into stabile forms is as important. There is a balance between stability and function and it is hypothesized that amino acid sequences that contribute to catalysis are not optimized for protein stability.[189] Recent studies with silk fibroin suggest it is possible to be used as a stabilizing matrix because the large hydrophobic domains of silk interspersed with small hydrophilic regions form semi-crystalline "nanopocket" domains. These regions can immobilize bioactive molecules and improve their stability by minimizing water content and reducing chain mobility preventing transitions to native states.[104,105] Altering the crystalline fraction associated

with pressure induced crystal lattice changes could improve encapsulation of therapeutic compounds in silk matrices compared to previous results.

Investigating the structure of silk fibroin has been conducted for the past 100 years to better understand silk's unique properties. Silk fibroin's structure is characteristic of pleated beta-sheets as determined by the model presented by Marsh, Corey, and Pauling.[116,190] Various silk structures have been examined concluding all silks essentially have the same orthorhombic crystal lattice composed mostly of amino acids glycine and alanine.[116] Silk is composed of repeated regions of glycine, alanine, and serine, and it was later suggested by Meyer, Fuld, and Klemm that the serine residues can take the place of the alanine in crystalline regions.[191,192]

Changes at the molecular structure can be measured by methods such as polarized light microscopy and X-ray diffraction. Polarized light microscopy is a method to provide information regarding crystal structure based on birefringence. Birefringence is the property of a material having a refractive index that varies on the polarization of light, and it is used to determine the anisotropy of crystal structures in materials. Applying a dye, such as Congo red, can enhance the observed birefringence making structures unknown to the observer more visible. Polarized light microscopy is capable of providing qualitative and quantitative information regarding color absorption and optical path length boundaries between crystals with different refractive indices. Additionally, X-ray diffraction is a method to determine the atomic and molecular structure of a crystal where the crystalline structures diffract a beam of X-rays producing a pattern. X-ray diffraction is the principal method for characterizing atomic structures of new materials and distinguishing materials that appear similar. As silk is one of the simplest fibrous proteins

containing a high number of small amino-acid residues that can fold into highly ordered structures, X-ray diffraction patterns are the most suitable for determination of the structure of fibrous proteins.[193,194] Many researchers have examined the diffraction pattern of silk in the raw and regenerated state and after applying shear on the raw dope.[116] However, little work has been conducted to examine the effects of pressure on silk gel states and how changes in pressure alter crystal structure.

Biological entities (e.g. cells) and chemical sensitive molecules can capitalize on silk fibroin nanostructures, particularly nanofibers and high porosity, as three-dimensional microenvironments to mimic extracellular matricies,[58] to mimic biological systems, or to build novel optical interfaces. Nanofibers and high porosity are the main characteristics of aerogels which have been shown as platforms for chemical sensing.[75,85,97] Combining nanofiber formation with the well-established mechanical, biochemical, and biological properties of silk fibroin would create a new form for this biomaterial, producing highly porous constructs with high surface area for enhanced biomedical applications.

In this chapter, we report a method to assemble regenerated silk fibroin into nanofibers after near-critical point and supercritical CO_2 drying, which enables the formation of a translucent silk fibroin aerogels with defined shapes and dimensions. Additionally, near-critical point and supercritical CO_2 drying of silk fibroin gels alters the crystal structure of silk fibroin. Additionally, supercritical drying produces silk aerogels that maintain the activity of biological compounds to be used as fluorescence gas sensors in a degradable biological protein. Change to the crystal structure of silk fibroin alters the stability of entrapped enzymes due to the increased lattice packing of the molecules.

[104,105] We intend to show enzyme stability associated with changes in silk crystal structure occur through different pressure drying.
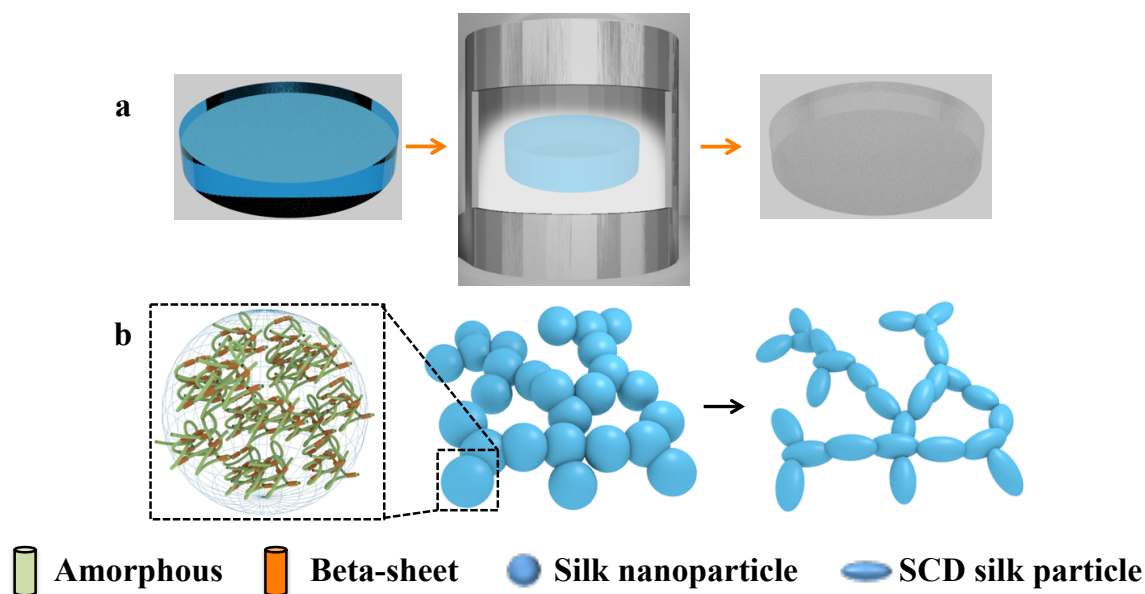
Figure 30. Fabrication of silk fibroin nanofibers. a) Free-standing silk fibroin hydrogel are formed, followed by dehydration in ethanol, and supercritical CO_2 drying leaving a free-standing silk fibroin aerogel. b) Schematic representation of conformational changes within silk fibroin during sol-gel transition. Silk fibroin possesses an amorphous structure (mostly random coils) and is arranged into micelles. During gelation, the silk fibroin experiences a combination of amorphous-to-crystalline conformational changes together with aggregation resulting in the formation of silk particles. These arrange together in the presence of water forming a free-standing hydrogel structure. During supercritical CO_2 drying, nanofibers are formed causing a morphological change of the silk particles.

Experimental

Materials

Silk fibroin solution preparation

Silk fibroin solution was prepared as previously described (**Figure 30**).[108] *B. mori* silkworm cocoons were boiled for 30 minutes in a solution of 0.02 M Na_2CO_3 to remove the sericin glycoprotein. The extracted fibroin was rinsed in deionized water and set to

dry for 12 h. The dried fibroin was dissolved in 9.3 M LiBr solution at 60°C for 3 h. The solution was dialyzed against deionized water using a dialysis cassette (Slide-a-Lyzer, Pierce, MWCO 3.5K) at room temperature for 2 days until the solution reached a concentration of ~60 mg/ml. The obtained solution was purified using centrifugation.

Silk aerogel synthesis

Acetone Optima (Fisher Scientific) was used to synthesize the initial hydrogel. Acetone was set in a glass Petri dish and silk solution with varying concentration of 30 minute silk solutions were added drop wise into the acetone bath. The ratio of silk solution to acetone was never more than 2:1 because the addition of more silk fibroin produced less transparent gels. The acetone was evaporated at room temperature for 12 h while adding deionized water to prevent the hydrogel from collapsing (**Figure 30b**). The hydrogel was soaked in a 20 mM solution of EDTA (pH=8.5, Sigma Aldrich) for 24 h to improve the hydrogel mechanical properties. The hydrogels were rinsed in deionized water followed by dehydration in a series of ethanol rinses at concentrations of 50%, 70%, 80%, 90%, 95%, 100%, and 100% for 30 minutes to be prepared for near-critical point and supercritical carbon dioxide ($SCCO_2$) drying conducted at 50°C (**Figure 30c**). The pressure vessel maintained the same temperature and fluid extraction rate when the pressure was varied to determine nanofiber formation.

Morphological characterization of the alcogels without drying with $SCCO_2$ was obtained by drying the samples in hexamethyldisilazane (HMDS). Samples were exposed to a series of HMDS baths at 70%, 90%, 100%, and 100% for 30 minutes to ensure

complete saturation. Samples were then left to dry in a chemical hood for 12 hours to allow complete evaporation and then immediately sputter coated for SEM analysis.

Measurements

Morphological measurements

SEM images were taken by a Supra55VP FESEM (Zeiss) using the SE2 detector. Samples were sputter coated using platinum/palladium or gold and imaged at 4 kV.

Density/porosity measurements

The bulk density of the silk aerogels was calculated by weighing the samples and dividing by the sample volume using a standard laboratory bench top scale.

Transmission measurements

Spectra were taken using a vis/near-infrared fiber-optic spectrometer (USB-2000, Ocean Optics). White light was propagated through the fiber to illuminate the sample. The transmitted light was coupled into a fiber tip opposite to the spectrometer. The distance between the illumination source and the collection tip was fixed at 7 mm. All samples had a thickness of 4.2 mm.

Mechanical testing

The compressive properties of samples of 4 mm in diameter were measured using an Instron 3366 testing frame (Instron, Norwood, MA) with a crosshead speed of 2 mm/min and a 100 N capacity load cell. Samples were conducted in air between force plates until

maximum compression was reached. The linear elastic modulus was calculated using a least-squared fitting in the linear region of initial compression up to a 20% strain point.

FITR measurements

FTIR analysis of samples was performed in a JASCO FTIR 6200 spectrometer (JASCO, Tokyo, Japan) in attenuated total reflectance (ATR). Hydrogels were let to dry on a glass slide. For each sample, 64 scans were coded with a resolution of 1 cm^{-1}, with a wavenumber range from 4000-600 cm^{-1}. Fourier self-deconvolution (FSD) of the infrared spectra covering the Amide I region (1595-1705 cm^{-1}) was performed by Opus 5.0 software. The second derivative was applied to the original spectra in the Amide I region with a nine-point Savitsky-Golay smoothing filter. Deconvolution was performed using Lorentzian line shape with a half bandwidth of 25 cm^{-1} and a noise reduction factor of 0.3. Apodization with a Blackman-Harris function was performed automatically at the same time in the software.

Congo Red staining and imaging

Silk fibroin samples were prepared using the method as described above and mixed in warm water and agitated for several hours. Liquid samples (10 μl) of the aggregated suspension were cast onto glass slides and set to air dry at room temperature. When the samples were dry, 200 μl of saturated Congo Red solution in 80% ethanol with saturated NaCl was added to the dried protein sample and blotted to remove the excess solution and dried at room temperature.[195]

Samples were imaged using a CRI Nuance multispectral camera (PerkinElmer, Waltham, MA, USA) scanning from 450-700 nm with 50 nm step intervals. Polarized light microscopy was used to image each sample with two linear polarizers crossed at a 90-degree angle to each other.

X-ray diffraction measurements

Silk materials were prepared as described above. Measurements of the X-ray diffraction patterns were conducted at room temperatures using an Oxford Diffraction Xcalibur PX Ultra System (Oxford Diffraction Ltd., Concord, MA). The CuK^{α} X-ray beam with wavelength of 1.542 Å was generated at 45 kV/40 mA using an Enhance Ultra in a sealed tube-based system incorporating confocal multilayer optics. The X-ray beam was monochromated and the K^{β} component was removed by means of the double bounce within the confocal optics. The X-ray beam was focused to 0.3 mm x 0.3 mm (full width at half-maximum at detector position). A two-dimensional Onyx CCD detector (Oxford Diffraction Inc., Concord, MA) with pixel size of 121 μm was placed 62 mm from the sample position. Exposure time was 150 s.

Horseradish peroxidase (HRP) stabilization and detection

Prior to hydrogel and aerogel formation, HRP was mixed with silk solution yielding a final concentration of 2.5 U/ml. After supercritical drying the silk fibroin aerogels, samples of the same dimension were separated and stored at different temperatures (4 °C, 25 °C, and 60 °C) along with liquid samples with a concentration of 2.5 U/ml to be measured at different time points. For HRP, 100 μl 3,3',5,5'-tetramethylbenzidine (TMB)

liquid solution (Sigma Aldrich, USA) was added to aerogels samples to monitor a reduction at 370 nm using a microplate reader (SpectraMax M2, Molecular Devices, Sunnyvale, CA, USA).

After supercritical drying the silk fibroin aerogels, samples of the same dimension were separated and stored at 25 °C along with dried samples with a concentration of 2.5 U/ml to be measured at different time points. Aerogel samples were prepared by drying with CO_2 at 750 psi, 1000 psi, 1400 psi, and 1800 psi. For HRP, 200 µl TMB liquid solution (Sigma Aldrich, USA) was added to aerogels samples and left to react for 15 minutes. Controls were the same concentration of HRP dried to a well plate after conditioning in acetone.

PtTFPP oxygen measurements

Prior to aerogel formation, silk fibroin aerogels were dehydrated with a final rinse in 100% ethanol mixed with platinum(II) meso-tetrakis(pentafluorophenyl)porphyrin (PtTFPP) and left for 24 h to ensure PtTFPP attachment to the silk fibroin.

Oxygen measurements were taken using a cuvette reader (SpectraMax M2, Molecular Devices, Sunnyvale, CA, USA) with excitation 405 nm and emission at 645 nm at 0% oxygen saturation and 20% oxygen saturation. Aerogel samples were cycled repeatedly at different oxygen saturations in one minute intervals to monitor the cyclical behavior of the fluorescence intensity. Samples were kept at different temperatures to calculate any changes in degradation. Silk films and ethanol solutions were used as controls.

Results and discussion

Effect of SCCO$_2$ drying on silk fibroin morphology

SCCO$_2$ drying is an environmentally benign alternative to fashion various biomaterials facilitating porosity, as well as processing thermally sensitive protein therapeutics.[101] Previously reported results state that pressure perturbations can convert protein molecules into nanofibers. Under high pressure conditions silk experiences a change in polymer morphology by which silk nanoparticles composing the hydrogel were merged together.[18,196,197] The process in nanofiber formation is associated with CO$_2$ molecules interacting with basic carbonyl groups in the polymer molecules reducing chain-chain interactions and increasing polymer segment mobility.[18] The effect of SCCO$_2$ drying silk fibroin hydrogels (**Figure 31a**, **Figure 31b**) was determined by drying at near-critical pressures and supercritical pressures to determine the pressure of nanofiber formation. Scanning electron microscope (SEM) images of silk gels after exposing silk hydrogels to near-critical point and SCCO$_2$ showed the assembly of silk submicron particles to nanofibers (**Figure 31c-h**). The polymer nanofiber formation was evident by drying a silk hydrogel in hexamethyldisilazane (HMDS), which depicted the assembly of silk fibroin nanoparticles with morphological features less than 100 nm (**Figure 31c**) to the development of nanofibers at increasing drying pressure. SEM images show a highly dense network of silk nanofibers with diameters between 10-20 nm with larger pore dimensions on the order of a hundred nanometers when samples were dried above the critical point of CO$_2$ (**Figure 31h, Figure 32**).
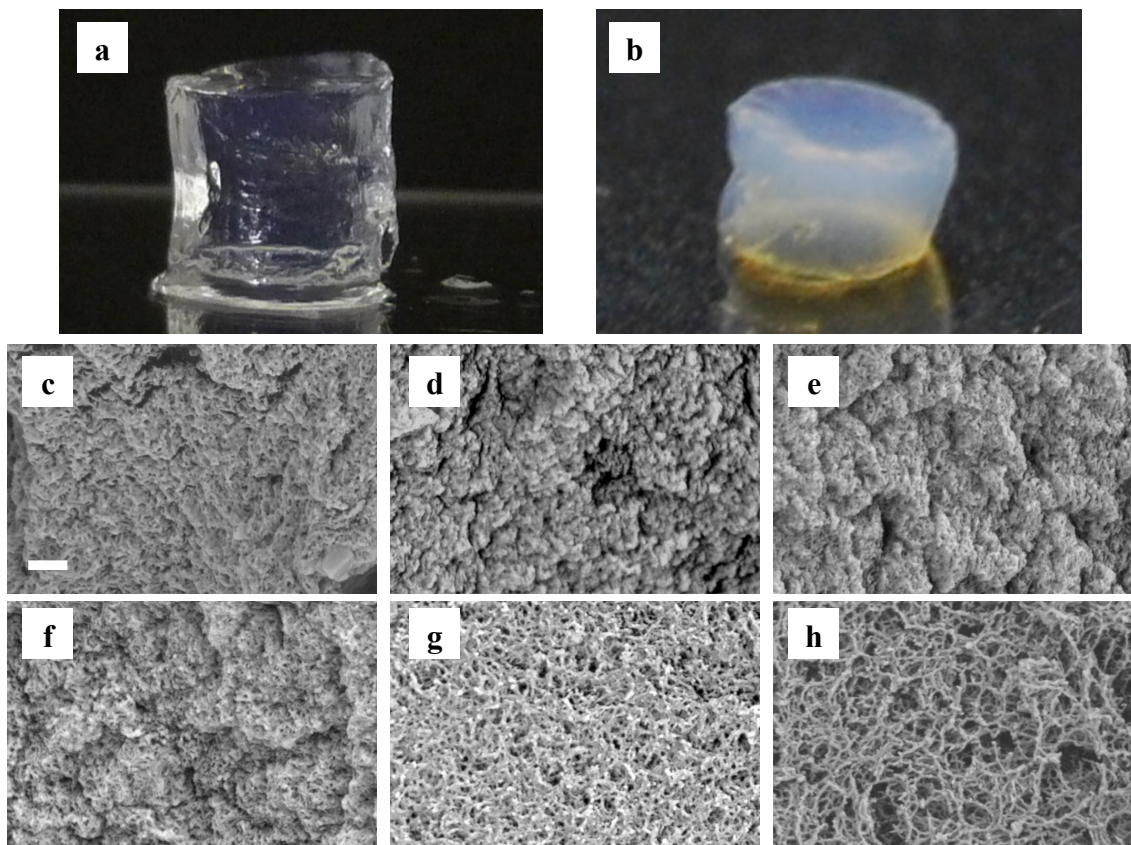
Figure 31. CO$_2$ pressure on silk fibroin gel. a) An image of a transparent, silk fibroin hydrogel formed by mixing reconstituted silk fibroin with acetone. b) Image of a silk fibroin aerogel produced after supercritical CO$_2$ drying. c-h) CO$_2$ pressure drying of silk fibroin gels. The pressure vessel was kept at constant temperature (50 °C) and effluent rate (4 kg/hr) for (c) 0 psi, (d) 200 psi, (e) 500 psi, (f) 750 psi, (g) 1000 psi, and (h) 1800 psi. Scale bar is 200 nm.
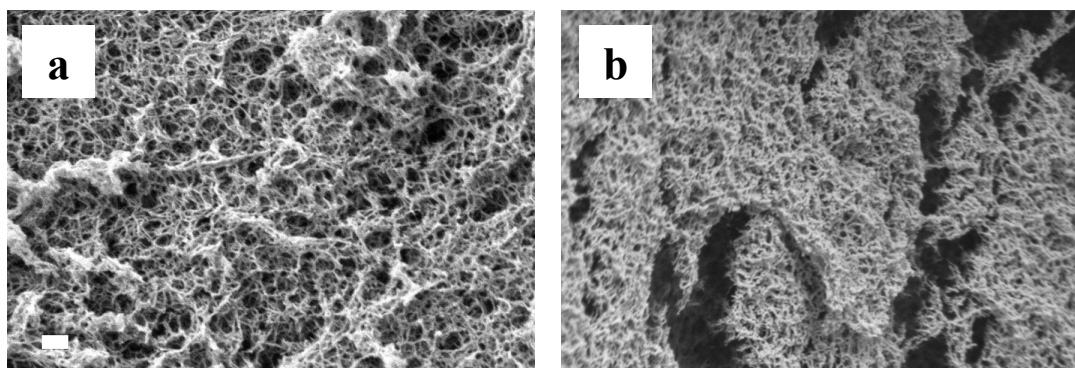
Figure 32. Silk gels dried with CO$_2$ at pressures a) 1200 psi and b) 1400 psi. Scale bar is 200 nm.

The transformation from particle gel to a nanofiber gel is believed to be associated with changes in the protein regarding partial molar volumes, protein folding, and conformational transformations.[101] This data is consistent with previously reported studies where silk fibroin nanofibers synthesis after $SCCO_2$ allowed for the formation of silk aerogels, which were used as a controlled drug release system for ibuprofen.[100] By controlling the hydrogel formation and pressure during drying, we developed a fast and easy method to form relatively translucent, low bulk density, silk aerogels where the gel formation was selected to maximize gel integrity and transparency. By modulating silk fibroin molecular weight (MW) during purification of the raw fiber, silk solutions with an average MW of 100 kDa (proportional to 30 minute boiling time[158]) provided the ideal trade-off between transparency, strength, and bulk density. The associated pressure to induce aerogel formation offers a significant variable to alter protein morphology and structure.

FTIR analysis

Measuring beta-sheet secondary structures is a way to monitor the order or crystallinity of silk fibroin molecules and modulate the degradation of the protein from hours to months and years.[177,179] It has been shown that enhanced crystallinity corresponds to a more packed hydrophobic structure that decreases accessibility to proteolytic enzymes to cleavage sites in the protein.[180] The control of crystallinity allows for the regulation of mechanical properties of the material as well as the ability to stabilize entrapped enzymes. To exploit the unique crystalline structure of silk fibrin

based materials, beta-sheet formation is typically controlled by introducing silk materials to alcohols (e.g. methanol and ethanol).[108] Attenuated total reflectance-Fourier transform infrared (ATR-FTIR) spectroscopy measurements verified the crystalline conformational change of silk fibroin after $SCCO_2$ drying by examining the amide I, II, and III absorption peaks (1750-750 cm^{-1}) of the protein attributed to the beta-sheet features (**Figure 33a**).[195,198] The amide I band occurs in the region between 1600 and 1700 cm^{-1} and assignment of the peak at 1620 cm^{-1} or lower wavenumbers are representative of beta-sheets with strong hydrogen bonding.[195] When measuring the beta-sheet at different pressure dried samples from 0 to 1800 psi, there is a calculated increase in beta-sheet fraction. The pressure driven change in morphology is also observed in changes at the molecular level as shown in a change of beta-sheet fraction from 32-47% for drying at 0-1800 psi samples (**Figure 33b**). The change in beta-sheet fraction can be associated with molecular movement of the silk fibroin molecules to more favorable hydrogen bonding secondary structures forms after the addition of pressure which has been previously hypothesized.
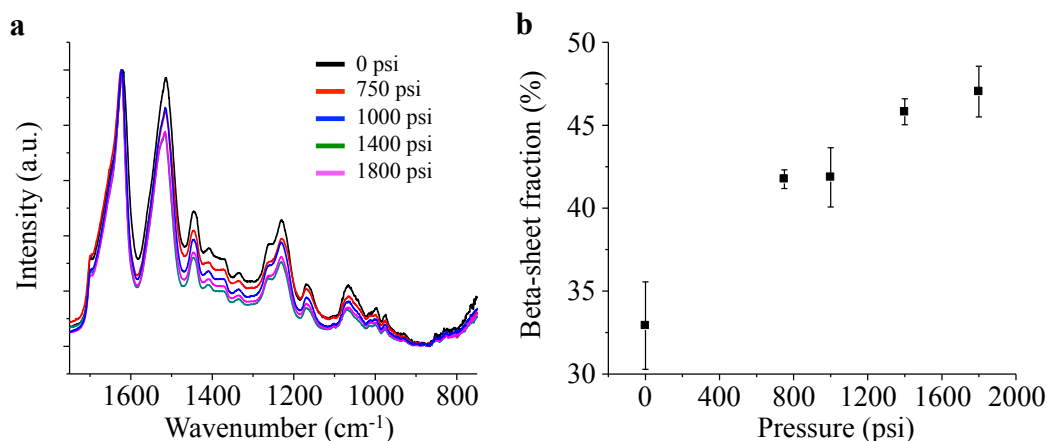
Figure 33. FTIR analysis of silk gels dried at different CO$_2$ pressures. a) ATR-FTIR spectra of silk fibroin samples dried at near-critical point and supercritical CO$_2$ pressures. b) Calculated beta-sheet fraction of silk fibroin samples dried at associated pressures.

Congo Red analysis

Polarized light microscopy was used to characterize the structure of the silk samples as the particles transitioned into a fiber after CO$_2$ drying to provide additional information regarding changes to silk secondary structures that were not capable using FTIR analysis. The highly repetitive primary sequence of silk fibroin makes it desirable among fibrous proteins as it bestows structural characteristics with fibrils.[199] Silk's transition from an unstructured state into a stable beta-sheet structure arranged in a cross-beta pattern perpendicular to the axis of the fibril has been suggest and was tested by staining with Congo Red to search for green birefringence (considered a positive result).[195,200] Fibrils form from a range of storage conditions and their dimensions can be controlled by varying temperature and pH to alter their native protein structure.[201] Pressure is a characteristic perturbant in studies of protein folding and has acted as a new influence to induce fibrils depending on the protein species.[184,202] The analysis of Congo Red stained silk film, and silk gels dried at near-critical pressures ranging from 0-1000 psi were absent of such birefringence (**Figure 34a-f**). This analysis corroborates well with SEM images defining when nanofiber formation occurs. Fibers were not observed until hydrogels were dried with a near-critical pressure of ~1000 psi, but still did not show full nanofiber morphology until the pressure reached above the critical point of CO$_2$.
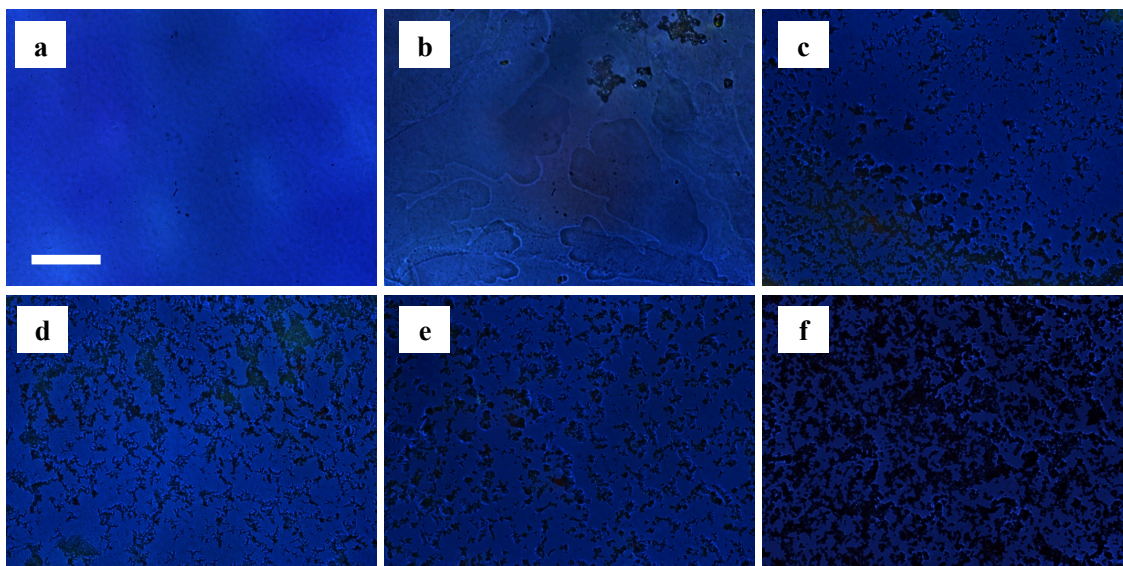
Figure 34. Congo Red analysis of silk fibroin gels dried at near-critical CO_2 pressures. Congo Red birefringence assay was used to examine silk material structural changes. Samples were stained with Congo Red and examined under polarized light microscopy. When the polarizers are crossed at a 90 degree angle to each other, any bright spots are a result of birefringence. (a-f) Congo red images of silk fibroin gels dried at different pressures for (a) silk solution, (b) silk hydrogel, (c) silk gel dried at 200 psi, (d) silk gel dried at 500 psi, (e) silk gel dried at 750 psi, and (f) silk gel dried at 1000 psi. Scale bar is 160 μm.

Additionally, silk gels dried using pressures above the critical point of CO_2 (1071 psi) were also tested and examined with Congo Red staining. Samples dried above the critical point of CO_2 (**Figure 35**) show significant green birefringence compared to samples dried at lower pressures. The presence of a blue background when observing samples is evidence for stress and/or strain in the optical system that would ordinarily have a black background. Furthermore, the formation of nanofibers (from SEM analysis) occurs at the same pressures as the appearance of green birefringence and these results corroborate with samples dried above the critical point of CO_2 suggest that a change in morphology produces a change in crystal structure.
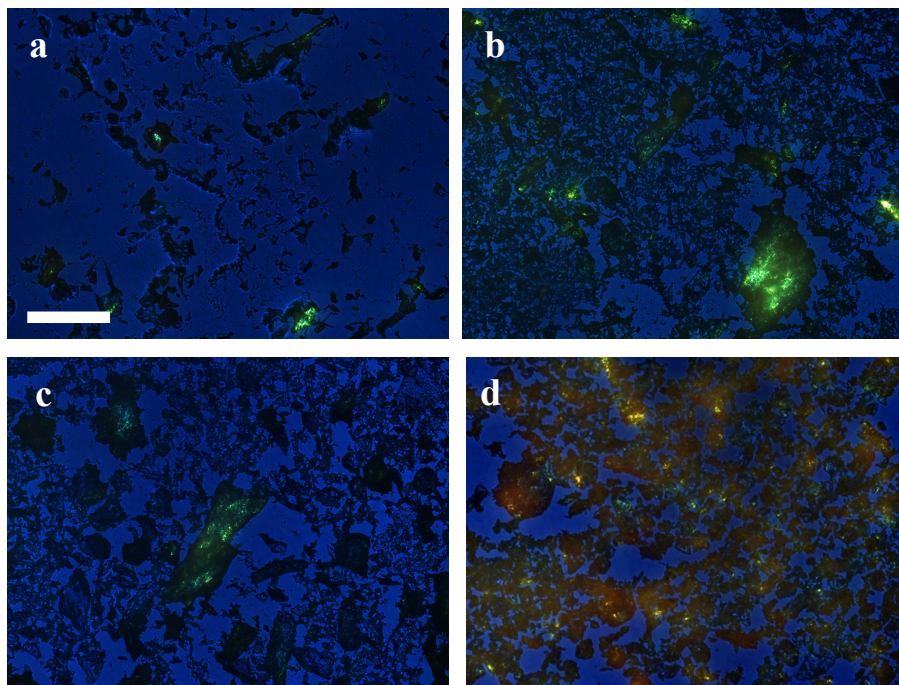
Figure 35. Congo Red analysis of silk fibroin aerogels dried above critical CO_2 pressure. Congo Red birefringence assay was developed to examine fibril structure. Samples were stained with Congo Red and examined under polarized light microscopy. When the polarizers are crossed at a 90 degree angle to each other, any bright spots are a result of birefringence. (a-d) Congo red images of silk fibroin gels dried at pressures above the critical point of CO2 for (a) 1200 psi, (b) 1400 psi, (c) 1600 psi, and (d) 1800 psi. Scale bar is 160 μm.

X-ray diffraction analysis

Figure 36 shows the X-ray diffraction pattern of silk fibroin at initial hydrogel conditions before drying and after $SCCO_2$ drying at 1800 psi. The diffraction patterns are significant of the arrangement of silk molecules (and the atoms within those molecules) associated with an ordered lattice structure. As shown in the previous sections, drying at different pressures causes a change in silk morphology, crystal structure, and silk beta-

sheet fraction. Drying at different pressure is believed to induce more ordered structures (as corroborated by the increase in beta-sheet content) associated with changes in molecular spacing observed from changes in X-ray diffraction patterns. The change in diffraction pattern is significant and the associated peaks represent a change in lattice spacing related with CO_2 drying. **Figure 36a**, a sample dried with a pressure of 0 psi does not show a sharp band significant of highly ordered lattice spacing, particularly compared to the sharp band at 4.2 Å and 3.8 Å observed in **Figure 36b,** a $SCCO_2$ dried sample at 1800 psi.
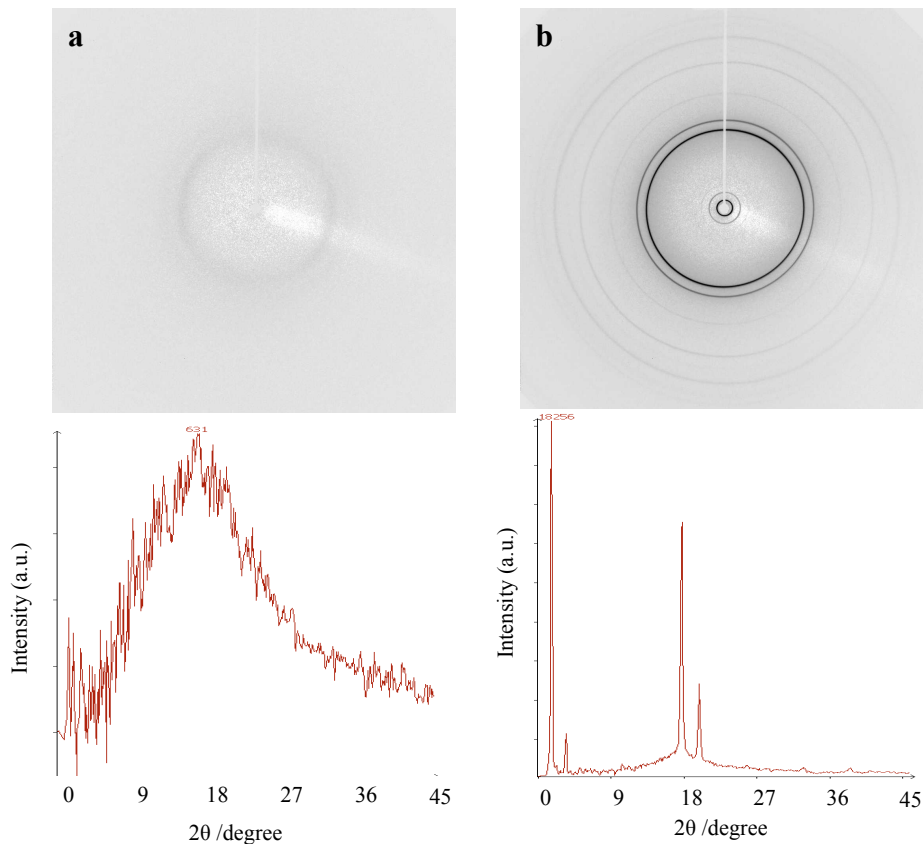
Figure 36. X-ray scattering of silk materials. Images of 2D X-ray scattering patterns and intensity vs. angle plots of silk gels. The patterns correlate to a) a silk hydrogel and b) a silk aerogel dried with supercritical CO_2 at 1800 psi.

As was previously shown from the Congo Red analysis and the morphology analysis, there are changes associated with silk drying at different pressures correlated with X-ray diffraction patterns. **Figure 37a** and **b** shows silk hydrogels dried at 200 psi and 500 psi, with diffuse bands with molecular spacing between 4.2-4.5 Å. However, when fibers begin to form, as was observed after 1000 psi by SEM images, two distinct bands appear at 3.8 Å and 4.2 Å. These bands remain constant and increase in sharpness for samples dried at 1800 psi. The data correlates well with SEM analysis and Congo Red staining suggesting changes in molecular orientation of silk gels dried with CO_2.
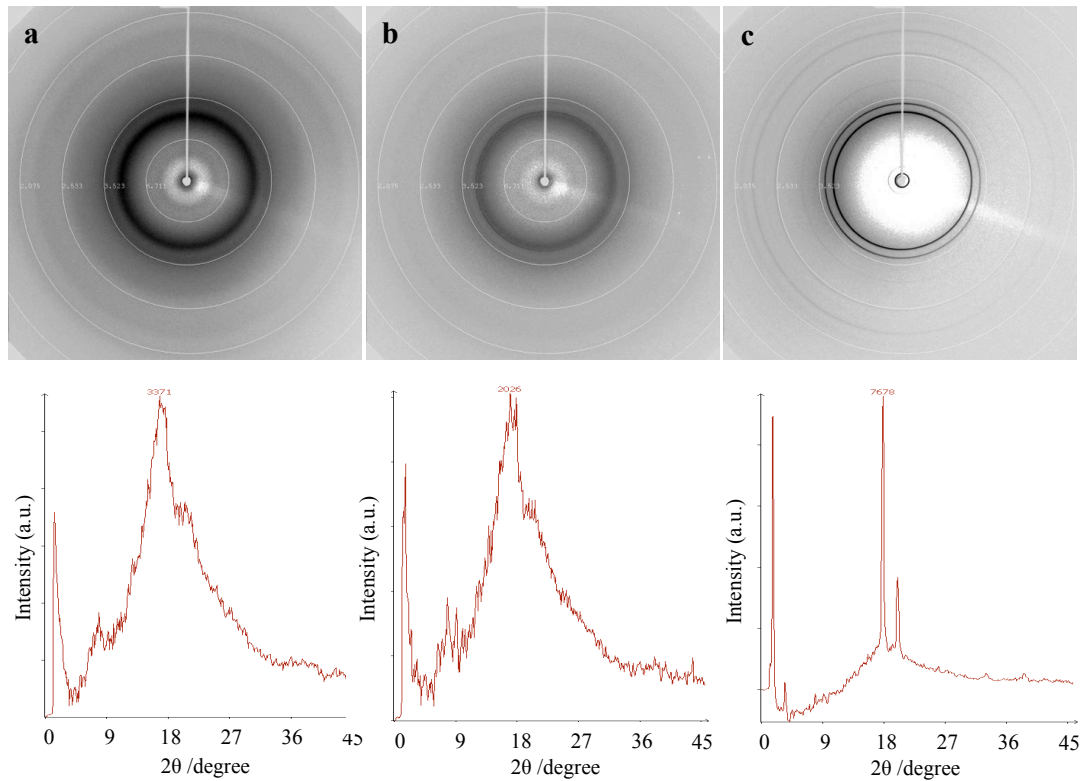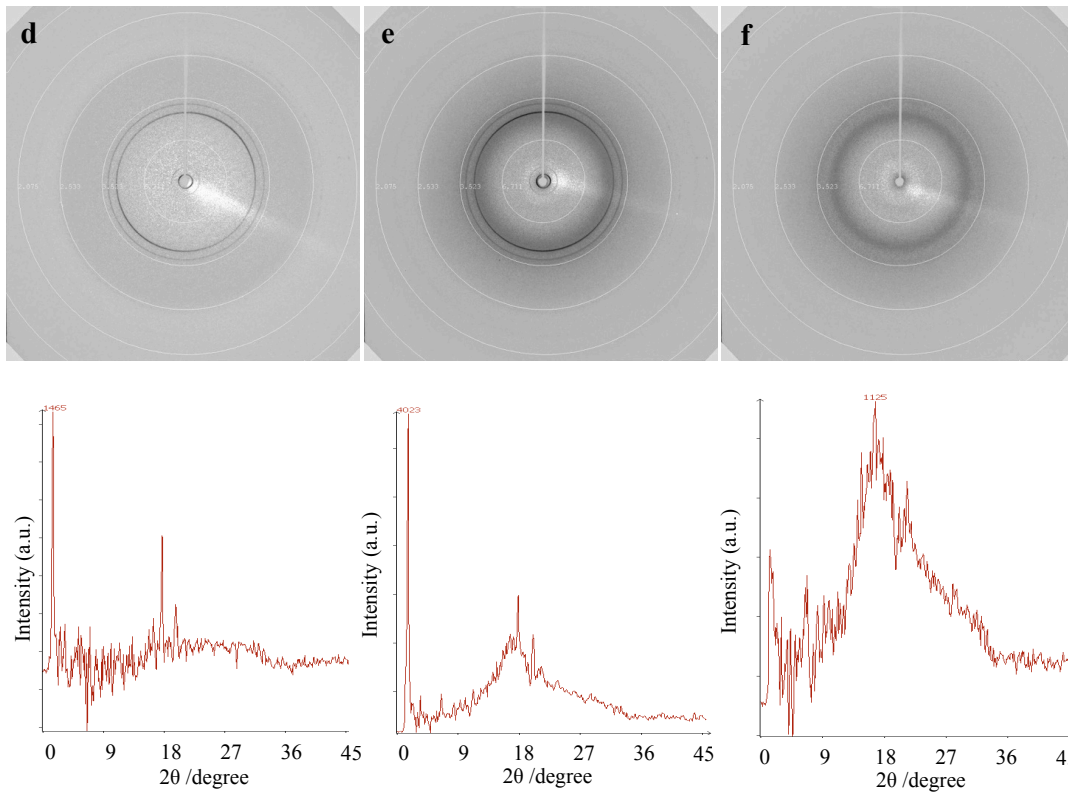
Figure 37. X-ray scattering of silk gels dried at different pressures. Images of 2D X-ray scattering patterns of silk gels dried with CO_2. The patterns correlate to a CO_2 dried silk gel dried at 200 psi, b) at 500 psi, c) at 1000 psi, d) at 1200 psi, e) at 1400 psi, and f) dried at 1600 psi.

Changes in the crystal structure of silk fibroin have shown to provide changes to its mechanical properties.[108] Additionally, it is believed changes to silk crystal structure also change the hydrophilic regions forming semi-crystalline domains. These domains can help form areas that immobilize bioactive molecules and improve their stability by minimizing water content and reducing chain mobility preventing transitions to native states.[104,105]

Furthermore, a control study to determine if EDTA was causing the changes to the crystal structure was examined. Hydrogel samples were prepared without conditioning in EDTA which might assist with the observed green/yellow birefringence and X-ray

diffraction patterns. However, when samples were analyzed by Congo Red staining and X-ray diffraction at 1800 psi, both analysis showed the same green birefringence and diffraction pattern observed as the hydrogels conditioned with EDTA (**Figure 38**).
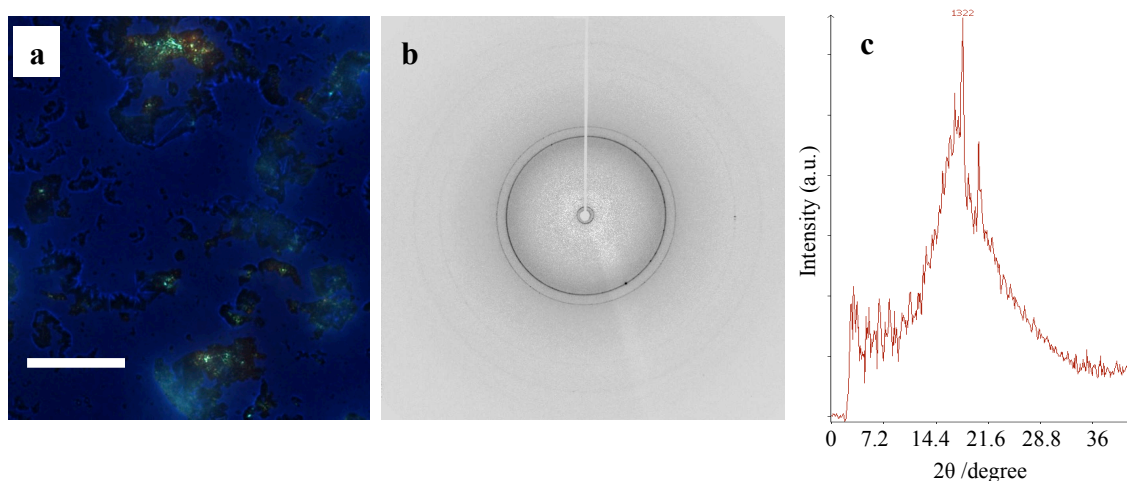
Figure 38. Silk fibroin aerogels not conditioned in EDTA. a) Silk aerogel dried at 1800 psi stained with Congo Red imaged by polarized light microscopy. Scale bar is 160 μm. b) X-ray diffraction pattern of a silk aerogel dried at 1800 psi without conditioning in EDTA. c) Intensity vs. angle plot. Diffraction pattern rings and intensity plots are found at same positions compared to the silk conditioned in EDTA.

Physical characterization

Highly porous materials present advantages over bulk materials in terms of diffusion efficiency and surface area, and thus have utility as catalyst supports or electrodes for electrochemical devices.[5] The structure and morphology ultimately determine the texture and density of the material, which can be changed by processing or removing predesigned sacrificial frameworks.[108] The bulk densities of the associated silk aerogels are shown in **Figure 39a** as a function of starting silk concentration. Aerogel bulk densities range from 23 kg/m^3 to 40 kg/m^3 and are higher compared to their initial hydrogel densities. The increase in bulk density of the aerogel compared to the hydrogel

occurs during hydrogel synthesis and the contraction of the aerogels during supercritical drying. During supercritical drying, shrinkage is attributed to a physical shift to more favorable equilibrium states resulting in a reduction of the overall volume as silk proteins experience high pressure.[101] This results in an average contraction of ~10% from the initial hydrated state and is also observed in other aerogel materials.

The transmission of aerogels as a function of the initial starting concentrations was examined to determine any changes after supercritical drying. Optical transparency in the visible range is necessary to render silk aerogels appropriate for use with optical sources while maintaining structural integrity. **Figure 39b** shows silk aerogel transmission as a function of initial silk concentration over the visible wavelengths. The highest observed transmission is 70% at wavelengths greater than 650 nm while the intensity value at 600 nm show a negative linear relationship associated with initial silk concentration from 60% transmission to 3% transmission. The decrease in transmission can be attributed to the number of interconnections within each gel and the size and spacing of the generated pores. The lower transmission is also observed during hydrogel formation from the uniform scattering of visible light.

Compressive tests were carried out to evaluate the influence of silk fibroin concentration on the mechanical properties of the aerogels. All samples showed a densification behavior distinctive of plastic materials, where low compressive stress generates high material deformation. The typical plastic behavior of the silk aerogels was also depicted as the aerogels were compressed increasing their stiffness as the material experienced higher degrees of deformation (**Figure 39c**). By controlling the initial silk fibroin concentration it was possible to regulate the compressive modulus of the aerogels

from 95 kPa to 250 kPa, which corresponds to the stiffness of many tissues found in the human body. **Figure 39d** illustrates representative stress stress-strain curves at a single crosshead speed for increased silk fibroin concentrations. Additionally, the added crystallinity of the protein after supercritical drying, which has been previously reported to control silk degradation along with the high porosity and size of the nanofibers can be used to impact cell differentiation and overall cell behavior.
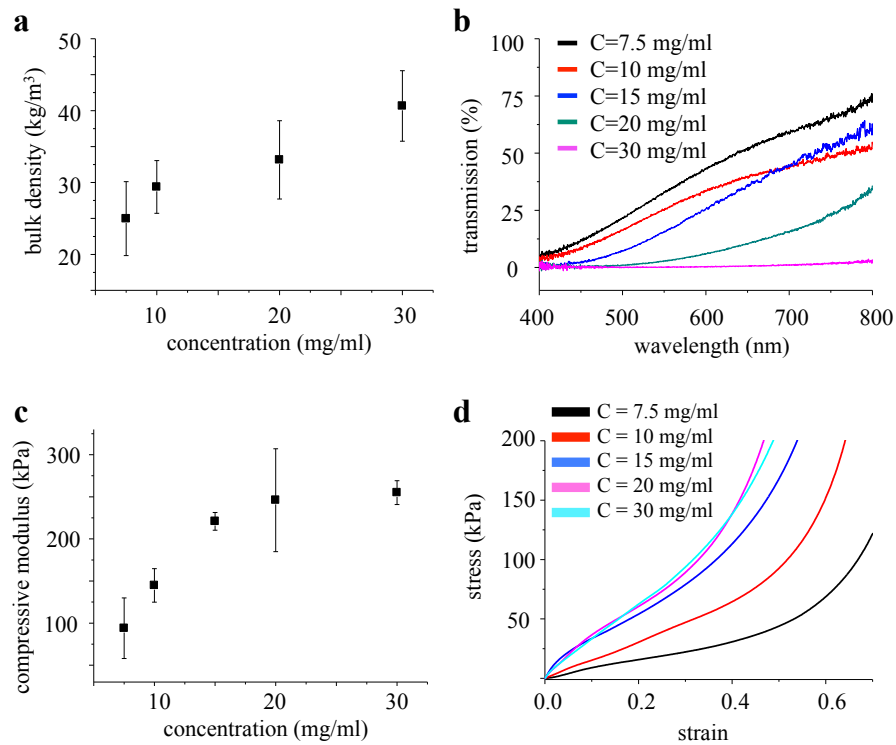
Figure 39. Physical properties of silk aerogels at different silk concentrations. a) Bulk density of silk aerogels measured with different initial silk concentrations. b) Transmission measurements of silk fibroin aerogels with different initial silk concentrations. c) Compressive modulus of silk fibroin aerogels with different initial silk concentrations. d) Stress strain curve of silk aerogels.

Cytotoxicity

As a preliminary evaluation of cytotoxicity, human dermal fibroblasts were cultured up to 10 days on the surface of the silk fibroin aerogel and imaged using confocal laser scanning microscopy. Fibroblasts were stained at days 1, 3, 7, and 10 with calcein-AM fluorescein and EtBr-1 deoxyribonucleic acid binding (Live/Dead® assay) (**Figure 40**). Fibroblasts were viable up to 10 days (green) and compared to silica aerogels as a control. In addition, SEM analysis of the seeded aerogels showed cell coverage up to day 10. Combined with the mechanical and porosity of silk aerogels, further studies can be examined to use this material as a tissue engineered material.
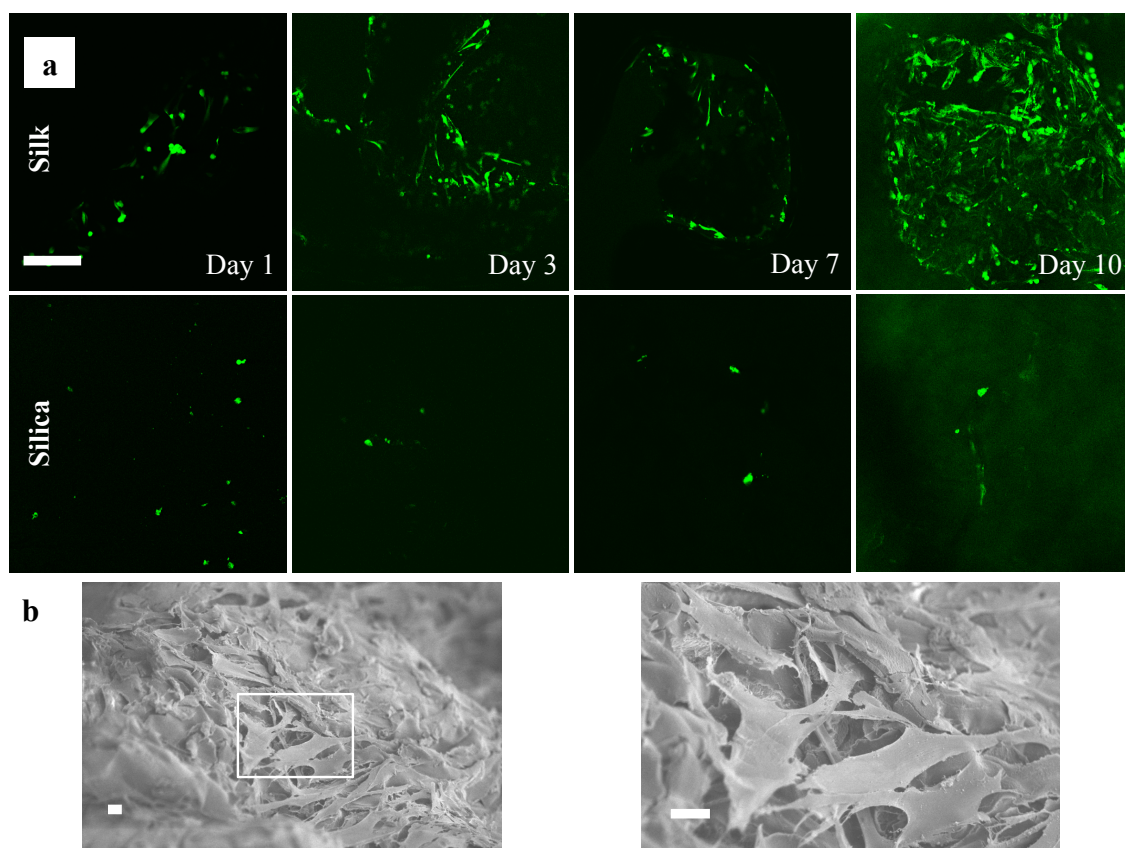
Figure 40. Biological characterization of silk fibroin aerogel. Human fibroblasts were culture on transparent silk fibroin aerogels. Silica aerogels were used as a control. a)

Confocal microscopy of live/dead assay on fibroblasts cultured on the surface of silk fibroin and silica aerogels at day 1, day 3, day 7, and day 10. Cells were viable and proliferated during the culture time considered. Scale bar is 375 μm. b) SEM micrographs cellular gels at day 10 were collected to investigate cell morphology and production of extracellular matrix. The enlarged micrograph shows close up of extracellular matric deposition. Scale bar is 20 μm.

Enzyme stabilization at different temperatures

Aerogels are among the most versatile materials available for technical applications including gas sensing and catalyst supports, and incorporating biologically active enzymes with aerogels can be imperative to make functional materials with various dopants.[5] Recent studies with silk fibroin suggest the large hydrophobic domains interspersed with small hydrophilic regions form semi-crystalline domains creating nanostructured pockets to immobilize bioactive molecules and improve their stability by minimizing water content and reducing chain mobility preventing unfavorable states.[104,105] As a preliminary evaluation regarding the stabilization of active biological compounds in silk fibroin aerogels, horseradish peroxidase (HRP) was mixed with silk fibroin solution prior to hydrogel and aerogel formation. Microplate reads were taken of aerogel samples at days 7, 14, and 21 after the reduction of 3,3′,5,5′-tetramethylbenzidine (TMB) liquid solution which changes from colorless to a bluish-green color in the presence of HRP (**Figure 41**). Silk fibroin aerogel samples and HRP liquid samples were stored at 4°C, 25°C, and 60°C to monitor the effectiveness of the silk aerogel stabilization. At day 14, there is a visible color change in TMB as shown by the images after 10 minutes (**Figure 41**) at 4°C and 25°C compared to the 60 °C sample, which relates to the measured HRP activity. In addition, due to the liquid nature of the samples, collapse of the structure was apparent (**Figure 41a inset**). However, SEM analysis of the

aerogel sample after wetting shows the structure and partial porosity remain making theses samples conducive as liquid sensors and active filtration systems for possible biological samples.
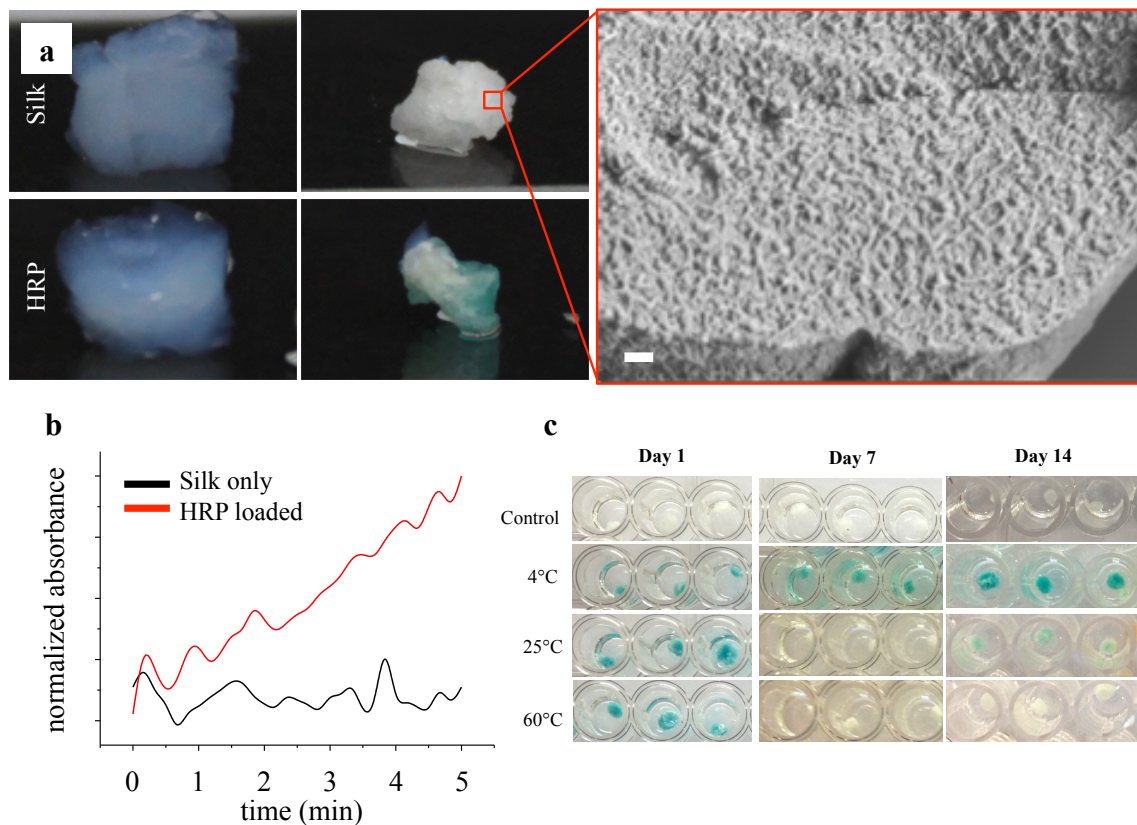
Figure 41. Biological entrapment of enzymes in silk fibroin aerogels. Enzymatic stability of horseradish peroxidase (HRP) in silk fibroin aerogels. a) Images of silk fibroin aerogels with and without HRP in the presence of TMB. In the presence of HRP, TMB follows a reaction changing from a transparent liquid to a blue-green liquid. SEM image of critically point dried aerogels after exposure to a liquid solvent preventing total collapse of the pore structure. Scale bar is 200 nm. b) TMB reaction product absorbance measured at 370 nm for silk and HRP loaded silk fibroin aerogels. c) Images of HRP loaded silk fibroin aerogels stored at different temperatures in the TMB solution at day 1, day 7, day 14, and day 21 and different storage temperatures.

Enzyme stability at different pressures

Protein stability and function are based upon ordered folding structure to minimize free energy, while also organizing into a maximized functional three-dimensional form.[189] While stabilizers are used to maintain protein function, silk has been shown to be used as a stabilizing matrix to reduce chain mobility preventing transitions.[104,105] Therefore, the more structured the order of a stabilizing matrix, the greater the entrapment stability. Altering the beta-sheet content associated with pressure induced crystal lattice changes could improve encapsulation of therapeutic compounds in silk matrices compared to previous results. As a preliminary study, HRP was stabilized in a silk matrix, similar to before, but dried at different pressures in the near-critical point and supercritical regions to determine the effect of crystal structure induced stability. Since it is hypothesized silk molecules form nanoscale pockets to reduce chain mobility of enzymes leading to unfavorable states, the higher the order would produce more ordered "nanopockets". The more ordered nanostructures would improve the stability of entrapped enzymes allowing longer efficacy times. **Figure 42** shows images of silk aerogels dried at different pressure catalyze TMB at increasingly longer storage time. The blue/green color is significant of TMB reduction, which is present at initial conditions. However, samples stored for longer time periods, samples dried at lower pressures, associated with lower ordered crystal structures, have reduced activity to catalyze TMB. These data suggest the higher ordered structures associated with CO_2 drying along with the ability to produce high surface area materials provide a significant advantage compared to other processing methods.
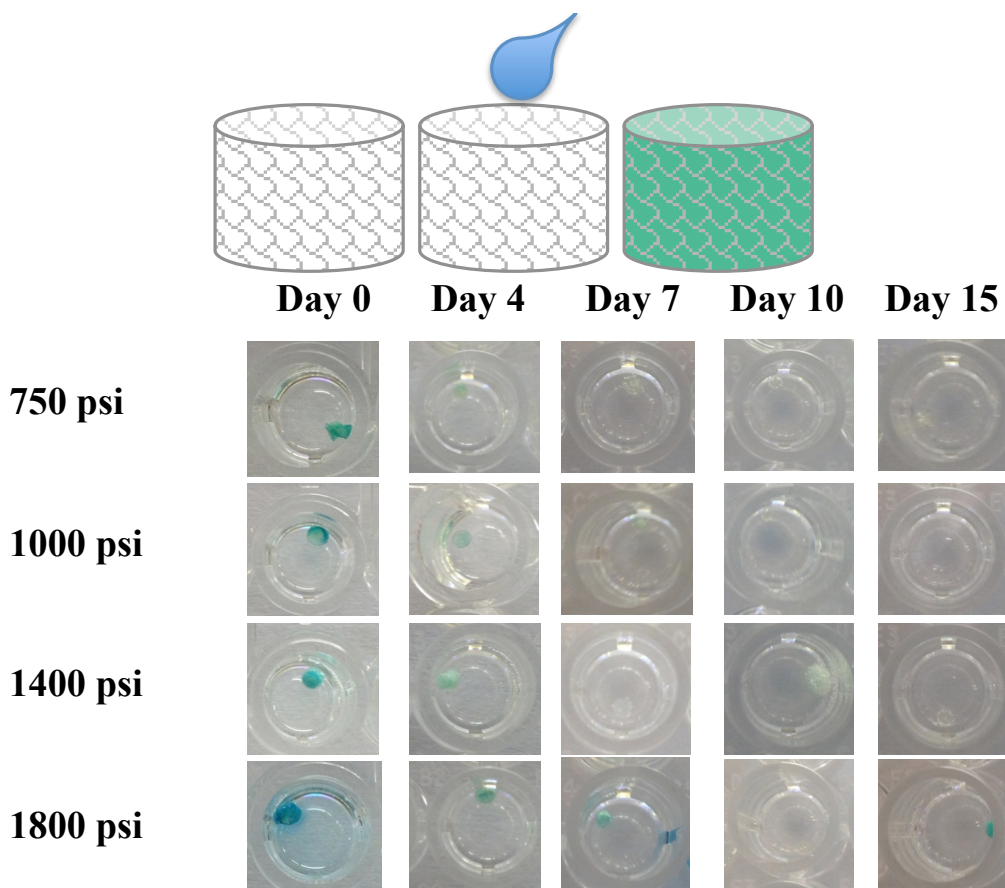
Figure 42. Silk gel HRP stability at different drying pressures. Silk gels were prepared with HRP and dried with CO_2 at pressures 750 psi, 1000 psi, 1400 psi, and 1800 psi. The stability of HRP was measured by the colorimetric assay of TMB at different storage times.

Oxygen sensing

Due to their high porosity, silk aerogels are ideal for gas sensing because gas molecules can contact more often with the higher surface area of the skeletal structure. Aerogel sensors are used for multiple detection purposes including monitoring gas-phase species to determine air quality, assessing pH, or measuring ion concentration in water samples.[7] As a possible gas sensing device, silk fibroin aerogels were loaded with platinum(II) meso-tetrakis(pentafluorophenyl)porphyrin (PtTFPP) to evaluate them as a fluorescent sensor based on the high surface area (**Figure 43a**). Optical oxygen sensing

relies upon collisional quenching of molecular oxygen with a fluorophore[9] causing a non-radiative relaxation reducing the emission intensity. A combination of oxygen saturation and storage conditions at 25 °C and 60 °C were used to examine the stability regarding the effect of temperature on the porphyrin molecule. Repeatability of the sensors at oxygen concentrations of 0% and 20% were examined that showed no appreciable difference after repeated and cyclic use (**Figure 43b**). To confirm the sensitivity of the samples, the derivative of the fluorescence intensity was compared during each cycle of 0% oxygen saturation and 20% oxygen saturation showing there was no change in fluorescence rate (**Figure 43c**). However, after prolonged exposure to storage temperature conditions at 25 °C and 60 °C (21 days), there was an observed difference in fluorescent intensity of the aerogels samples (**Figure 44a and 44b**). Silk aerogels kept at a higher temperature showed a larger change in fluorescence at 0% oxygen saturation and 20% oxygen saturation up to 21 days compared to aerogels stored at 25 °C (**Figure 44c**). The decrease in change in fluorescence observed at higher temperatures is hypothesized to occur due to damage of the skeletal structure from changes of the ambient humidity content at 25 °C compared to the drier 60 °C condition. To prevent damage due to liquid or gaseous water, these aerogels have the capability to become hydrophobic with a contact angle of ~110° by conditioning the samples in a saturated HMDS gas environment for 24 hours.
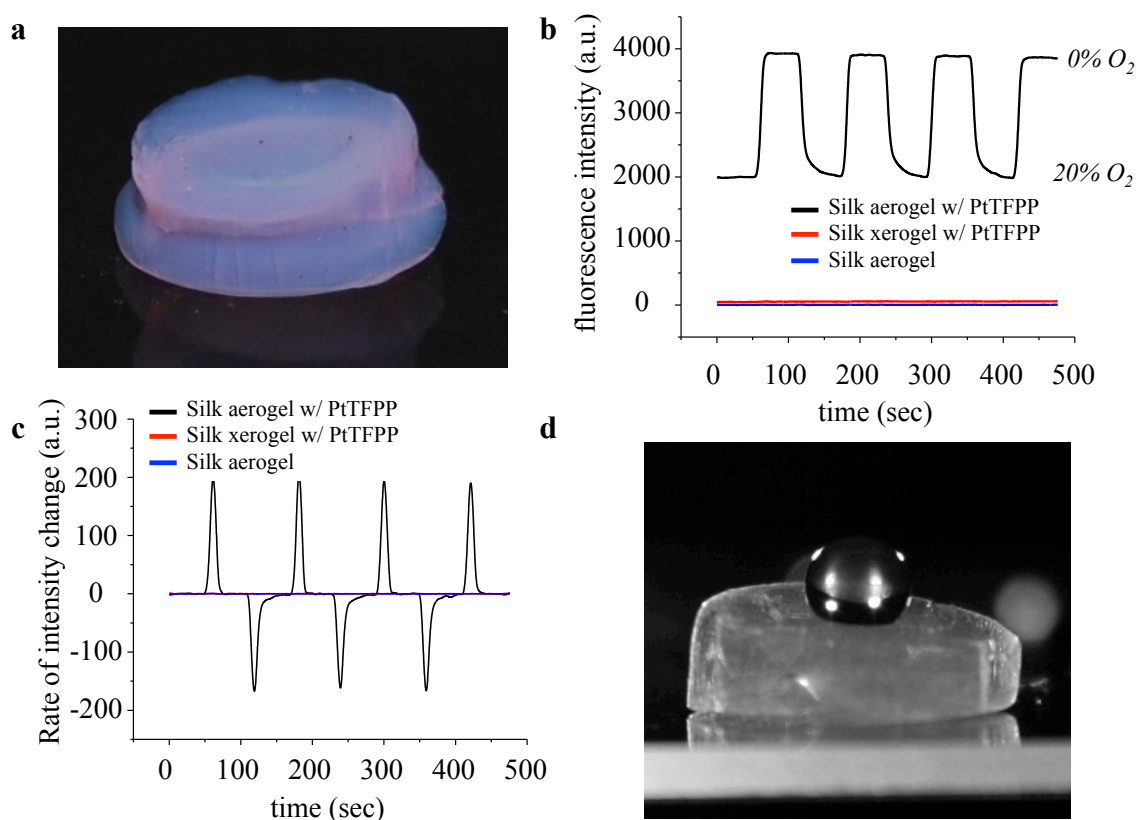
Figure 43. Silk aerogels as gas sensing materials. PtTFPP loaded silk aerogel for oxygen sensing applications. a) An image of a silk fibroin aerogel loaded with PtTFPP. b) Fluorescent measurements of silk fibroin aerogels loaded with PtTFPP, silk xerogels loaded with PtTFPP, and silk aerogels without PtTFPP. Nitrogen gas was cycled every minute during measuring starting at ambient oxygen levels of 20% and finishing at 0% during flushing the chamber with nitrogen. c) Derivative of fluorescent intensity vs. time to show the response of oxygen sensitivity during oxygen measurements. d) Image of hydrophobic silk aerogel with a contact angle of ~110°.
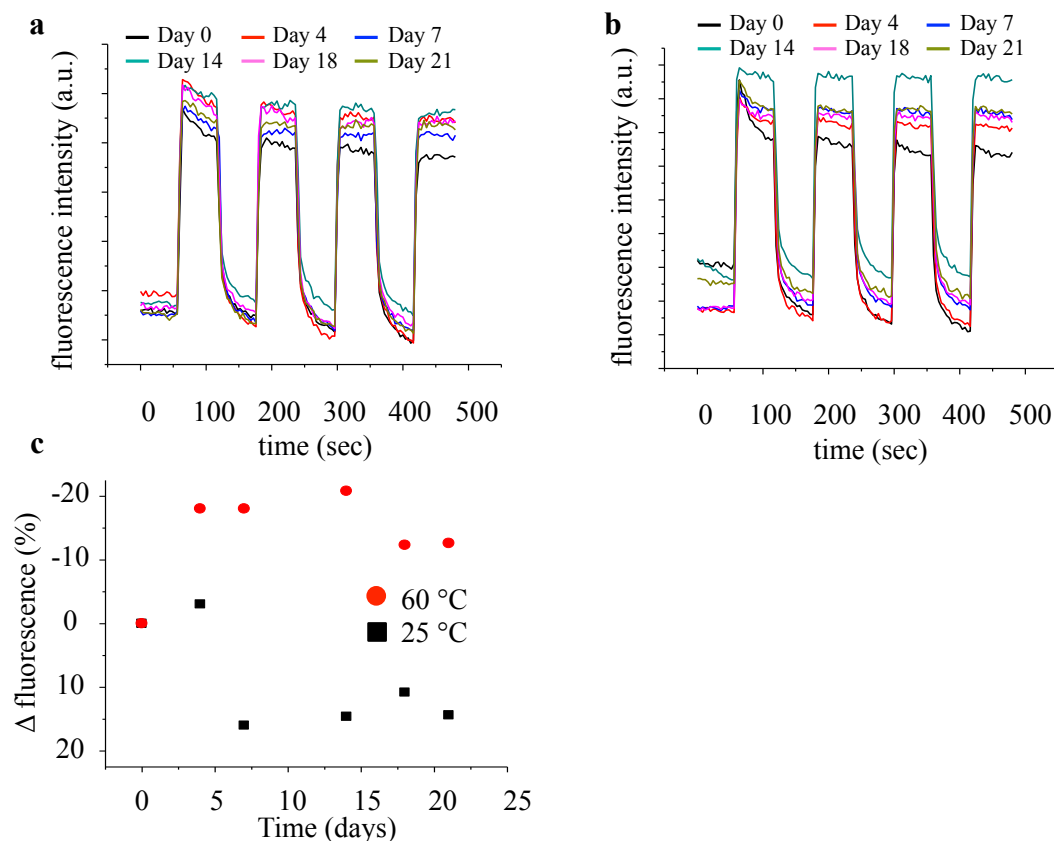
Figure 44. Stability of PtTFPP in silk fibroin aerogels at different temperatures. The effects of temperature on silk fibroin aerogels as measured by fluorescence of representative samples at (a) 25 °C and (b) 60 °C. (c) Difference in 0% oxygen saturation fluorescence and 20% oxygen saturation fluorescence of individual silk fibroin aerogels compared to the initial saturation difference. The negative value associated with 60 °C aerogel samples signifies there is an increase in the difference between 0% oxygen saturation fluorescence and 20% oxygen saturation fluorescence compared to aerogel samples stored at 25 °C.

Silk fibroin aerogels after supercritical N2O drying

Carbon dioxide (CO_2) is one of the most commonly used supercritical fluids because it is relatively inert, nontoxic, non-flammable, inexpensive, and is a cleaner substitute compared to volatile organic solvents and non-aqueous waste streams.[16,203,204] The supercritical conditions associated with CO_2 are also favorable as the temperature and pressure are relatively low compared to other materials (T_c = 31°C, P_c = 1071 psi).

Supercritical CO_2 (SCCO$_2$) is ideal for products that are sensitive to high temperature and meant for human consumption.[13,16] Therefore, food and pharmaceutical industries are very active in developing and implementing SCCO$_2$ based processes.[15,17,18,74,197,205] SCCO$_2$ has recently been explored in polymer processing because the density of SCCO$_2$ can be fine tuned by varying pressure which changes the properties of the SCCO$_2$. Furthermore, the SCCO$_2$ is easily removed by depressurization.[204] However, many polymers become swollen and plasticized in the presence of SCCO$_2$, and SCCO$_2$ plays a major role to change polymer morphology from unnecessary chemical reactions caused by its acidic conditions.[18,196,197] The morphological changes are a result of CO_2 molecules interacting with basic carbonyl groups of the polymer reducing chain-chain interactions and increasing polymer segment mobility.[18] Therefore, to prevent changes in polymers during supercritical drying, another supercritical fluid is required.

As mentioned above, transformations occur by changes in pressure during near-critical and SCCO$_2$ drying creating silk fibroin aerogels for drug delivery.[99,100] The pressures associated with these transformations form nanofiber structures. However, since silk responds to change in pH, it is expected these structures are formed from a combination of high pressure and the acidity of CO_2. Therefore, finding an alternative material is necessary to examine the supercritical fluid conditions altering silk fibroin.

A supercritical fluid with low temperature and pressure are important because high critical temperatures can degrade the silk and high critical pressures can result in excessive compression.[74,206] As mentioned above, CO_2 is the most common critical fluid for bioprocessing because it is nontoxic, non-flammable, and inexpensive along with a relatively low critical point. Nitrous oxide (N$_2$O) is a fluid with similar characteristics to

CO_2 with relatively low critical point parameters (T_c = 37°C, P_c = 1050 psi), a permanent dipole moment, low chemical reactivity, and low acidity.[206] The importance of working with a non-acidic supercritical fluid will prevent the interacts with silk's carbonyl groups reducing chain-chain interactions causing polymer molecular movement. Therefore, processing silk fibroin gels under similar with supercritical N_2O should result in different morphology and crystal structure compared to CO_2.

To evaluate the effects of supercritical fluids instead of pressure on the silk hydrogels, samples were exposed to supercritical N_2O compared to $SCCO_2$.[207] Samples were maintained at 1200 psi, 50 °C, and effluent flow rate of 4 kg/hr. **Table 4** highlights the physical properties of supercritical CO_2 and N_2O. The physical properties of the two molecules are very similar, particularly regarding the critical temperature (T_C) and critical pressure (P_C), especially when compared to other materials used as supercritical fluids. Similar to CO_2, N_2O has relatively low T_C and P_C allowing N_2O to be used in similar chambers as supercritical CO_2 drying. Additionally, some of the major advantages of N_2O as a supercritical fluid are its low chemical reactivity and the lack of acidity. Therefore, any changes that are caused by silk interacting with CO_2 will not occur with supercritical N_2O.

Physical properties of carbon dioxide and nitrous oxide		
Material Property	Carbon dioxide (CO_2)	Nitrous Oxide (N_2O)
Molecular weight	44.01 g/mol	44.01 g/mol
Critical temperature	30.98 °C	36.27 °C
Critical pressure	1071 psi	1050 psi

Critical point density	467.6 kg/m^3	452.01 kg/m^3
Latent heat of fusion	204.93 kJ/kg	148.57 kJ/kg
Latent heat of vaporization	574 kJ/kg	374.3 kJ/kg
Solubility in water	1.716 vol/vol	1.14 vol/vol

Table 4. Physical properties of supercritical carbon dioxide and nitrous oxide.

It was hypothesized the nanostructure changes to the silk hydrogels would be different when using supercritical N_2O drying compared to $SCCO_2$ because of their chemical differences. As observed in **Figure 45**, there is a distinct change from hydrogel to aerogel, and the aerogel formed after supercritical N_2O drying looks physically different compared to similar silk gels dried with $SCCO_2$. Unlike an elastic and hygroscopic material, silk aerogels dried with N_2O are more brittle, fragile, and less hygroscopic. The image in **Figure 45b** shows a more lustrous appearance compared to CO_2 dried silk aerogels and are more opaque compared to their previous counter parts. Additionally, the morphology of the aerogels dried with supercritical N_2O is also different compared to $SCCO_2$ dried silk aerogels. The nanofibers on the surface have diameters ~50 nm and show a more pearl-like structure compared to the continuous nanofibers associated with $SCCO_2$ drying. This pearl-like morphological is significant because the hydrogels used were formed by mixing silk solution with acetone which has been shown to make nanoparticles ~50 nm in diameter that attach together in a pearl-like structure when forming the hydrogel. The morphology after $SCCO_2$ of silk gels reveals the fusion of silk nanoparticles, which has been observed several times. The pearl-like structure that is observed after supercritical N_2O drying signifies that the nanoparticles do not fuse together like they do with $SCCO_2$ suggesting a different mechanism. Therefore,

the chemical differences between N_2O and CO_2 changes the morphology of silk fibroin during supercritical drying. This showed that not only is pressure responsible to change structure in silk fibroin, but the supercritical fluid also has affects the morphology and should be considered when working with protein biopolymers.
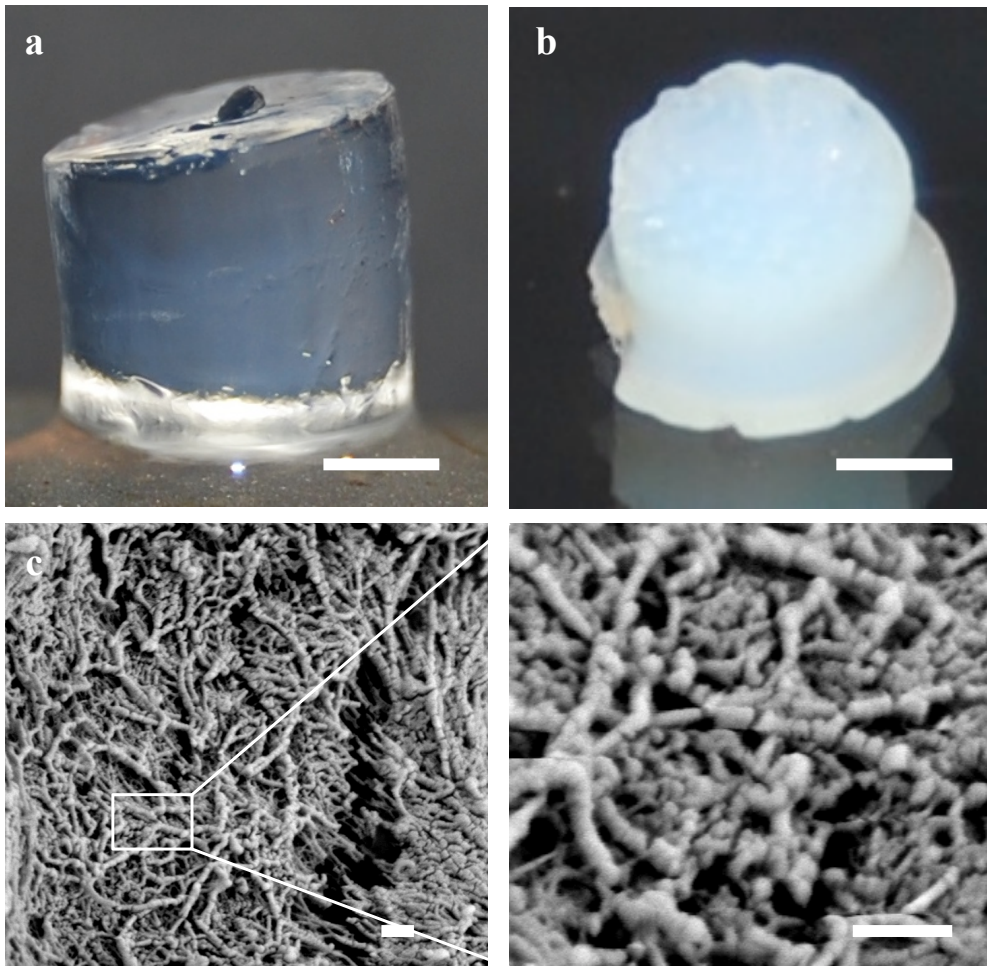
Figure 45. Morphology after supercritical N_2O drying on silk gels. a) An image of a silk fibroin hydrogel. b) Image of a silk fibroin aerogel produced after supercritical N_2O drying of a silk fibroin hydrogel. Scale bar is 2 mm. c) SEM image of supercritical nitrous oxide dried silk gel. Scale bar is 200 nm.

The morphology changes should also lead to changes in crystal structure as mentioned above. ATR-FTIR was conducted on supercritical N_2O silk fibroin samples to determine the amount of beta-sheets after supercritical drying (**Figure 46**). Determining the amount of beta-sheet content has been shown as a successful method to determine the amount of crystallinity in a sample. Using the method provided by Hu, silk fibroin hydrogels dried in N_2O had a beta-sheet content as high $47.5 \pm 1.6\%$.[208]
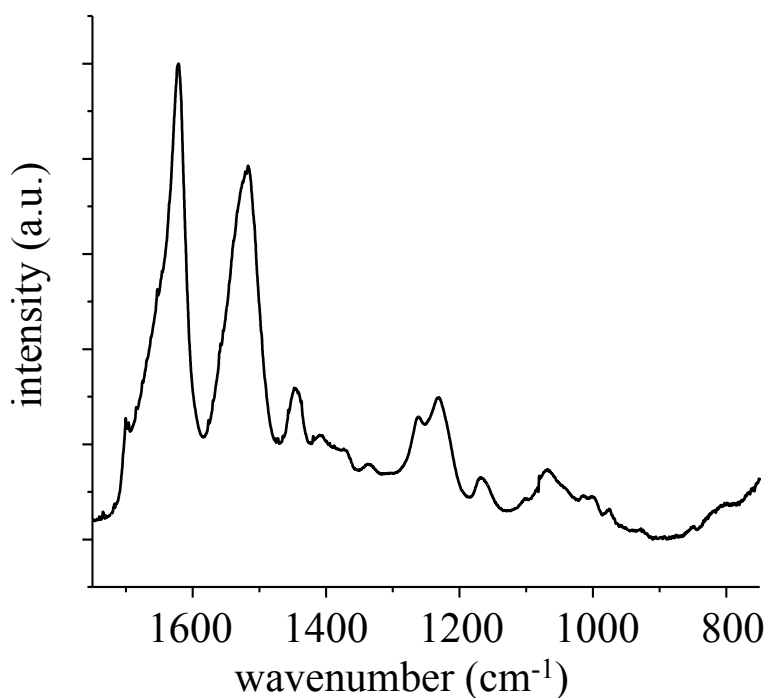
Figure 46. ATR-FTIR spectrum of silk fibroin after supercritical N_2O drying.

Additionally, to examine other crystal structures, samples were examined using X-ray diffraction. **Figure 47** shows the diffraction pattern with a weak diffuse spacing from 4.17-4.77 Å compared to samples dried with $SCCO_2$ which shows two distinct bands (**Figure 36**). The diffraction pattern shows there is change from hydrogel to aerogel when

dried with supercritical N_2O and there is also a change when compared to $SCCO_2$. These results corroborate observed morphology of the aerogels and the hypothesis that nanofiber formation associated with nanostructure relates to pressure and the supercritical fluid.
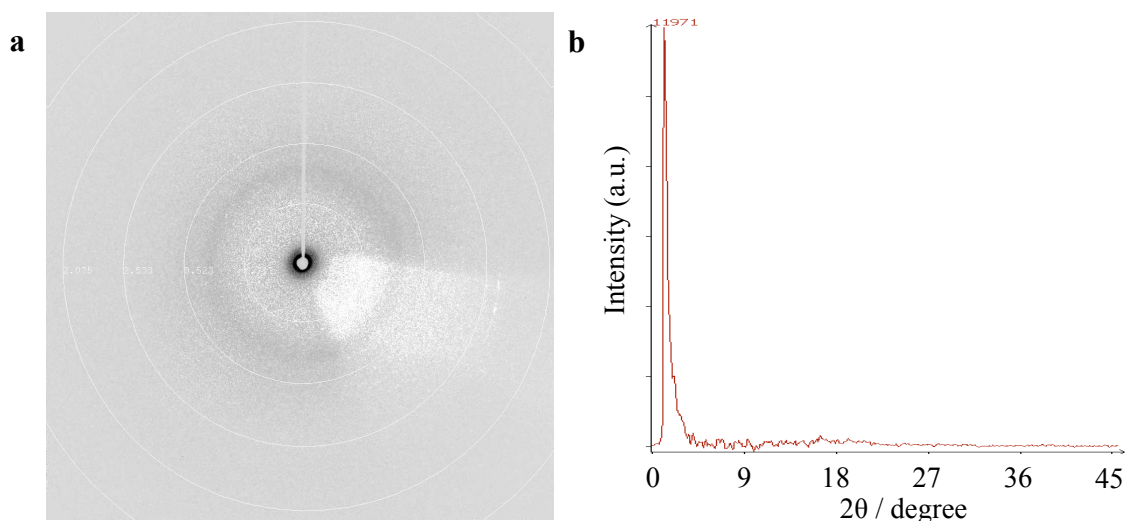
Figure 47. a) X-ray diffraction pattern of supercritical N_2O dried silk fibroin gel and b) intensity vs. angle graph.

Conclusions

In conclusion, we have successful developed and characterized a silk fibroin nanofiber material after near-critical point and $SCCO_2$ drying. The samples were analyzed morphologically by SEM, and structurally by ATR-FTIR spectra, Congo Red staining, and X-ray diffraction. Nanofibers 10-20 nm in diameter and pores ranging from 50 to hundreds of nanometers were formed during synthesis generating aerogels with bulk densities as low as 25 kg/m³ and transmission in the visible spectrum up to 60%. The mechanical properties can be varied due to changes in initial silk concentration and offer an elastic modulus within the biological range to culture human fibroblasts up to 10

days.

Changes in nanostructure are capable by changing the drying pressure relating to near-critical and supercritical pressures. Samples showed a calculate increase in beta-sheet content at higher pressures, and, pressure drying showed observed changes in crystal lattice spacing between 4.2-4.5 Å shifted to smaller lattice spacing (3.8 Å) at higher pressure drying that can be correlated with fiber formation. The most significant structural changes occurred in the supercritical region and agree with previously stated results. Immobilization of HRP maintained enzymatic activity up to 21 days at varying temperature conditions. Additionally drying at different pressures associated with improved lattice spacing offers a new practice to stabilize enzymes in silk fibroin based on crystal structure. The crystal domains helped form microenvironments that immobilized HRP and improved its stability by minimizing contact with water and reducing chain mobility, which can damage enzyme activity. The nanofiber network associated with these silk aerogels also provides high surface area to be used as gas sensor materials for biomedical nanostructured applications in a protein based material.

Furthermore, this chapter examines the morphology and crystal structure after supercritical N_2O on silk fibroin gels. As previously shown, nanofiber formation is not only affected by pressure changes associated with CO_2 but also from its acidity.[99,209] Supercritical N_2O does not fuse the nanoparticles as effectively as $SCCO_2$ while the aerogels becomes more brittle. Differences in the morphology between N_2O and CO_2 were also observed in the crystal structure using FTIR and X-ray diffraction. Applying supercritical N_2O drying to silk hydrogels provides an understanding of silk nanofiber

formation, and the data agrees with the proposed hypothesis evaluated morphologically

and structurally to confirm the differences between $SCCO_2$ and supercritical N_2O.

General conclusions

This dissertation has presented and examined nanostructured materials in silk fibroin after different processing conditions for biomedical applications. We united applied research in material science, nanomaterials, and protein conformational transitions in an interdisciplinary way that created new material forms for eco-friendly and biodegradable applications made from silk fibroin. We elucidated the mechanism of formation, optimized and characterized physical, chemical, and biological properties, and identified applications for tissue engineering, catalytic platforms, and degradable sensors. Silk nanoparticles, silk hydrogels, and silk aerogels were developed, characterized, tested, and used for specific applications. Each nanostructure was determined by different fluid conditions and offered forms of the silk fibroin. The results directly translate into new platforms where optical clarity, low density, high surface area, and biodegradability are required.

Specifically, this dissertation has shown the generation of silk micron and submicron spheres using a microfluidic co-flow capillary device. Under different concentrations of silk, different silk fibroin molecular weights, different concentrations of the continuous fluid (PVA), and different flow rate ratios, the diameter and dispersion of the generated silk spheres were controlled. Additionally, the silk formulation was mixed with a model drug before sphere formation to be used for drug delivery applications.

Regarding silk hydrogels, this dissertation formed highly transparent, nanostructured hydrogels formed by nanoprecipitation using reconstituted silk fibroin with organic solvents acetone, ethanol, methanol, and isopropanol. Different concentrations of silk

fibroin changed the transparency of the hydrogels by changing the diameter of the formed

nanoparticles during solvent mixing. The mechanical properties of the hydrogels were

tuned by conditioning in a dilute solution of EDTA which increased the compressive

modulus up to 10 times compared to its as formed state. Additionally, silk hydrogels

showed good attachment of human dermal fibroblasts and human corneal epithelial cells

to the surface for use as tissue scaffolds. Metabolic activity of human corneal epithelial

cells grown on the silk hydrogels was significantly higher after 7 days of growth

compared to human corneal epithelial cells grown on collagen hydrogel controls.

Transmission of the hydrogels was unaltered compared to collagen samples after cell

attachment making them possible as lens replacements.

This dissertation also showed the synthesis of silk nanofiber formation after near-

critical point and supercritical CO_2 drying. A theoretical model of nanofiber formation

from nanoparticles was empirically determined by evaluating at different drying

pressures. The mechanism was also evaluated using a different supercritical fluid, nitrous

oxide. Silk fibroin molecular movement associated with pressure induced morphology

changes were also corroborated by an increase in the beta-sheet fraction. Stabilization of

biological enzymes increased at higher drying pressure drying believed to be due to the

increase in crystal structure that minimize contact with water, reducing chain mobility.

Human fibroblasts showed good attachment up to 10 days on acetone formed aerogels

and sensing platform using an oxygen sensing molecule was also shown in this work.

In conclusion, the formation of nanostructures in silk fibroin is possible under

different processing conditions to produce relevant biomedical applications in drug

delivery, tissue engineering, and sensors. The concentration ratio between the fluid

environment and silk fibroin has a significant impact on silk's final form changing the morphology and crystal structure. This study plays a noteworthy role in polymer processing (in this case silk fibroin), but can also be considered when using other biopolymers. Therefore, this work could be applied to other relevant fibrous proteins to induce nanostructure formation by changing the fluid environment altering a material's morphology and crystal structure for biomedical applications.

Future directions

Micron- and submicron spheres

Future studies regarding silk micron- and submicron spheres include examining the generated spheres *in vivo*. A basic *in vivo* study would evidence to better understand the cytotoxicity of the silk microspheres to determine if they are cleared on the first pass after injection. This study would determine location of the micron and submicron sphere after injection. A majority of the microfluidic work focused on tuning sphere size and dispersion based on concentration, viscosity, and flow rate. However, potential physiological studies are necessary to achieve the full potential of these spheres. The application provided showed evidence for potential uses for drug delivery, but further studies would offer more information about the necessary biology.

The work shown in this dissertation focused on a model peptide for drug delivery, but many other additives can be attempted. Materials such as small molecules, magnetic nanoparticles, gold nanoparticles for controlled heating, or laser and fluorescent dyes have been added to silk solution to make films suggesting the silk particles are also possible with these additives. Loading these additive could also be examined that would

allow them to be used for targeted delivery where silk is the matrix carrier. As on example, studies using water-soluble ferrofluids was attempted to make magnetic microspheres for targeted delivery. The synthesized magnetic silk spheres responded to a magnetic field and were made with low dispersion (**Figure 48**). Furthermore, due to the benign all-aqueous process of silk, multiple additives can be combined with the solution before sphere (or film formation) adding multiplicity to such forms. As an example, silk spheres could be mixed with magnetic particles and a cancer drug to conduct targeted drug delivery to tumors.
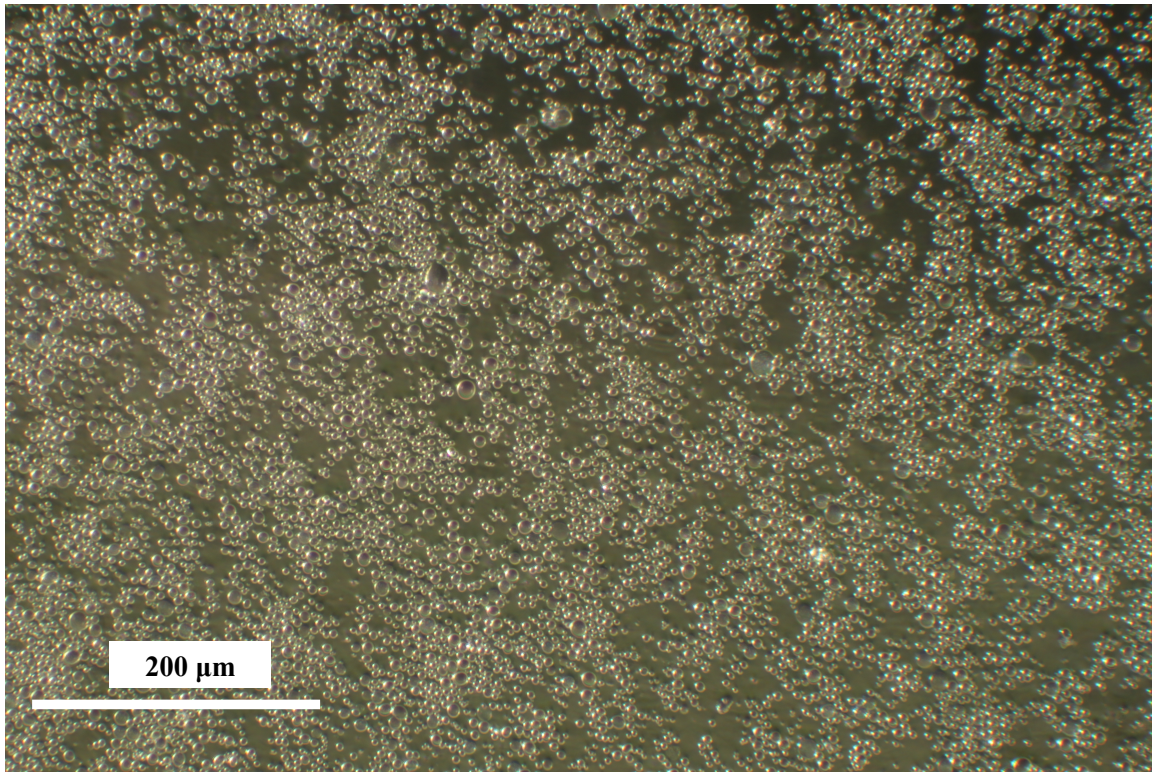
Figure 48. Magnetic microspheres. Microscope image of silk microspheres mixed with ferrofluid before synthesis. Silk fibroin spheres have a diameter ~2 μm in diameter and respond to a magnetic field. Further investigation show the spheres have a pole and orient themselves in the direction of the magnetic field lines.

Also, recent research in delivering small interfering RNA (siRNA) has transformed the study of gene regulation for disease treatment because interfering RNA can knockdown genes by targeting complementary mRNA due to their high specific sequence.[210] Interfering RNA have the potential to silence genes and treat diseases such as cancers, viral infections, and hereditary disorders.[210] However, even though the possibilities of siRNA seem limitless, it still requires an effective delivery matrix to target cells. Cationic lipids and polymers have been explored over the past decade that act as carriers to escort siRNA into the cytosol through an endocytotic pathway.[210] Degradable polymer vesicles are possible as delivery vehicles that can maintain the function of the siRNA and readily release it in response to intracellular environments. As a future application, degradable silk submicron spheres can be used as polymer vesicles to delivery siRNA to assist in gene silencing.

Finally, silk nanospheres of controlled diameter could be used to fabricate photonic devices such as silk opals. There is significant research where microspheres are used with optical sensing. Current research has produced silk inverse opals by making a nanostructured mold of PMMA spheres before casting the solution on top and removing the PMMA spheres by wet etching leaving a free standing inverse opal silk film.[113] There are optical properties associated with inverse opals, but there are also different optical properties with regular opals. Additionally, the spheres created using a flow-focusing device would ideally have more tunable diameters so fabrication of silk opals with different lattice spacing to create colors throughout the entire visible spectrum would be possible. However, the yield and volume of silk nanospheres produced, particularly at the submicron level, were not significant. A higher multiplexed system with several nozzles

is required to produce the amount of silk nanospheres with consistent size and diameter. Additionally, due to the benign loading of the silk solution with interactive materials, silk opals could be used to enhance the optical properties of additives as observed in silk inverse opals.[113]

Silk hydrogels

Future work regarding nanostructured hydrogels can be used where transparency, low compressive modulus, and slow remodeling are desired. Most tissues are highly scattering and absorbing and do not efficiently let light enter the tissue, therefore, a transparent hydrogel could be used to image tissues at significant depths. The dermal fibroblast study showed that cells could be imaged at a depth of 1 mm, however, imaging cells is not the only possibility for this hydrogel. The transparent hydrogel could be used as a window to image other materials (i.e. proteins, lipids, etc.) embedded within the hydrogel or outside the hydrogel. Examples could include illuminating and observing fluorescently labeled spheres entrapped within or on the surface of these hydrogels.

Future work on the hydrogels should also include *in vivo* performance studies. The nano features of these hydrogels are attractive for growing cell as shown during the *in vitro* work. Cell growth was well observed which is believed to be associated with the elastic modulus of the hydrogels and the nanotopology. The *in vitro* studies regarding human dermal fibroblasts showed significant cell growth and alignment while also depositing an extracellular matrix. It has been shown the degradation of silk fibroin is much slower compared to polymers derived from mammals such as collagen and elastin. Therefore, using the silk hydrogels *in vivo* will allow it to remodel slower compared to

other scaffold, which may benefit studies for soft tissue repair, or where as soft elastic modulus is necessary.

Silk aerogels

Silk aerogels should be researched in areas where high surface area and porosity are necessary in a protein matrix. Over the past several decades, aerogels made from different materials have been examined as discussed in Chapter 1, and this dissertation attempts to offer different possible applications using silk aerogels. The ability of silk fibroin aerogels to stabilize biological compounds along with its high surface area makes this form ideal for chemical and biological sensing and mitigation.

Adding other materials such as gold nanoparticles and carbon nanotubes (CNT) can also be added to silk aerogels as shown in **Figure 49**. Silk is the material of choice for such situations because adding these materials is easier due to its benign water-based processing compared to other materials. Adding non-biological materials to silk aerogels can provide new applications in sensing and devices because the additives are more exposed more
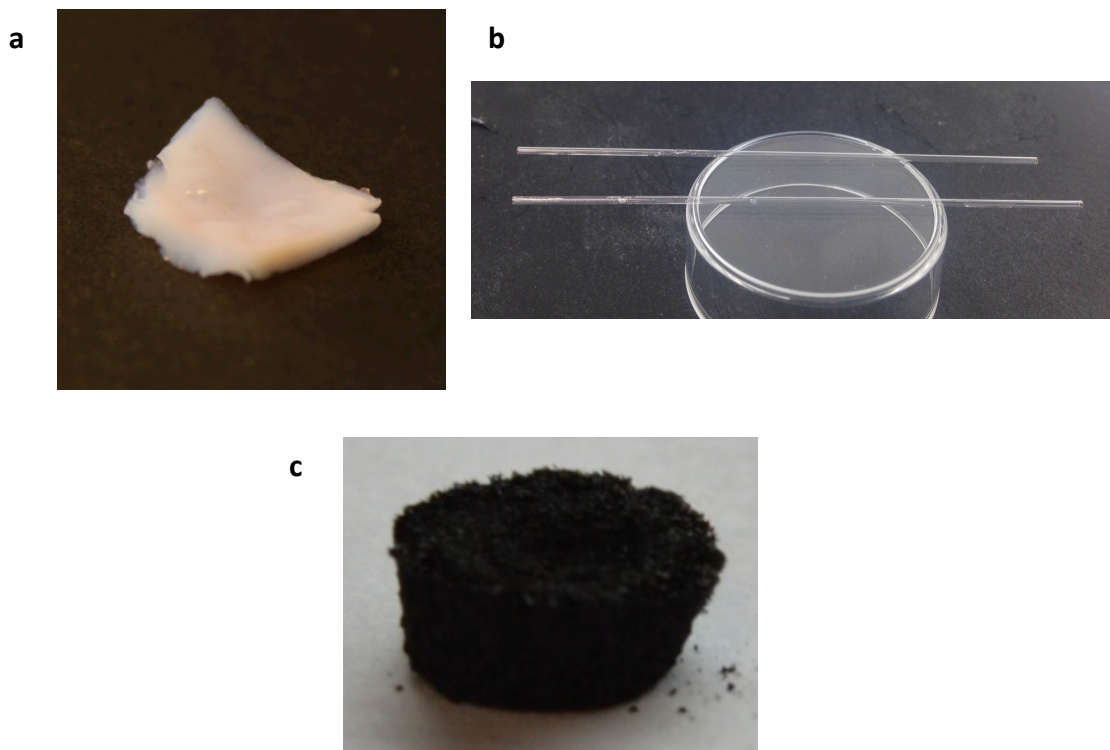
Figure 49. Non-biological additives to silk fibroin aerogels. a) Silk aerogels loaded with gold nanoparticles, b) gold nanoparticles loaded silk aerogels in capillary tubes, c) carbon nanotubes.

Laser machining features into silk fibroin aerogels can also be attempted and may be a potentially better material compared to polyurethane aerogels because silk requires lower laser powers to machine lines.[211] Laser machining the aerogels can occur on the surface to make defined features and shapes or inside the aerogels due to its high transmission. This work has been attempted and is shown in **Figure 50**.
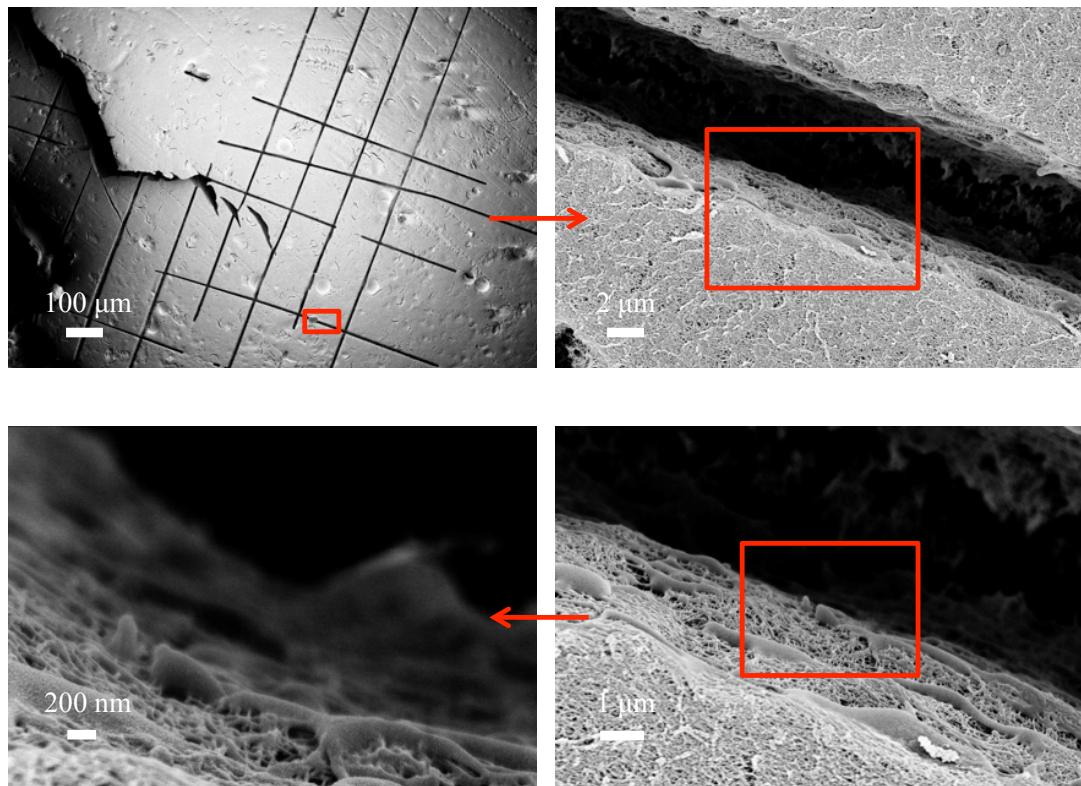
Figure 50. Laser machined silk aerogels. Different magnifications showing the scale of laser machining. At the highest magnification it shows how the silk material is melted on the edge of the surface instead of forming a clean cut.

More research can also be conducted on these silk fibroin aerogels as tissue scaffolds where high surface area and porosity are required. Mineralization onto the silk aerogels has been attempted to enhance cell attachment for tissue scaffolds. Additional chemistries such as RGD modification and other decoration methods can be applied before or after formation. The silk aerogel showed attachment of cells without any modification. Therefore, enhancing the silk surface for cell attachment and growth benefit silk aerogels as tissue scaffolds.

Aligned the nanofibers within the silk aerogels can also examined. Aligning the fibers could occur during supercritical drying, which induces stress on the silk in all directions. If the stress is controlled more in one direction compared to another, then the fibers will align in that diretion. If the molds of silk hydrogels have dimensions significantly longer in one direction compared to other directions it may be possible to form regions of highly aligned nanofibers during supercritical drying. Applying stress to the aerogels during drying or hydrogel formation was shown to be an effective method to align fibers. In an early silk aerogel study, aligned fibers were found on the edge of a bubble (**Figure 51**) which was believed to generate a stress gradient. Furthermore, if the hydrogels are initially loaded with conducting materials such as carbon nanotubes (as shown above), aligned fibers can be used to improve the conductivity of silk fibroin materials because it is currently believed alignment of the fibers is one of the limiting factors for successful conductivity.

1 µm

200 nm
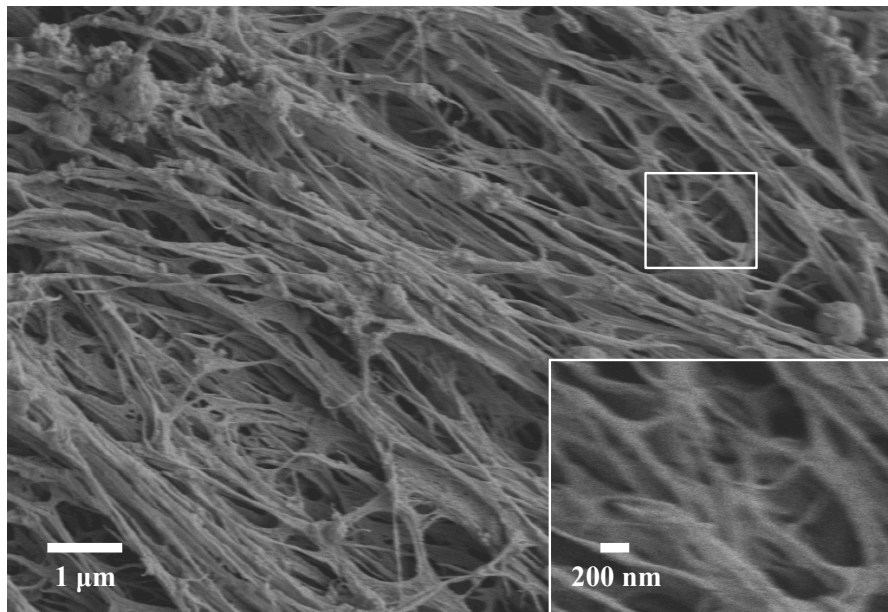
Figure 51. Alignment of fibers in HFIP/silk aerogels. Alignment is believed to have occurred from stresses formed during hydrogel formation on a bubble edge.

Furthermore, silk aerogels can be used as an absorbing material (**Figure 52**). In a preliminary study, the aerogels were able to absorb up to 20 times their mass of a liquid solution. **Table 5** shows the initial mass of the silk aerogel (m_i), the final mass of the silk aerogel after the addition of liquid (m_f), and the absorbance ratio. Silk aerogels are not as highly absorbing as graphene aerogels but are highly absorbing for both polar and nonpolar liquids.[212] The ability to absorb both polar and nonpolar liquids makes this silk aerogel unique. Since silk fibroin has hydrophilic and hydrophobic domains it interacts with both polar and nonpolar solvents. Furthermore, since silk is a biodegradable material it is beneficial for applications such as oil spills and less eco-friendly clean up compared to other more brittle and potentially hazardous aerogels that may absorb more liquid but may cause more damage to the environment.
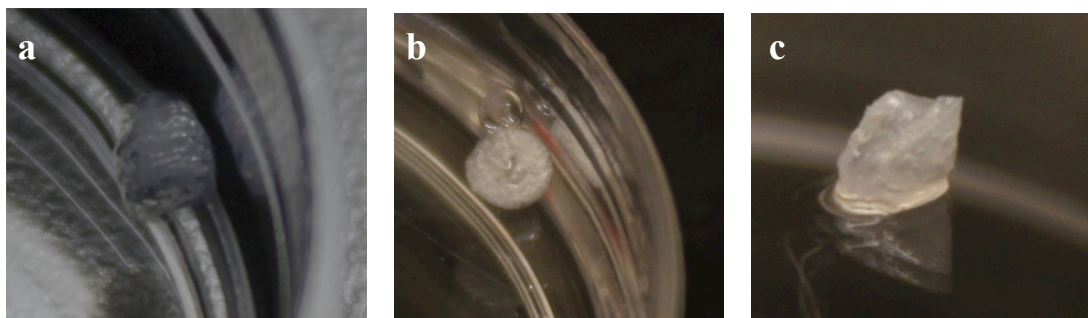
Figure 52. Silk aerogels absorbing ability. Images of silk aerogels absorbing a) isopropyl alcohol, b) ethanol, and c) water.

Liquid	m_i *(mg)*	m_f *(mg)*	m_f/m_i
IPA	3.1	46.2	14.9
Methanol	2.6	41.8	16.1
H_2O	3.5	75.5	21.6
Lighter fluid	3.1	71.7	23.1

Table 5. Initial, final, and ratio of silk aerogel masses after absorbing with different fluids.

Additionally, there are several different possible mechanisms to form a silk hydrogel followed by supercritical drying. Since processing silk fibroin differently creates different hydrogels, these hydrogels will form different aerogels with unique physical properties (**Appendix A**). In the aerogel handbook, one chapter discusses how silica made with different precursors and different methods produces an aerogel with different physical properties. Preliminary results show that different silk fibroin hydrogels critically point dried can provide different aerogels with different properties.

Aerogel covers applications such as energy storage, super insulation, platforms for chemical sensing, high energy physics research, implantable devices, tissue substrates, drug delivery systems, pharmaceutical applications, and space exploration.[7] Keeping this knowledge in mind and combining it with the different processing conditions silk could be just as an effective material compared to other substances.

General future works and considerations

This work on nanostructured silk fibroin forms could be relevant using other fibrous proteins regarding fluid environment changes, with a particular focus on supercritical drying. Part of this dissertation has shown the changes in morphology of silk fibroin at different pressures using near critical and $SCCO_2$. Supercritical drying is designed to prevent structural changes associated with ambient temperature drying. However, this dissertation reveals changes in morphology occurring in a fibrous protein. Further research should be considered regarding nanostructured changes in other biologically

relevant fibrous proteins that have been prepared by supercritical drying. It is possible these materials also undergo similar changes that can provide them with unknown properties and should be examined by future researchers.

APPENDIX A: SUPERCRITICAL CO$_2$ DRYING OF OTHER SILK GELS

Abstract

Silk fibroin from the *Bombyx mori* caterpillar is a well-known biopolymer that can be processed into several different forms such as fibers, films, and gels from a reconstituted solution. Additionally, silk fibroin can be formed into several different gels depending on the processing condition. Recently, dried silk fibroin gels from hexafluorisopropanol (HFIP) have been investigated as fracture fixation materials to be used as resorbable craniofacial repairs. Silk fibroin gels prepared using HFIP have increased mechanical properties compared to gels prepared in water because it stabilizes the alpha-helical conformation. Here we examine supercritical drying of HFIP silk fibroin gels as highly porous materials for biomedical applications. Low concentration silk fibroin gels made from HFIP and lyophilized silk, cross-linked with ethanol, and dried with supercritical CO$_2$ produce low density, high porosity degradable materials to be used as tissue engineering constructs. Furthermore, other hydrogel preparation methods are possible methods from silk fibroin can be dried with supercritical CO$_2$ producing materials with different physical properties. The physical properties associated with these gels are ideal for high porous tissues and other resorbable material repairs.

Introduction

Advanced drying technology is a method to produce a material with high surface area, low density, and low thermal conductivity.[37] However, a material must start as a gel prepared using a variety of techniques to fabricate the material matrix into nanostructures. Supercritical drying of alcogels is used to maintain the solid skeletal structure by removing the pore fluid with respect to the matrix.[74] Supercritical fluids are used to prevent phase transitions between liquid and gas because they have the same density between liquid and gas preventing the formation of surface tension forces that can damage delicate structures at liquid-gas-solid junctions.[17] This drying process produces materials known as aerogels that are solid materials possessing unique physical properties including large porosity and high mechanical strength.[197]

Silk fibroin, purified from the *Bombyx mori* silk caterpillar, is a well-established material that is possible to form into fibers,[106,109] films,[45,213–215] foams, particles,[154] hydrogels,[101,110] and recently aerogels after supercritical drying with CO_2.[99,100] The production of silk based materials requires a detailed understanding of processing conditions to induce the hierarchical structure responsible for the mechanical properties among protein primary structure and molecular assembly.[216] Silk fibroin molecular folding is a characteristic of the solvent that causes the primary structure to arrange into structures such as random coils, alpha helices, or beta-sheets.[216]

Alcohols denature the native state of proteins and are useful to stabilize protein specific structures in aqueous environments.[217] Since the properties of silk fibroin depend strongly on the preparation conditions, the choice of solvent is important and affects the overall quality of the bulk material.[218] 1,1,1,3,3,3-Hexafluoro-propan-2-ol (HFIP) is one

of the most applicable solvents for the stabilization of secondary structures in proteins, particularly stabilizing the alpha-helical conformation.[217,219] Protein concentration is a significant factor in unfolded protein conformations as it regulates between random coil and alpha-helix.[217] Furthermore, the addition of alcohols stabilizes the helical state and depending on the alcohol concentration results in bounding hydrophobic alcohols to the protein decreasing the polarity around protein chains stabilizing local hydrogen bonds and amphiphilic helical conformations.[217] Silk fibroin exposed to HFIP and alcohols have been used to make gel materials which after convective drying can be used for fracture fixation systems or artificial fibers.[216,220] Dissolving silk with HFIP to make different forms, particularly gel materials before convective drying offers mechanical properties associated with the protein folded structure and maintains the assembled solid structure in the alcogel formation.[220]

Over the past decade, silk fibroin has been formed into hydrogels using several different methods. Hydrogels have been synthesized by sonication, electrogelation, and recently by addition with horseradish peroxidase (HRP).[68,108,221] Each method generates a silk gel with different physical properties. Previous results using $SCCO_2$ drying of silk gels produces nanofibers, and it is hypothesized the nanofibers are a result of silk molecules interacting with $SCCO_2$ at high pressure causing molecular unfolding. To examine these effects, other silk hydrogels were examined to identify and explain the theorized model. Supercritical drying silk fibroin gels to produce nanofibers has not been observed using other drying methods, and it is believed to be a constant with all silk gels and not only silk gels produced using the previously described method.

There is a need for biomaterials that match the physical and mechanical properties of human tissue by mimicking the extracellular space with particular interest for cell infiltration, porosity, and mechanical properties.[42] For tissue engineering applications, silk hydrogels have been used as scaffolds because their mechanical properties, degradability, porosity, and structural can mimic tissues.[108] One of the most common requirements for mechanically improved scaffolds with load bearing properties that match native tissue is pores.[42] Silk's initial strength comes from inter- and intra-molecular interactions between protein molecules that fold into favorable beta-sheets.[109,110] Combing the strength with the biochemical cues of the protein structure help promote cell growth for advanced tissue scaffolds.[109]

Here, we explore porous silk aerogels after supercritical drying gels induced using HFIP, HRP, and sonication. The gels have controllable geometries to improve the mechanical strength and improve the porosity compared to other generated silk scaffolds such as sponges as a major step towards silk based biomaterials. The physical properties of different silk aerogels will be characterized by examining the porosity, density, mechanical properties, and optical transparency. Examining the hydrogel morphology with and without supercritical drying will determine the effect of supercritical CO_2 drying on silk fibroin in these states. Additionally, the crystal structure of each gel will be examined to determine molecular changes after drying. These hydrogels have different characteristics compared to the aerogel mentioned previously. We present a review of the different silk gel formations along with properties and future applications for silk fibroin aerogels.

<u>Experimental</u>

Materials

Silk aerogel synthesis

Silk fibroin solution was prepared as previously described.[108] *B. mori* silkworm cocoons were boiled for 30 minutes in a solution of 0.02 M Na_2CO_3 to remove the sericin glycoprotein. The extracted fibroin was rinsed in deionized water and set to dry for 12 h. The dried fibroin was dissolved in 9.3 M LiBr solution at 60°C for 3 h. The solution was dialyzed against deionized water using a dialysis cassette (Slide-a-Lyzer, Pierce, MWCO 3.5KDa) at room temperature for 2 days until the solution reached a concentration of ~60 mg/ml. The obtained solution was purified using centrifugation.

For HFIP aerogels, the reconstituted silk fibroin was frozen for 2 days and vacuum dried at - 20 °C until complete sublimation and stored in ambient conditions to prevent any rehydration of the lyophilized silk fibroin until used in the processing steps below. The vacuum-dried silk was resolubilized in HFIP (Matrix Scientific, USA) to generate solutions for preparation of aerogels. Before dissolving in HFIP, the vacuum-dried silk was packed into a 30 ml syringe for 4 w/v% silk in HFIP, 0.8 g of vacuum-dried silk was mixed with 20 ml of HFIP. The concentration is critical as solutions with lower concentrations produced aggregated gels. The solubilized HFIP silk solutions were stored at ambient temperatures until used in the molding steps.

Silk aerogel were prepared using plastic dishes and filled with HFIP/silk solution. After the HFIP/silk solution was stable, 200 proof ethanol (Fisher Scientific, USA) was carefully cast on top of the HFIP/silk solution. Mixing between the HFIP/silk solution and ethanol was prevented by slowly adding ethanol on the side of the plastic dish and

allowed to rest on top of the solution. Samples were undisturbed for two days to induce beta-sheet conversion and form a free-standing gel. Additional ethanol rinses were continued to displace the HFIP and create a silk alcogel to prepare samples for supercritical drying.

Silk hydrogels prepared by sonication were prepared as previously described by taking a 10 mg/ml solution of silk fibroin and sonicating at 20% amplitude for 30 seconds and left to gel.[68] Silk hydrogels prepared by HRP crosslinking were prepared as previously described by mixing 10 Units of HRP to 1 ml silk solution and initiated with 10 μl of 165 mM hydrogen peroxide.[221] Both the sonicated and HRP induced hydrogels were dehydrated in a series of ethanol rinses at concentrations of 50%, 70%, 80%, 90%, 95%, 100%, and 100% for 30 minutes to be prepared for supercritical carbon dioxide (SCCO$_2$) drying. The materials were then dried in SCCO$_2$ at 50 °C and 1800 psi maintaining the same temperature and fluid extraction rate before examination and use for further experimentation.

Morphological characterization of the alcogels without SCCO$_2$ drying was obtained by drying the samples in hexamethyldisilazane (HMDS). Samples were exposed to a series of HMDS baths at 70%, 90%, 100%, and 100% for 30 minutes to ensure complete saturation. Samples were then left to dry in a chemical hood for 12 hours to allow complete evaporation and then immediately sputter coated for SEM analysis.

Methods

Measurements

Morphological measurements

SEM images were taken by a Supra55VP FESEM (Zeiss) using the SE2 detector. Samples were sputter coated using platinum/palladium or gold and imaged at 4 kV.

Density/porosity measurements

  Bulk density of the silk aerogels was conducted by weighing the samples and dividing by the sample volume using a standard laboratory bench top scale.

Transmission measurements

Spectra were taken using a vis/near-infrared fiber-optic spectrometer (USB-2000, Ocean Optics). White light was propagated through the fiber to illuminate the sample. The transmitted light was coupled into a fiber tip opposite to the spectrometer. The distance between the illumination source and the collection tip was fixed at 7 mm.

FITR measurements

FTIR analysis of samples was performed in a JASCO FTIR 6200 spectrometer (JASCO, Tokyo, Japan) in attenuated total reflectance (ATR). Hydrogels were let to dry on a glass slide. For each sample, 64 scans were coded with a resolution of 1 cm^{-1}, with a wavenumber range from 4000-600 cm^{-1}. Fourier self-deconvolution (FSD) of the infrared spectra covering the amide I region (1595-1705 cm^{-1}) was performed by Opus 5.0 software. The second derivative was applied to the original spectra in the amide I region with a nine-point Savitsky-Golay smoothing filter. Deconvolution was performed using Lorentzian line shape with a half bandwidth of 25 cm^{-1} and a noise reduction factor of

0.3. Apodization with a Blackman-Harris function was performed automatically at the same time in the software.

Mechanical testing

The compressive properties of samples of 4 mm in diameter were measured using an Instron 3366 testing frame (Instron, Norwood, MA) with a crosshead speed of 2 mm/min, with a 100 N capacity load cell. Samples were conducted in air between force plates until maximum compression was reached. The linear elastic modulus was calculated using a least-squared fitting in the linear region of initial compression up to a 20% strain point.

Four-point bending was conducted on HFIP/silk induced aerogel beams to evaluate the flexural strength of the material. Silk beams were machined to a width of 4 mm, length of 29 mm, and a thickness of 3 mm. Plate geometry was not explored. A four-point bending fixture was machined from stainless steel with brass loading rollers. Brass loading rollers and support rollers were used to allow rolling during testing to avoid frictional forces. The bending fixture was machined to ASTM standard F205-11 with a loading span and center span of 6 mm with support rollers placed directly between the 2 outer holes. The bottom fixture remained stationary while the top fixture was mounted to the Instron test frame and compressed at a rate of 5.00 mm/min until complete compression. A load vs. load point displacement curve was generated to determine bending stiffness, bending structural stiffness and bending strength using the methods described in ASTM standard F2502-11.

Bending stiffness (N/mm) was determined by calculating the slope of the initial linear portion of the line. Bending structural stiffness is the normalized effective stiffness that

takes the test set up configuration into consideration. Bending structural stiffness was

calculated using the equation:

$$EI_e = \frac{(2h + 3a)Kh^2}{12}$$

where:

EI_e = bending structural stiffness (Nmm^2)
K = bending stiffness (N/mm)
a = center span distance (mm)
h = loading span distance (mm)

Bending modulus was determined derived from published methods for four-point

bending from the equation:

$$E_{4p} = \frac{m_{4p}L_0^3}{8wh^3}$$

where:

E_{4p} = four-point bending modulus (MPa)
m_{4p} = four-point bending stiffness (N/mm)
L_0 = length between support rollers (mm)
w = width of plate (mm)
h = height of plate (mm)

X-ray diffraction measurements

Silk materials were prepared as described above. Measurements of the X-ray

diffraction patterns from the silk materials were conducted at room temperatures using an

Oxford Diffraction Xcalibur PX Ultra System (Oxford Diffraction Ltd., Concord, MA).

The CuK$^\alpha$ X-ray beam with wavelength of 1.542 Å was generated at 45 kV/40 mA using

an Enhance Ultra, a sealed tube-based system incorporating confocal multilayer optics.

The X-ray beam was monochromated and the K$^\beta$ component was removed by means of

the double bounce within the confocal optics. The X-ray beam was focused to 0.3 mm x 0.3 mm (full width at half-maximum at detector position). A two-dimensional Onyx CCD detector (Oxford Diffraction Inc., Concord, MA) with pixel size of 121 μm was placed 62 mm from the sample position, covering the scattering range of Bragg spacing. Exposure time was 150 s.

Results

HFIP/silk aerogels

General inspection of HFIP/silk gels after the addition of ethanol showed that at low concentrations HFIP/silk gels are transparent and mechanically robust. Compared to other gelation methods this technique involves cross-linking HFIP/silk solution in ethanol compared to processes involving formation of a film followed by cross-linking with alcohol.[108,220] After dehydration to remove the HFIP and saturate the silk gel in ethanol, the HFIP/silk gel remained transparent (**Figure 53a**). There is a change in transparency compared to the initial gel after supercritical drying as observed in **Figure 53b** but compared to other silk aerogels in previous chapters, the as made aerogel remains partially transparent and is more mechanically robust.
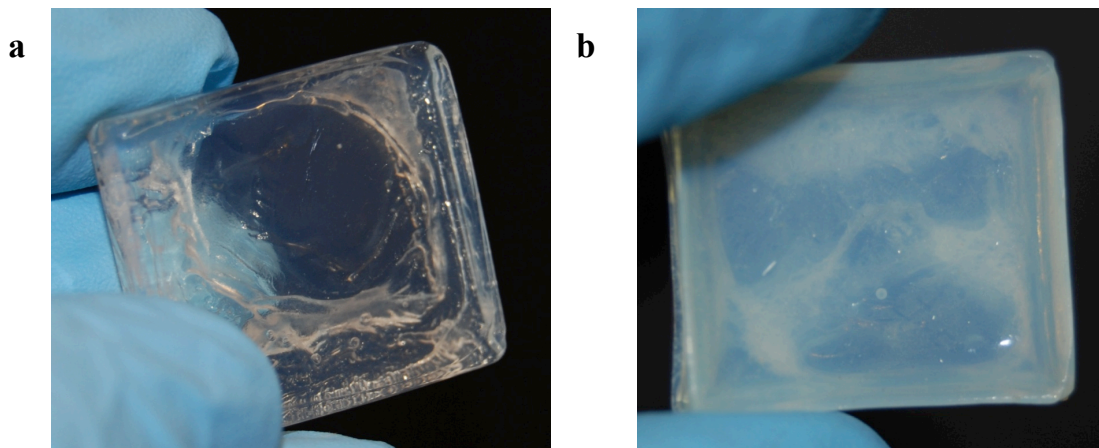
Figure 53. HFIP/silk formed (a) gel and (b) aerogel.

SEM images using HMDS chemical drying and $SCCO_2$ drying show the transition to nanofibers associated with silk aerogels as observed before. Maintaining the features of the silk gel after $SCCO_2$ improves its porosity to be used for further applications. As observed in **Figure 54**, drying in HMDS causes collapse and loss of the nanostructures compared to HFIP/silk gel dried with $SCCO_2$. Creating structures with high porosity and low bulk density allows these aerogels to be used as nanofilters and sieving devices. The HFIP/silk gels produced in this study had a calculated bulk density of 440 ± 25 kg/m^3 and are 20 times denser than aerogels formed by organic solvent addition or sonication.
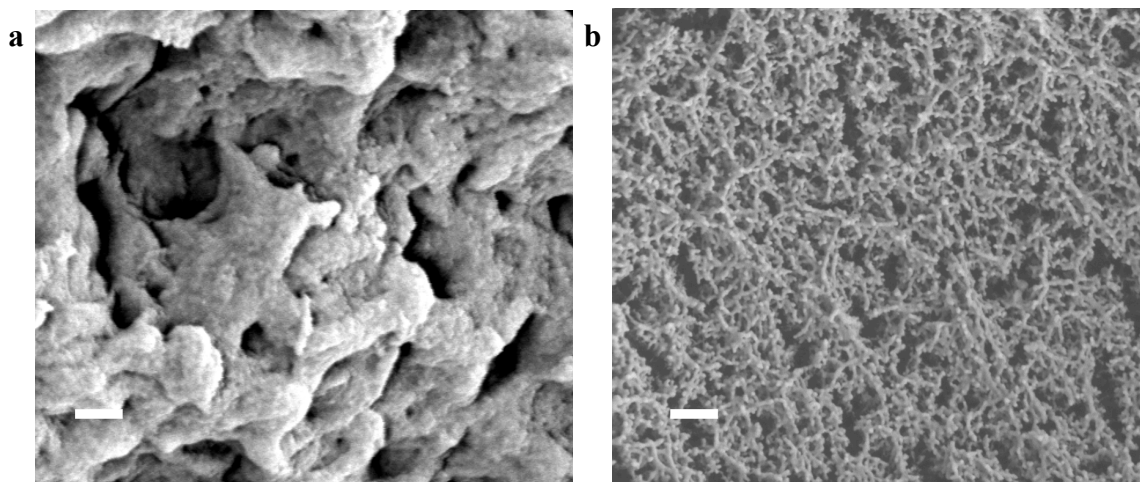
Figure 54. SEM images of HFIP/silk gels after (a) HMDS drying and (b) supercritical drying. Scale bar is 200 nm.

Chemical characterization

ATR-FTIR measurements were used to determine the amorphous to crystalline conformational change of silk fibroin during the sol-gel transition monitored by the Amide I absorbance peak. Analysis of HFIP/silk gels before and after treatment in $SCCO_2$ show a different absorbance spectrum with relatively low beta-sheet content (~36%), however, alpha-helix structures of the protein show a change from 0.0% to 5.8 ± 1.6% for HFIP/silk gels and after exposure to $SCCO_2$ drying respectively (**Figure 55a**). Additionally, the crystal structure after supercritical drying was examined by X-ray diffraction. The X-ray diffraction pattern after $SCCO_2$ drying in **Figure 55b** shows a band at 3.33 Å and a diffuse band from 4.1-4.9 Å.
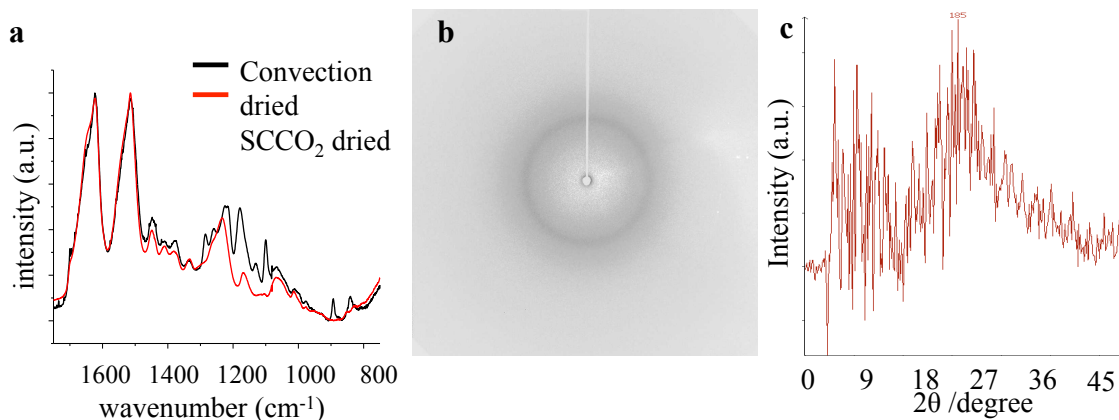
Figure 55. Chemical characterization of HFIP/silk aerogels. a) ATR-FTIR spectra of dried HFIP/silk before supercritical CO_2 dying and after supercritical drying. b) X-ray diffraction pattern of HFIP/silk aerogel after supercritical CO_2 drying. c) Intensity vs. angle plot.

Mechanical characterization

As load bearing materials it is important that HFIP/silk aerogels have adequate bending strength and stiffness if they are to be used as tissue engineering scaffolds. Silk beams were tested in four-point bending in order to produce a load vs. load-displacement curve. From the curve, bending stiffness, structural stiffness, and bending strength were calculated using the methods described in ASTM standard F2502-11.[222] Bending modulus and compression modulus of the HFIP/silk aerogels were also calculated. The compressive modulus was determined to be 33 ± 5 MPa which was lower than the orthopedic hardware for craniofacial plates (2.2 ± 0.3 GPa).[220] The compressive modulus is magnitudes lower than other HFIP formulated silk beams because the concentration and density are lower. Nevertheless, the bending stiffness was calculated to be 29.2 ± 2.1 N/mm, the bending structural stiffness was calculated to be 2018.2 ± 144.3 N-mm^2, and the bending modulus was calculated to be 60.4 ± 14.0 MPa. All the calculated values are lower compared to the previous standard formulation for silk plates and screws, formed

156

by HFIP gelation. However, the concentration and porosity are the limiting factors to determine the mechanical strength of the silk aerogels, but is benefited by the increase in porosity associated with HFIP/silk gels.

HRP and sonicated aerogels
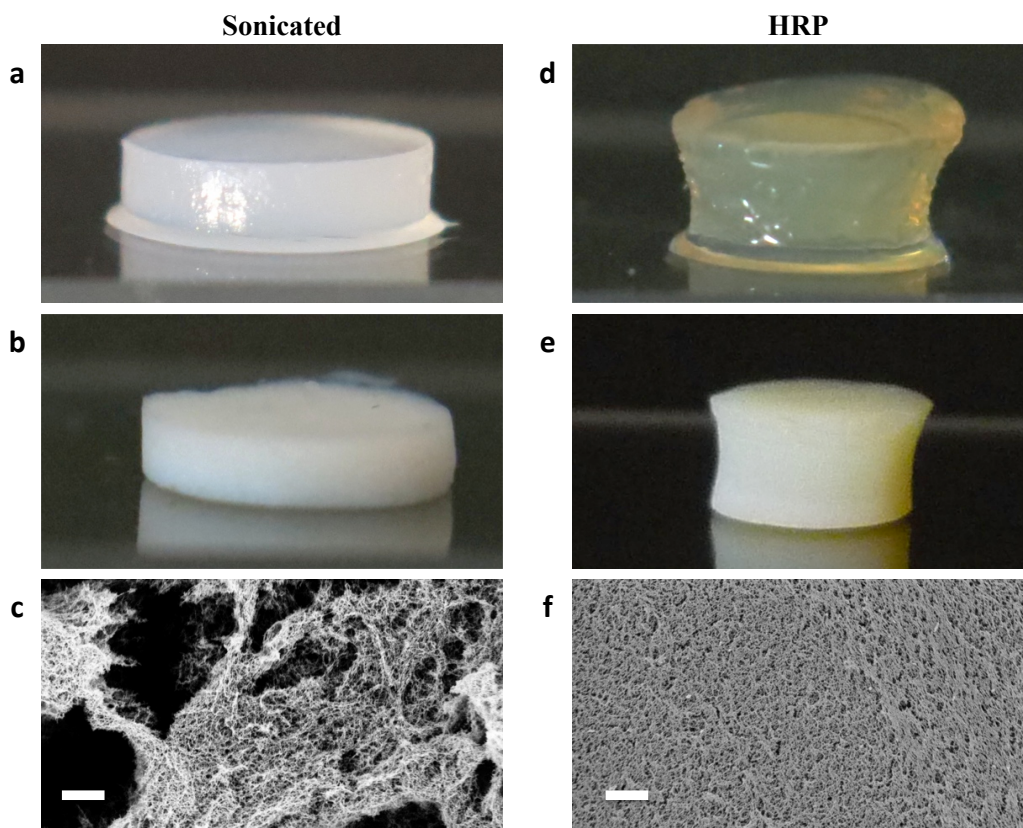
Figure 56. Sonicated (a-c) and HRP aerogels (d-f). (a,d) Images of silk hydrogels induced by sonication and HRP respectively. (b,e) Images of silk aerogels after $SCCO_2$ induced hydrogels by sonication and HRP respectively. (c,f) SEM images of silk aerogels induced by sonication and HRP respectively. Scale bar is 200 nm.

Sonication and HRP induced hydrogels were also examined after dehydrating in ethanol followed by $SCCO_2$ drying (**Figure 56**). The observation of formed nanofibers was apparent, but differed compared to what was observed after drying with HMDS.

Furthermore, the porosity of the HRP induced gels is relatively different compared to sonicated gels. The pores in the HRP induced aerogels are more uniform and smaller comparatively. This observation is noticeable in the SEM images of the two gels after supercritical drying, and also observed in changes to some of the physical properties of the two aerogels (**Figure 56**).

Supercritical drying of silk hydrogels has shown to produce nanofibers above a specific pressure. A similar observation after supercritical drying of sonication induced hydrogels suggests the process of supercritical drying leads to the formation of silk nanofibers. Similar to organic solvent induced silk hydrogels, the nanofibers are between 20-50 nanometers and have a relatively high porosity (**Figure 56**). Therefore, SEM images of the silk hydrogels with and without supercritical drying were examined. SCCO$_2$ drying has been shown to be the catalyst to form nanofibers in silk gels, especially from hydrogels composed of particles. However, not all silk hydrogels are composed of nanoparticles and are made of a network of aggregated silk molecules or form covalently bonded structures. **Figure 57** shows the surface of a sonicated hydrogel and HRP induced hydrogel dried using HMDS, a chemical alternative to supercritical drying. **Figure 57a** shows the morphology similar to hydrogels composed of aggregated silk particles while **Figure 57b** shows the morphology of an HRP induced gel providing a different morphology but similar to one that is already composed of nanofibers. HRP induced hydrogels involves the formation of dityrosine bonds of silk molecules which are apparent in the morphology shown in the SEM images.[221]
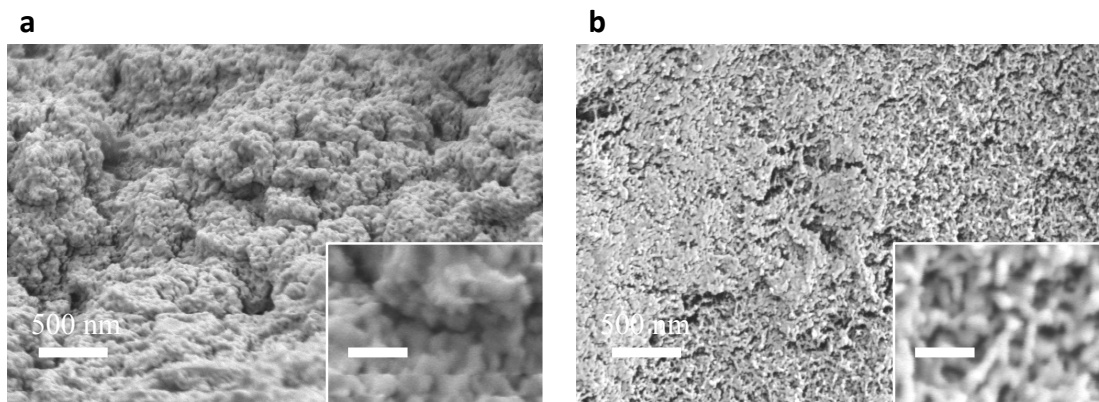
Figure 57. SEM images of sonicated and HRP induced silk hydrogels dried with HMDS. a) Silk hydrogel formed by sonication. b) Silk hydrogel formed by HRP induced gelation. Inset scale bar is 100 nm.

There are significant measured differences between the sonication induced hydrogels and the HRP induced hydrogels (**Figure 58**). Compared to the sonicated aerogels, the HRP induced aerogels show a five-fold increase in bulk density (**Figure 58a**). Each process started with the same initial silk concentration, but show different bulk densities revealing noticeable changes in hydrogel volume. During gelation and ethanol dehydration, there was a noticeable shrinkage in the HRP induced hydrogels that was not observed in the sonication induced samples. This emphasizes the difference in cross-linking and type of cross-linking by HRP induced gels that was also observed in their morphology.
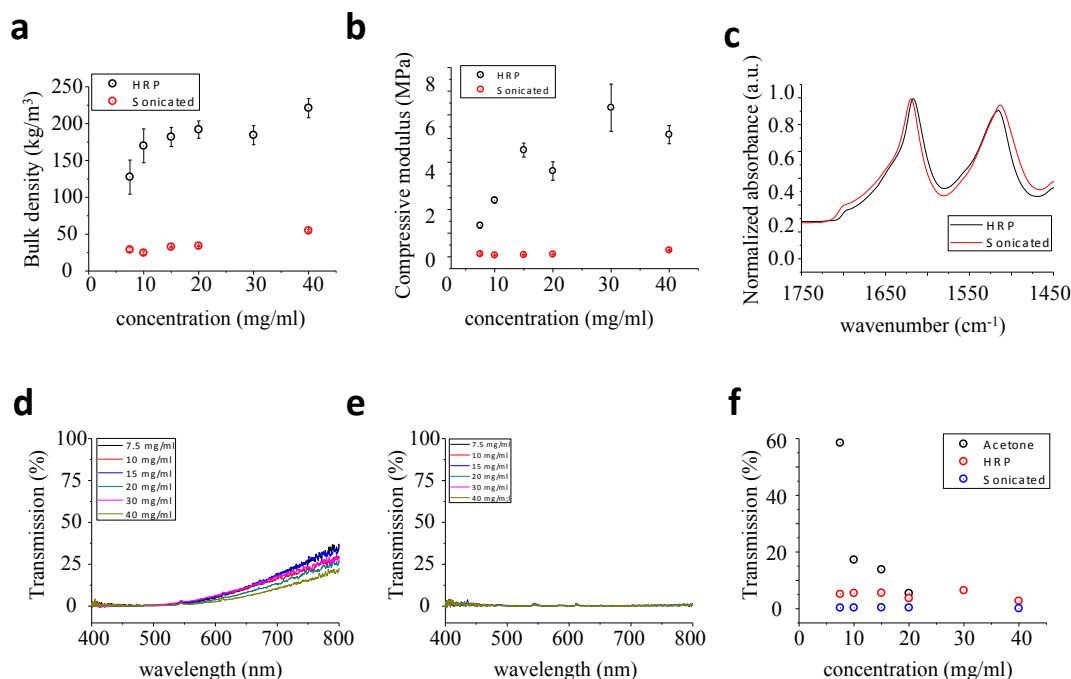
Figure 58. Physical and chemical properties of sonication and HRP induced silk fibroin aerogels. a) Calculated bulk density of aerogels at similar starting concentrations. b) Compressive modulus of aerogels at similar starting concentrations. c) FTIR analysis of aerogels at similar starting concentrations. d-e) Transmission measurements of (d) HRP induced and (e) sonication induced gels. f) Transmission values at 600 nm plotted vs. initial starting concentrations for different synthesized aerogels.

Another noticeable observation between gelling mechanisms is the ability to pass light. Transparency/translucency is important for chemical sensing limited by scattering or absorbance of light.[7] As observed in **Figure 53** and **Figure 56** there is a difference in appearance of the silk gels and the silk aerogels after supercritical drying. The transmission through each of the hydrogels was measured and compared. As shown in the previous chapter, silk aerogels formed by organic solvent induced gelation have a transmission up to 60% at 600 nm and decreases as the concentrations of silk is increased during formation. Hydrogels formed by HRP have a lower transmission in the visible spectrum and remain relatively constant depending on the starting concentration. The

transmission of the aerogels is one-third the transmission of the silk aerogel formed by organic solvent gelation. The hydrogel formed by sonication shows no transmission in the visible spectrum that is observed in the photographs and by the optical measurements.

Another observation is the capability of entrapping specific biomolecules within the hydrogel to act as interactive high surface area sensors. The sonicated hydrogels are ideal for entrapping biomolecules because molecules can be added after sonication but before gelation. However, as stated above, sonicated silk aerogels are not transparent preventing the use of these aerogels as optical sensors due to light loss. Nevertheless, they are still highly porous and can be used as sieving or catalysis platforms to react with biomolecules in flow systems. Entrapping fluorescent molecules and other enzymes within HRP hydrogels was unsuccessful and the silk did not gel. The only known successful molecules possible to be stabilized within the HRP induced hydrogels is HRP, which maintained its activity after supercritical drying as shown in the **Figure 59**.
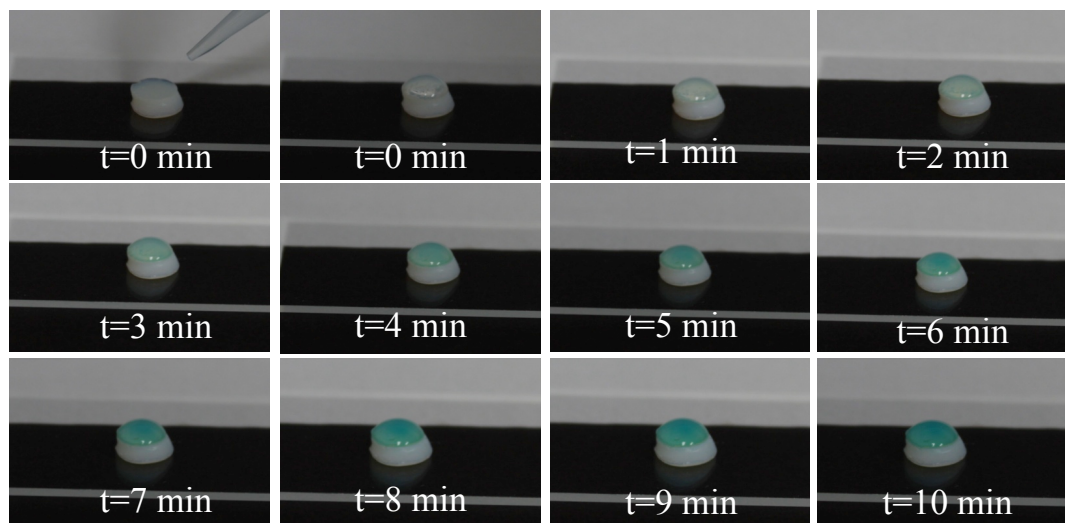
Figure 59. TMB reduction of HRP aerogels at different time points.

Conclusions

As illustrated in this appendix, there are several methods to produce silk fibroin hydrogels to produce aerogels. Processing silk hydrogels via supercritical CO_2 drying yields aerogels with high porosity and silk nanofiber formation. The different hydrogels produced have different characteristics making each one beneficial for certain applications. Examining the mechanical properties, bulk density, transparency, and ability to entrap and stabilize molecules within the gel are characteristics that provide unique interactive biological applications for silk aerogels. The morphology of the samples was examined before and after supercritical drying to better understand any structural change occurring during supercritical conditions. Silk fibroin aerogels can be used as another form where high porosity and nanostructure is required. Similar to silica aerogels, which have different methods to produce slightly different quality aerogels, silk fibroin also shares similar features, and a change during the initial hydrogel formation can change the aerogel application.

Introduction

The crystal structure of proteins provides information about the secondary and tertiary folding used to determine mechanical properties, residual water, and other factors regarding macromolecular function.[10] Semi-crystalline materials can be ordered and arranged in structures determined by their environment and the folding entropy of the molecule.[223,224] Depending on the conditions, such as humidity, pressure, temperature, and solvent concentration, a protein can fold into several different secondary forms.[223]

The primary structure of silk fibroin is composed mainly of glycine, alanine, and serine residues.[116,190] These residues constitute the highly repetitive GAGAGS amino acid motif, which is able to fold into parallel and anti-parallel beta-sheet structures forming semi-crystalline regions.[192] The adjustable mechanical properties and biodegradability are closely related to beta-sheet content and substantial efforts have been devoted to understand the formation of silk structure in its different forms. The crystal structure of silk fibroin has been examined significantly for the past century with several different structure spacing in the fibrous form, regenerated form, and theoretical form.[116,225]

X-ray diffraction is frequently used as a means to investigate the structures, and conclusions determined that various types of silk essentially have the same orthorhombic crystal lattice (**Figure 61**).[191] However, there are also other ways to predict geometric structure of materials, specifically proteins. Methods such as NMR spectroscopy, FTIR spectroscopy, Raman spectroscopy, circular dichroism, and polarized light microscopy

are some examples to provide information regarding final atomic structure.[216] Each method has advantages and disadvantages, and using multiple methods can provide sufficient information to build an atomic model.

Recently, FTIR spectroscopy has been the easiest and most successful method offering quantitative data regarding molecular folding in silk fibroin. FTIR spectroscopy uses infrared light to measure the absorbance of a material characteristic of molecule resonant frequencies. The resonant frequencies are characteristic of bond length and molecular spacing, which provide information regarding protein secondary structure. However, FTIR spectroscopy does not provide detailed information about atomic location and spacing between atoms. Recent understanding and methods require additional information that is not possible from FTIR spectroscopy alone. Therefore, other methods are required to provide more information to determine a protein's three-dimensional structure.

Regenerated silk fibroin from *Bombyx mori* cocoons has been examined by X-ray crystallography, however, has not been examined on the several different forms (amorphous films, crystallized films, hydrogels, lyophilized foams, etc.). Researchers have examined raw silk fibers or films by extracting the dope from silkworm glands, and applied shear to the dope to induce beta-sheet spacing and it compared to raw fibers.[192] Physical action has the potential to change the structure of a silk solution, and under different processing conditions change the physical properties observed in the semi-crystalline structure.
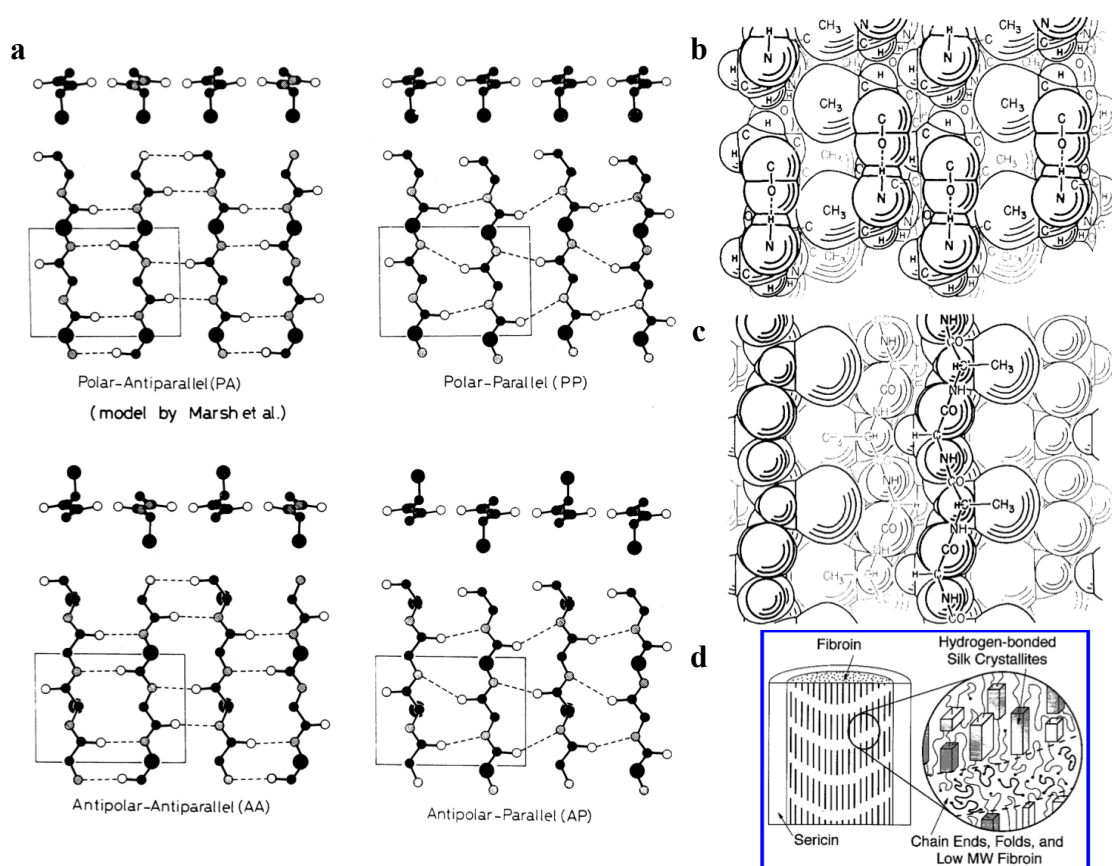
Figure 60. Molecular structure of silk fibroin. a) A theoretical model of the beta-sheet structure of silk fibroin formed by hydrogen bonds. b) The original prediction of silk fibroin crystal structure. c) A theoretical prediction of silk fibroin structure forming semi-crystal structures and their orientation to fiber direction. [116, 226, 227]

In this appendix we show X-ray diffraction patterns of silk fibroin forms processed using different methods. It is apparent by the processing conditions, the silk molecules are rearranged providing more ordered lattice spacing forming different semi-crystal structures. This information can help explain the changes in physical and chemical properties of silk molecules in response to processing methods.

165

Experimental

Preparation of silk formats

Silk materials were made in several different ways as discussed in depth by Rockwood.[108] The forms examined by X-ray diffraction were degummed silk fibers, lyophilized foams, electrospun mats, amorphous silk films, silk films crystallized by methanol and water annealing, and silk dissolved in HFIP and cured with ethanol. Degummed silk fibers were processed using the standard method. Lyophilized foams were prepared by freeze drying a solution of silk fibroin by freezing the solution to -46°C and sublimating the water at 30 mTorr. Amorphous films were prepared by casting silk solution on a flat surface and left to air dry. Silk crystalized in methanol was treated in a bath of 90% methanol, which has shown to be the ideal concentration when crystalizing with alcohols. The films were left in the methanol bath for 30 minutes before drying. Water annealed samples were left for 24 hours in a 100% water vapor environment. Electrospun mats were formed by dissolving silk solution with 3% PEO and spinning with a distance voltage of 18 kV to a grounded surface 11 cm from an injection needle. HFIP/silk gels were prepared by lyophilizing silk solution followed by resolubilizing the lyophilized powder in HFIP. The solution was then cross-linked with ethanol forming a free standing gel.

Methods

X-ray diffraction measurements

Silk materials were prepared as described above. Measurements of the X-ray diffraction patterns from the silk materials were conducted at room temperatures using an

166

Oxford Diffraction Xcalibur PX Ultra System (Oxford Diffraction Ltd., Concord, MA). The CuK$^{\alpha}$ X-ray beam with wavelength of 1.542 Å was generated at 45 kV/40 mA using an Enhance Ultra, a sealed tube-based system incorporating confocal multilayer optics. The X-ray beam was monochromated and the K$^{\beta}$ component was removed by means of the double bounce within the confocal optics. The X-ray beam was focused to 0.3 mm x 0.3 mm (full width at half-maximum at detector position). A two-dimensional Onyx CCD detector (Oxford Diffraction Inc., Concord, MA) with pixel size of 121 μm was placed 62 mm from the sample position, covering the scattering range of Bragg spacing. Exposure time was 150 s.

Results

The diffraction pattern, as explain above, is significant of the arrangement of the atoms in molecules.[116,192] Differences in the patterns are associated with the changes in the molecular spacing caused by the physical changes leading to potentially higher ordered structures.[190,193,226] The arrangement of the secondary structures within silk compared to the tertiary structures are essentially undetermined. Previously, FTIR has been the method of choice, which is an easy and effective method to determine changes in the ordered arrangement of silk.[198] However, FTIR only offers information regarding bending bonds and the length of those bonds, not the direct spacing between molecules. FTIR is used to analyze the effects of repetitive amino acid sequences on the formation of crystals, and have indicated the importance of the contribution of the beta-sheet structure.[198] It is this three dimensional information that is provided using X-ray

diffraction which makes it an ideal and usable technique to determine changes to silk semi-crystalline structure.

In **Figure 61** there are bands associated with the X-ray diffraction pattern of lattice structures of a silk fiber and electronspun fiber. Previous studies have shown that silk has a beta-sheet with spacing associated with shear during fiber formation.[192] **Figure 61a** shows a degummed fiber with a two diffuse bands. The bands are similar to previous findings and are fundamental to understand the new findings.[116,192–194] The fiber form of silk is the most noticeable and understandable, which is why it was originally examined by X-ray diffraction. As fibers are the natural form of silk fibroin, electrospun fibers were also examined. **Figure 61b** shows an electrospun silk mat with two distinct bands with spacing 3.85Å and 4.62 Å. Electrospinning not only forms fibers, but induces shear by pulling the solution and stretches the fibers as they dry. This can cause a change in diffraction pattern as was observed by applying shear on the fiber dope.[192]
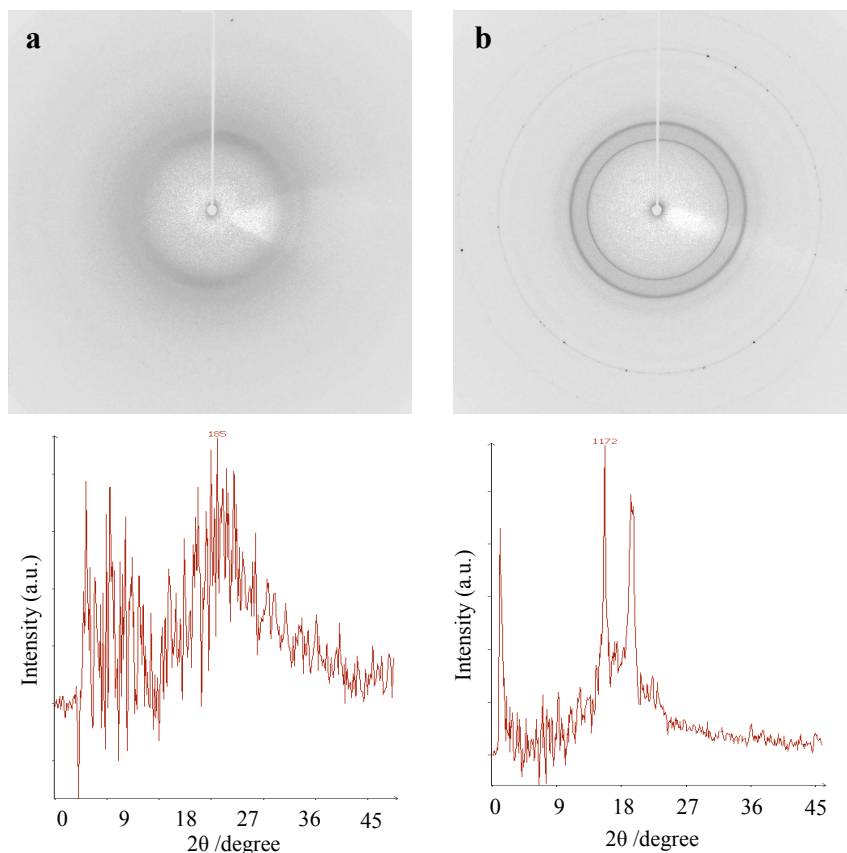
Figure 61. X-ray scattering of silk fibers. Images of 2D X-ray scattering patterns and intensity vs. angle plots of a) a silk fiber and b) electrospun silk fibers.

Figure 62 shows two dried gel forms made after lyophilization and crosslinking a solution of HFIP/silk with ethanol. Silk gel states have been used as tissue engineered scaffolds for craniofacial replacements and as sustained drug delivery vehicles.[103,220] As with other silk forms, FTIR spectra were used to describe beta-sheet content of the silk, however, it is necessary to measure additional structures of these materials. **Figure 62a** shows the diffraction pattern of a lyophilized silk foam having a diffuse band with spacing 3.24-6.40 Å. The diffuse band falls within the range associated with silk materials. Additionally, **Figure 62b** shows an HFIP and ethanol treated silk hydrogel with a sharper band compared to the lyophilized foam with spacing 4.08-4.83 Å, and is

structurally different than either the silk fiber, electrospun mat, or lyophilized foam. These diffraction patterns show the different crystal structures silk can have, which shows how the polymorphism of silk correlates to its crystal structure by its processing method.
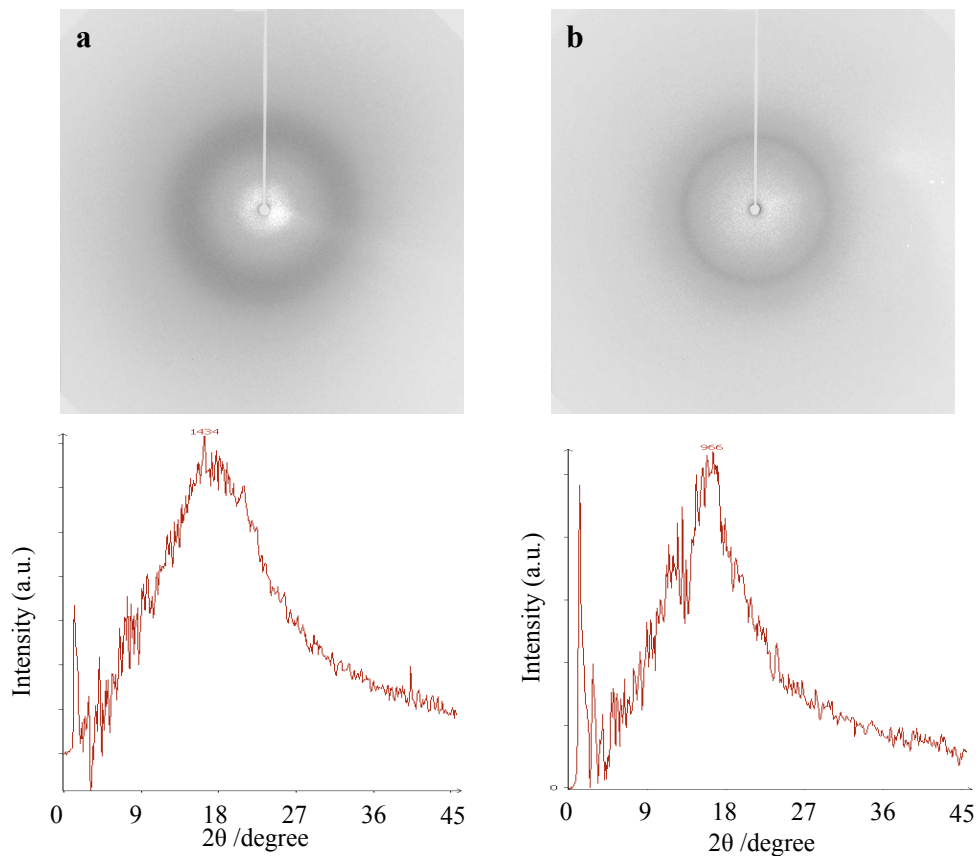
Figure 62. X-ray scattering of silk gels. Images of 2D X-ray scattering patterns and angle vs. intensity plots of a) lyophylized silk and b) silk fibroin dissolved in HFIP and cured with 100% ethanol

Finally, there has been significant work on understanding the beta-sheet content of silk films.[159,181,198,208] Three structural models have been reported to exist in silk fibroin; silk I, II, and III.[198] Silk I is the amorphous, water soluble structure existing within the gland before spinning, silk II is the insoluble beta-sheet structure, and silk III is an unstable structure observed at water-air interfaces.[198] Processing of silk fibroin differently

relates to these transitions in structure and have been thoroughly examined by FTIR. Processing the as made amorphous silk films in alcohols or by water vapor annealing, where a sample is saturated in a humid environment of water, changes the Amide I to more order structures.[198] **Figure 63** shows different post processing of silk films from amorphous to more crystalized states and signify more order in lattice structures. **Figure 63a** shows an amorphous silk film with a relatively low intensity, diffuse band. This agrees well with FTIR data and structural stability of the film since it easily dissolves in water. The less ordered semi-crystal structure shown by the X-ray diffraction correlates well with theorized silk structure. **Figure 63b** shows a water-annealed silk film with a distinct band with spacing 4.17 Å and a diffuse band from 2.97-7.71 Å. The increase in intensity is observed in the diffraction pattern (the dark bands) associated with more structural order. This report is also confirmed by different amounts of beta-sheet structure as determined by different amount of water annealing and at different temperatures.[181,198]

Figure 63c shows a methanol treated silk film with a different diffraction pattern compared to amorphous films and water annealed silk films. There is a distinct band at 4.48 Å surrounded by a diffuse region at 3.57-4.95 Å. The changes in X-ray diffraction patterns are associated with the amount of change induced during cross-linking. Water-annealed films appear to have more crystal structure and could be a result of easier movement of the molecules. Nevertheless, the lattice patterns in silk materials show changes depending on their processing conditions.
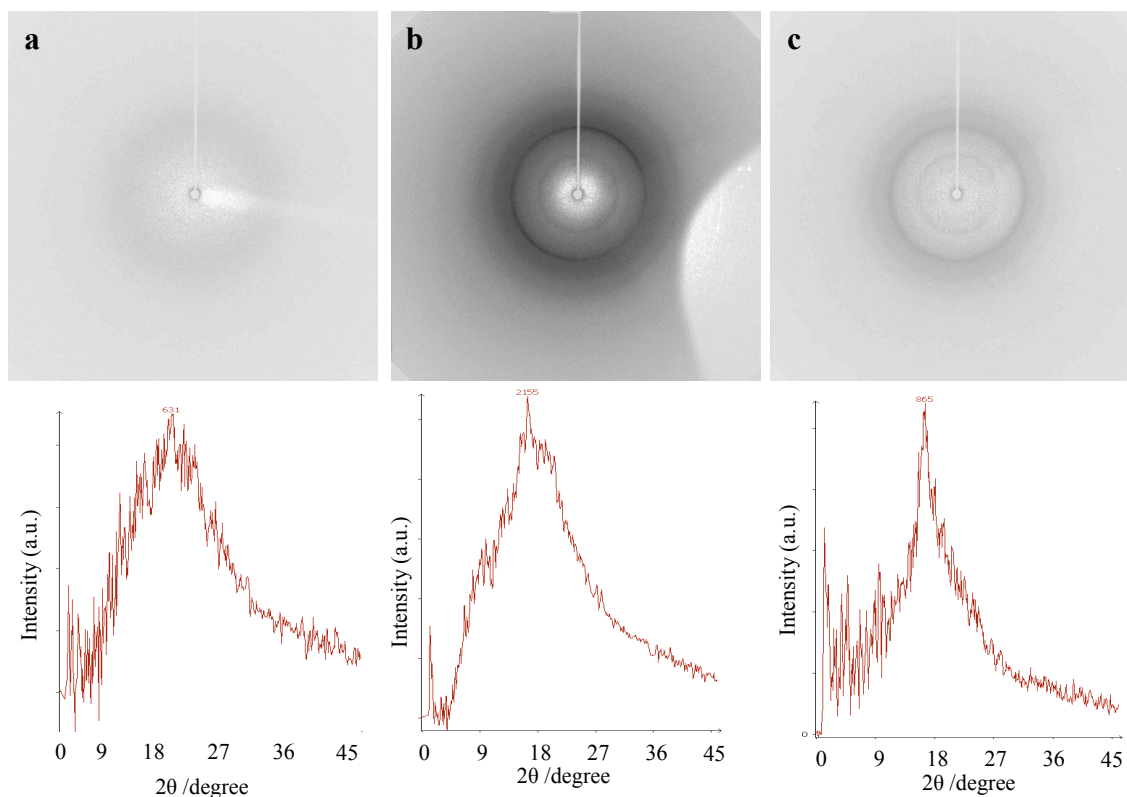
Figure 63. X-ray scattering of silk films. Images of 2D X-ray scattering patterns and intesnity vs. angle of silk films. The patterns correlate to a) a regenerated amorphous silk film, b) water annealed film, and c) a methanol treated cross-linked silk film.

There is much more structure in each silk form depending on processing that has not been shown until now. The theoretical and measured beta-sheet structure of silk has been around for over 60 years using X-ray crystallography, but the individual forms studied in this appendix have not been examined. Studying different silk semi-crystalline structures offers more information about beta-sheet content compared to FTIR analysis to help with understanding degradation time and mechanical properties.

Conclusions

Here we have provided information about silk fibroin that has not been previously examined using X-ray crystallography. X-ray crystallography is a powerful tool to provide information regarding the ordered lattice spacing in silk materials that is not apparent using FTIR spectroscopy or Raman spectroscopy. If more information can be discovered about silk relating to its secondary structure, then there may be additional opportunities regarding the processing parameters beyond temperature and humidity to affect molecular arrangements that relates to the different polymorphs of regenerated silk fibroin solution.

REFERENCES

1. J. Y. Cheng, A. M. Mayes, and C. A. Ross, *Nat. Mater.*, 2004, **3**, 823–8.

2. M. Shibayama and N. Osaka, *Macromol. Symp.*, 2010, **291-292**, 115–121.

3. A. E. Nel, L. Mädler, D. Velegol, T. Xia, E. M. V Hoek, P. Somasundaran, F. Klaessig, V. Castranova, and M. Thompson, *Nat. Mater.*, 2009, **8**, 543–57.

4. A. Frenot and I. S. Chronakis, *Curr. Opin. Colloid Interface Sci.*, 2003, 8, 64–75.

5. L. W. Hrubesh, *J. Non. Cryst. Solids*, 1998, 225, 335–342.

6. M. Schmidt and F. Schwertfeger, *J. Non. Cryst. Solids*, 1998, 225, 364–368.

7. M. Aegerter, N. Leventis, and M. Koebel, Eds., *Aerogel Handbook*, Springer, New York, 2011.

8. J. Tan and W. M. Saltzman, *Biomaterials*, 2004, **25**, 3593–601.

9. M. R. Ayers and A. J. Hunt, *J. Non. Cryst. Solids*, 1998, **225**, 343–347.

10. J. L. Finney and D. D. Eley, *Philos. Trans. R. Soc. B Biol. Sci.*, 1977, **278**, 3–32.

11. E. Brandenburg, H. V Berlepsch, J. Leiterer, F. Emmerling, and B. Koksch, *Biomacromolecules*, 2012, **13**, 3542–51.

12. K. Heremans and L. Smeller, *Biochim. Biophys. Acta - Protein Struct. Mol. Enzymol.*, 1998, **1386**, 353–370.

13. *The World Book encyclopedia.*, 2015.

14. J. M. DeSimone and W. Tumas, Eds., *Green chemistry using liquid and supercritical carbon dioxide*, Oxford University Press, Inc., Oxford, 2003.

15. M. Purcell, S. M. Howdle, K. M. Shakesheff, and L. J. White, *Rec. Pat. Regen. Med.*, 2013, 237–248.

16. A. I. Cooper, *J. Mater. Chem.*, 2000, **10**, 207–234.

17. G. Brunner, *Annu. Rev. Chem. Biomol. Eng.*, 2010, 1, 321–342.

18. S. G. Kazarian, *Polym. Sci.*, 2000, **42**, 78–101.

19. J. L. Silva, D. Foguel, and C. A. Royer, *Trends Biochem. Sci.*, 2001, **26**, 612–618.

20. C. Krywka, C. Sternemann, M. Paulus, M. Tolan, C. Royer, and R. Winter, *Chemphyschem*, 2008, **9**, 2809–15.

21. Y. P. Handa, Z. Zhang, and B. Wong, *Macromolecules*, 1997, **30**, 8499–8504.

22. A. Aertsen, F. Meersman, M. E. G. Hendrickx, R. F. Vogel, and C. W. Michiels, *Trends Biotechnol.*, 2009, 27, 434–441.

23. D. L. Tomasko, H. Li, D. Liu, X. Han, M. J. Wingert, L. J. Lee, and K. W. Koelling, *Ind. Eng. Chem. Res.*, 2003, 42, 6431–6456.

24. M. Bhamidipati, A. M. Scurto, and M. S. Detamore, *Tissue Eng. Part B. Rev.*, 2013, **19**, 221–32.

25. S. Areerat, E. Funami, Y. Hayata, D. Nakagawa, and M. Ohshima, *Polym. Eng. Sci.*, 2004, **44**, 1915–1924.

26. M. Takada, M. Tanigaki, and M. Ohshima, *Polym. Eng. Sci.*, 2001, **41**, 1938–1946.

27. B. D. Ulery, L. S. Nair, and C. T. Laurencin, *J. Polym. Sci. B. Polym. Phys.*, 2011, **49**, 832–864.

28. C. Wang, R. J. Stewart, and J. Kopecek, *Nature*, 1999, **397**, 417–20.

29. T. Kietzke, D. Neher, K. Landfester, R. Montenegro, R. Güntner, and U. Scherf, *Nat. Mater.*, 2003, **2**, 408–12.

30. R. Karnik, F. Gu, P. Basto, C. Cannizzaro, L. Dean, W. Kyei-Manu, R. Langer, and O. C. Farokhzad, *Nano Lett.*, 2008, **8**, 2906–12.

31. S. Schubert, J. T. Delaney, Jr, and U. S. Schubert, *Soft Matter*, 2011, **7**, 1581–1588.

32. N. Anton, F. Bally, C. A. Serra, A. Ali, Y. Arntz, Y. Mely, M. Zhao, E. Marchioni, A. Jakhmola, and T. F. Vandamme, *Soft Matter*, 2012, **8**, 10628.

33. E. J. Lee, S. A. Khan, and K.-H. Lim, *J. Biomater. Sci. Polym. Ed.*, 2011, **22**, 753–71.

34. C. A. Serra and Z. Chang, *Chem. Eng. Technol.*, 2008, **31**, 1099–1115.

35. D. N. Breslauer, S. J. Muller, and L. P. Lee, *Biomacromolecules*, 2010, **11**, 643–7.

36. A. S. Hoffman, *Adv. Drug Deliv. Rev.*, 2002, **54**, 3–12.

37.   E. Tsotsas and A. S. Mujumdar, Eds., *Modern Drying Technology*, Wiley-VCH Verlag GmbH & Co. KGaA, Weinheim, Germany, 2011.

38.   L. L. Hench and J. K. West, *Chem. Rev.*, 1990, **90**, 33–72.

39.   W. A. Petka, *Science (80-.).*, 1998, **281**, 389–392.

40.   C. J. Brinker and G. W. Scherer, *Sol-gel science: the physics and chemistry of sol-gel processing*, 1990, vol. 8.

41.   D. R. Ulrich, *J. Non. Cryst. Solids*, 1990, **121**, 465–479.

42.   J. L. Drury and D. J. Mooney, *Biomaterials*, 2003, **24**, 4337–4351.

43.   K. Y. Lee and D. J. Mooney, *Chem. Rev.*, 2001, **101**, 1869–1880.

44.   N. A. Peppas, J. Z. Hilt, A. Khademhosseini, and R. Langer, *Adv. Mater.*, 2006, **18**, 1345–1360.

45.   B. D. Lawrence, M. Cronin-Golomb, I. Georgakoudi, D. L. Kaplan, and F. G. Omenetto, *Biomacromolecules*, 2008, **9**, 1214–20.

46.   J. P. Jung, J. Z. Gasiorowski, and J. H. Collier, *Biopolymers*, 2010, **94**, 49–59.

47.   N. Peppas, *Eur. J. Pharm. Biopharm.*, 2000, **50**, 27–46.

48.   S. S. Anumolu, A. S. DeSantis, A. R. Menjoge, R. A. Hahn, J. A. Beloni, M. K. Gordon, and P. J. Sinko, *Biomaterials*, 2010, **31**, 964–74.

49.   X. Calderón-Colón, Z. Xia, J. L. Breidenich, D. G. Mulreany, Q. Guo, O. M. Uy, J. E. Tiffany, D. E. Freund, R. L. McCally, O. D. Schein, J. H. Elisseeff, and M. M. Trexler, *Biomaterials*, 2012, **33**, 8286–95.

50.   W. Liu, K. Merrett, M. Griffith, P. Fagerholm, S. Dravida, B. Heyne, J. C. Scaiano, M. A. Watsky, N. Shinozaki, N. Lagali, R. Munger, and F. Li, *Biomaterials*, 2008, **29**, 1147–58.

51.   Y. Feng, J. Foster, S. Mi, B. Chen, and C. J. Connon, *Exp. Eye Res.*, 2012, **101**, 97–103.

52.   J. H. Fitton, B. A. Dalton, G. Beumer, G. Johnson, H. J. Griesser, and J. G. Steele, *J. Biomed. Mater. Res.*, 1998, **42**, 245–257.

53.   S. J. Liliensiek, S. Campbell, P. F. Nealey, and C. J. Murphy, *J. Biomed. Mater. Res. A*, 2006, **79**, 185–92.

54. T. A. E. Ahmed, E. V Dare, and M. Hincke, *Tissue Eng. Part B. Rev.*, 2008, **14**, 199–215.

55. A. D. Augst, H. J. Kong, and D. J. Mooney, *Macromol. Biosci.*, 2006, **6**, 623–33.

56. M. Choi, J. W. Choi, S. Kim, S. Nizamoglu, S. K. Hahn, and S. H. Yun, *Nat. Photonics*, 2013, **7**, 987–994.

57. C. M. Hassan and N. A. Peppas, *Biopolymers · PVA Hydrogels, Anionic Polymerisation Nanocomposites*, Springer Berlin Heidelberg, Berlin, Heidelberg, 2000, vol. 153.

58. M. P. Lutolf and J. A. Hubbell, *Nat. Biotechnol.*, 2005, **23**, 47–55.

59. M. D. Shoulders and R. T. Raines, *Annu. Rev. Biochem.*, 2009, **78**, 929–58.

60. J. Zhu, *Biomaterials*, 2010, **31**, 4639–56.

61. G. P. Raeber, M. P. Lutolf, and J. A. Hubbell, *Biophys. J.*, 2005, **89**, 1374–88.

62. T. Tanigami, K. Yano, K. Yamaura, and S. Matsuzawa, *Polymer (Guildf).*, 1995, **36**, 2941–2946.

63. T. Tanigami, Y. Nakashima, K. Murase, H. Suzuki, K. Yamaura, and S. Matsuzawa, *J. Mater. Sci.*, 1995, **30**, 5110–5120.

64. T. Tanigami, K. Murase, K. Yamaura, and S. Matsuzawa, *Polymer (Guildf).*, 1994, **35**, 2573–2578.

65. G. M. Nogueira, M. A. de Moraes, A. C. D. Rodas, O. Z. Higa, and M. M. Beppu, *Mater. Sci. Eng. C*, 2011, **31**, 997–1001.

66. T. Yucel, P. Cebe, and D. L. Kaplan, *Biophys. J.*, 2009, **97**, 2044–50.

67. S. Nagarkar, T. Nicolai, C. Chassenieux, and A. Lele, *Phys. Chem. Chem. Phys.*, 2010, **12**, 3834–44.

68. X. Wang, J. A. Kluge, G. G. Leisk, and D. L. Kaplan, *Biomaterials*, 2008, **29**, 1054–64.

69. P.-H. G. Chao, S. Yodmuang, X. Wang, L. Sun, D. L. Kaplan, and G. Vunjak-Novakovic, *J. Biomed. Mater. Res. B. Appl. Biomater.*, 2010, **95**, 84–90.

70. A. M. Hopkins, L. De Laporte, F. Tortelli, E. Spedden, C. Staii, T. J. Atherton, J. A. Hubbell, and D. L. Kaplan, *Adv. Funct. Mater.*, 2013, **23**, 5140–5149.

71. G. W. Scherer, *J. Am. Ceram. Soc.*, 1990, **73**, 3–14.

72. G. W. Scherer, *J. Non. Cryst. Solids*, 1989, **109**, 171–182.

73. G. W. Scherer, *J. Non. Cryst. Solids*, 1993, 155, 1–25.

74. J. R. Williams, A. A. Clifford, and S. H. R. al-Saidi, *Mol. Biotechnol.*, 2002, **22**, 263–286.

75. N. Hüsing and U. Schubert, *Angew. Chemie Int. Ed.*, 1998, **37**, 22–45.

76. A. Soleimani Dorcheh and M. H. Abbasi, *J. Mater. Process. Technol.*, 2008, 199, 10–26.

77. T. Woignier and J. Phalippou, *J. Non. Cryst. Solids*, 1988, 100, 404–408.

78. M. J. Bommel and A. B. Haan, *J. Mater. Sci.*, 1994, 29, 943–948.

79. L. Kocon, F. Despetis, and J. Phalippou, *J. Non. Cryst. Solids*, 1998, 225, 96–100.

80. D. W. Schaefer, R. Pekala, and G. Beaucage, *J. Non. Cryst. Solids*, 1995, 186, 159–167.

81. R. Saliger, V. Bock, R. Petricevic, T. Tillotson, S. Geis, and J. Fricke, *J. Non. Cryst. Solids*, 1997, 221, 144–150.

82. T. Horikawa, J. Hayashi, and K. Muroyama, *Carbon N. Y.*, 2004, **42**, 1625–1633.

83. C. Liang, G. Sha, and S. Guo, *J. Non. Cryst. Solids*, 2000, **271**, 167–170.

84. J. Li, X. Wang, Q. Huang, S. Gamboa, and P. J. Sebastian, *J. Power Sources*, 2006, **158**, 784–788.

85. F. Fischer, A. Rigacci, R. Pirard, S. Berthon-Fabry, and P. Achard, *Polymer (Guildf).*, 2006, **47**, 7636–7645.

86. H. MAEDA, M. NAKAJIMA, T. HAGIWARA, T. SAWAGUCHI, and S. YANO, *KOBUNSHI RONBUNSHU*, 2006, 63, 135–137.

87. J. Cai, S. Kimura, M. Wada, S. Kuga, and L. Zhang, *ChemSusChem*, 2008, **1**, 149–154.

88. H. Jin, Y. Nishiyama, M. Wada, and S. Kuga, *Colloids Surfaces A Physicochem. Eng. Asp.*, 2004, **240**, 63–67.

89. J. Cai, S. Kimura, M. Wada, S. Kuga, and L. Zhang, *ChemSusChem*, 2008, **1**, 149–154.

90. T. Oshima, T. Sakamoto, K. Ohe, and Y. Baba, *Carbohydr. Polym.*, 2014, **103**, 62–69.

91. H. Jin, M. Kettunen, A. Laiho, H. Pynnönen, J. Paltakari, A. Marmur, O. Ikkala, and R. H. A. Ras, *Langmuir*, 2011, **27**, 1930–1934.

92. C. A. Garcia-Gonzalez, M. Alnaief, and I. Smirnova, *Carbohydr. Polym.*, 2011, **86**, 1425–1438.

93. M. R. Ayers and A. J. Hunt, *J. Non. Cryst. Solids*, 2001, **285**, 123–127.

94. X. Chang, D. Chen, and X. Jiao, *J. Phys. Chem. B*, 2008, **112**, 7721–7725.

95. J. Fricke, *J. Non. Cryst. Solids*, 1990, 121, 188–192.

96. S. S. Kistler, *Nature*, 1931, 127, 741.

97. H. D. Gesser and P. C. Goswami, *Chem. Rev*, 1989, **89**, 765.

98. H. Qi, E. Mäder, and J. Liu, *J. Mater. Chem. A*, 2013, **1**, 9714.

99. R. R. Mallepally, M. A. Marin, and M. A. McHugh, *Acta Biomater.*, 2014.

100. M. A. Marin, R. R. Mallepally, and M. A. McHugh, *J. Supercrit. Fluids*, 2014, **91**, 84–89.

101. M. L. Floren, S. Spilimbergo, A. Motta, and C. Migliaresi, *Biomacromolecules*, 2012, **13**, 2060–2072.

102. Y. S. Yun, S. Y. Cho, and H.-J. Jin, *Macromol. Res.*, 2014, **22**, 509–514.

103. N. Guziewicz, A. Best, B. Perez-Ramirez, and D. L. Kaplan, *Biomaterials*, 2011, **32**, 2642–50.

104. S. Lu, X. Wang, Q. Lu, X. Hu, N. Uppal, F. G. Omenetto, and D. L. Kaplan, *Biomacromolecules*, 2009, **10**, 1032–42.

105. J. Zhang, E. Pritchard, X. Hu, T. Valentin, B. Panilaitis, F. G. Omenetto, and D. L. Kaplan, *Proc. Natl. Acad. Sci. U. S. A.*, 2012, **109**, 11981–6.

106. C. Vepari and D. L. Kaplan, *Prog. Polym. Sci.*, 2007, **32**, 991–1007.

107. F. G. Omenetto and D. L. Kaplan, *Nat. Photonics*, 2008, 2, 641–643.

108.   D. N. Rockwood, R. C. Preda, T. Yücel, X. Wang, M. L. Lovett, and D. L. Kaplan, *Nat. Protoc.*, 2011, **6**, 1612–31.

109.   G. H. Altman, F. Diaz, C. Jakuba, T. Calabro, R. L. Horan, J. Chen, H. Lu, J. Richmond, and D. L. Kaplan, *Biomaterials*, 2003, **24**, 401–416.

110.   U.-J. Kim, J. Park, C. Li, H.-J. Jin, R. Valluzzi, and D. L. Kaplan, *Biomacromolecules*, 2004, **5**, 786–92.

111.   F. G. Omenetto and D. L. Kaplan, *Science*, 2010, **329**, 528–531.

112.   B. D. Lawrence, J. K. Marchant, M. A. Pindrus, F. G. Omenetto, and D. L. Kaplan, *Biomaterials*, 2009, **30**, 1299–308.

113.   S. Kim, A. N. Mitropoulos, J. D. Spitzberg, H. Tao, D. L. Kaplan, and F. G. Omenetto, *Nat. Photonics*, 2012, **6**, 818–823.

114.   A. R. Murphy and D. L. Kaplan, *J. Mater. Chem.*, 2009, **19**, 6443–6450.

115.   H.-J. Jin and D. L. Kaplan, *Nature*, 2003, **424**, 1057–61.

116.   R. E. Marsh, R. B. Corey, and L. Pauling, *Biochim. Biophys. Acta*, 1955, **16**, 1–34.

117.   T. Terashima, T. Sugita, K. Fukae, and M. Sawamoto, *Macromolecules*, 2014, **47**, 589–600.

118.   G. Rialdi and E. Battistel, *Biophys. Chem.*, 2007, **126**, 65–79.

119.   S. Zarkoob, D. H. Reneker, R. K. Eby, S. D. Hudson, D. Ertley, and W. W. Adams, in *American Chemical Society, Polymer Preprints, Division of Polymer Chemistry*, ACS, 1998, vol. 39, pp. 244–245.

120.   S. Kim, B. Marelli, M. A. Brenckle, A. N. Mitropoulos, E.-S. Gil, K. Tsioris, H. Tao, D. L. Kaplan, and F. G. Omenetto, *Nat. Nanotechnol.*, 2014, **9**, 306–10.

121.   M. A. Northrup, *Nat. Mater.*, 2004, **3**, 282–3.

122.   G. F. Christopher and S. L. Anna, *J. Phys. D. Appl. Phys.*, 2007, **40**, R319–R336.

123.   E. Castro-Hernández, V. Gundabala, A. Fernández-Nieves, and J. M. Gordillo, *New J. Phys.*, 2009, **11**, 075021.

124.   Y. Morimoto, K. Kuribayashi-Shigetomi, and S. Takeuchi, *J. Micromechanics Microengineering*, 2011, **21**, 054031.

125.   J. Wang, J. Zhang, and J. Han, *Front. Chem. Eng. China*, 2010, **4**, 26–36.

126. W. J. Duncanson, T. Lin, A. R. Abate, S. Seiffert, R. K. Shah, and D. A. Weitz, *Lab Chip*, 2012, **12**, 2135–45.

127. T. Schneider, G. H. Chapman, and U. O. Häfeli, *Colloids Surf. B. Biointerfaces*, 2011, **87**, 361–8.

128. W. Lee, L. M. Walker, and S. L. Anna, *Phys. Fluids*, 2009, **21**, 032103.

129. Q. Xu, M. Hashimoto, T. T. Dang, T. Hoare, D. S. Kohane, G. M. Whitesides, R. Langer, and D. G. Anderson, *Small*, 2009, **5**, 1575–81.

130. A. O. Elzoghby, W. M. Samy, and N. A. Elgindy, *J. Control. Release*, 2012, **161**, 38–49.

131. U. O. Häfeli, *Int. J. Pharm.*, 2004, **277**, 19–24.

132. K. M. L. Taylor, J. S. Kim, W. J. Rieter, H. An, W. Lin, and W. Lin, *J. Am. Chem. Soc.*, 2008, **130**, 2154–5.

133. T. Pham, J. B. Jackson, N. J. Halas, and T. R. Lee, *Langmuir*, 2002, **18**, 4915–4920.

134. E. M. Pritchard and D. L. Kaplan, *Expert Opin. Drug Deliv.*, 2011, **8**, 797–811.

135. X. Wang, E. Wenk, A. Matsumoto, L. Meinel, C. Li, and D. L. Kaplan, *J. Control. Release*, 2007, **117**, 360–70.

136. A. B. Mathur and V. Gupta, *Nanomedicine (Lond).*, 2010, **5**, 807–20.

137. B. B. Mandal and S. C. Kundu, *Nanotechnology*, 2009, **20**, 355101.

138. V. Gupta, A. Aseh, C. N. Ríos, B. B. Aggarwal, and A. B. Mathur, *Int. J. Nanomedicine*, 2009, **4**, 115–122.

139. E. M. Pritchard, P. B. Dennis, F. Omenetto, R. R. Naik, and D. L. Kaplan, *Biopolymers*, 2012, **97**, 479–98.

140. J.-H. Yeo, K.-G. Lee, Y.-W. Lee, and S. Y. Kim, *Eur. Polym. J.*, 2003, **39**, 1195–1199.

141. Z. Zhao, A. Chen, Y. Li, J. Hu, X. Liu, J. Li, Y. Zhang, G. Li, and Z. Zheng, *J. Nanoparticle Res.*, 2012, **14**, 736.

142. L. Wang, Z. R. Xia, L. L. Lv, Q. Tang, and M. Z. Li, *Adv. Mater. Res.*, 2011, **236-238**, 1902–1905.

143. T. Hino, S. Shimabayashi, and A. Nakai, *Pharm. Pharmacol. Commun.*, 2000, **6**, 335–339.

144. U. K. Slotta, S. Rammensee, S. Gorb, and T. Scheibel, *Angew. Chem. Int. Ed. Engl.*, 2008, **47**, 4592–4.

145. A. Lammel, M. Schwab, U. Slotta, G. Winter, and T. Scheibel, *ChemSusChem*, 2008, **1**, 413–6.

146. Z. Cao, X. Chen, J. Yao, L. Huang, and Z. Shao, *Soft Matter*, 2007, **3**, 910.

147. P. Shi and J. C. H. Goh, *Powder Technol.*, 2012, **215-216**, 85–90.

148. E. Wenk, A. J. Wandrey, H. P. Merkle, and L. Meinel, *J. Control. Release*, 2008, **132**, 26–34.

149. Y. Srisuwan, P. Srihanam, and Y. Baimark, *J. Macromol. Sci. Part A*, 2009, **46**, 521–525.

150. Y. Baimark, P. Srihanam, Y. Srisuwan, and P. Phinyocheep, *J. Appl. Polym. Sci.*, 2010, **118**, n/a–n/a.

151. R. J. Xie, H. Y. Wu, M. N. Zhu, and Y. Y. Huang, *Adv. Mater. Res.*, 2011, **175-176**, 110–115.

152. C. W. Park, S. Y. Lee, and W. Hur, *Polym.*, 2010, **34**, 321–325.

153. S. J. Myung, H. S. Kim, Y. Kim, P. Chen, and H. J. Jin, *Macromol. Res.*, 2008, **16**, 604–608.

154. X. Wang, T. Yucel, Q. Lu, X. Hu, and D. L. Kaplan, *Biomaterials*, 2010, **31**, 1025–35.

155. P. Hiemenz, *Principles of colloid and surface chemistry.*, Marcel Dekker, New York, 1997.

156. B. Berne, *Dynamic light scattering : with applications to chemistry, biology, and physics*, Wiley, New York, 1976.

157. T. Nisisako, T. Torii, and T. Higuchi, *Chem. Eng. J.*, 2004, **101**, 23–29.

158. L. S. Wray, X. Hu, J. Gallego, I. Georgakoudi, F. G. Omenetto, D. Schmidt, and D. L. Kaplan, *J. Biomed. Mater. Res. B. Appl. Biomater.*, 2011, **99**, 89–101.

159. X. Hu, D. Kaplan, and P. Cebe, *Macromolecules*, 2008, **41**, 3939–3948.

160. H. Tao, D. L. Kaplan, and F. G. Omenetto, *Adv. Mater.*, 2012, **24**, 2824–37.

161. J. Zhu and R. E. Marchant, *Expert Rev. Med. Devices*, 2011, **8**, 607–26.

162. T. Chirila, Z. Barnard, Zainuddin, and D. Harkin, in *Materials Science Forum*, 2007, vol. 561-565, pp. 1549–1552.

163. T. V. Chirila, Z. Barnard, Zainuddin, D. G. Harkin, I. R. Schwab, and L. W. Hirst, *Tissue Eng. Part A*, 2008, **14**, 1203–1211.

164. K. Higa and J. Shimazaki, *Cornea*, 2008, **27 Suppl 1**, S41–7.

165. E. S. Gil, S.-H. Park, J. Marchant, F. Omenetto, and D. L. Kaplan, *Macromol. Biosci.*, 2010, **10**, 664–73.

166. J. Wu, J. Rnjak-Kovacina, Y. Du, M. L. Funderburgh, D. L. Kaplan, and J. L. Funderburgh, *Biomaterials*, 2014, **35**, 3744–55.

167. B. D. Lawrence, Z. Pan, A. Liu, D. L. Kaplan, and M. I. Rosenblatt, *Acta Biomater.*, 2012, **8**, 3732–3743.

168. E. S. Gil, B. B. Mandal, S.-H. Park, J. K. Marchant, F. G. Omenetto, and D. L. Kaplan, *Biomaterials*, 2010, **31**, 8953–63.

169. F. P. Seib, G. T. Jones, J. Rnjak-Kovacina, Y. Lin, and D. L. Kaplan, *Adv. Healthc. Mater.*, 2013, **2**, 1606–11.

170. M. J. Dalby, N. Gadegaard, R. Tare, A. Andar, M. O. Riehle, P. Herzyk, C. D. W. Wilkinson, and R. O. C. Oreffo, *Nat. Mater.*, 2007, **6**, 997–1003.

171. T. J. Webster, R. W. Siegel, and R. Bizios, *Biomaterials*, 1999, **20**, 1221–7.

172. T. J. Webster, C. Ergun, R. H. Doremus, R. W. Siegel, and R. Bizios, *Biomaterials*, 2000, **21**, 1803–10.

173. P. Monti, G. Freddi, A. Bertoluzza, N. Kasai, and M. Tsukada, *J. Raman Spectrosc.*, 1998, **29**, 297–304.

174. P. Monti, P. Taddei, G. Freddi, T. Asakura, and M. Tsukada, *J. Raman Spectrosc.*, 2001, **32**, 103–107.

175. E. M. Pritchard, X. Hu, V. Finley, C. K. Kuo, and D. L. Kaplan, *Macromol. Biosci.*, 2013, **13**, 311–20.

176. R. C. Preda, G. Leisk, F. Omenetto, and D. L. Kaplan, *Methods Mol. Biol.*, 2013, **996**, 19–41.

177. Y. Cao and B. Wang, *Int. J. Mol. Sci.*, 2009, **10**, 1514–24.

178. T. Arai, G. Freddi, R. Innocenti, and M. Tsukada, *J. Appl. Polym. Sci.*, 2004, **91**, 2383–2390.

179. Y. Wang, D. D. Rudym, A. Walsh, L. Abrahamsen, H.-J. Kim, H. S. Kim, C. Kirker-Head, and D. L. Kaplan, *Biomaterials*, 2008, **29**, 3415–28.

180. J. Brown, C.-L. Lu, J. Coburn, and D. L. Kaplan, *Acta Biomater.*, 2015, **11**, 212–21.

181. X. Hu, K. Shmelev, L. Sun, E.-S. Gil, S.-H. Park, P. Cebe, and D. L. Kaplan, *Biomacromolecules*, 2011, **12**, 1686–96.

182. L. Zhou, X. Chen, Z. Shao, Y. Huang, and D. P. Knight, *J. Phys. Chem. B*, 2005, **109**, 16937–45.

183. A. S. Lammel, X. Hu, S.-H. H. Park, D. L. Kaplan, and T. R. Scheibel, *Biomaterials*, 2010, **31**, 4583–4591.

184. F. Meersman, C. M. Dobson, and K. Heremans, *Chem. Soc. Rev.*, 2006, **35**, 908–17.

185. N. Bhardwaj and S. C. Kundu, *Biotechnol. Adv.*, 2010, 28, 325–347.

186. F. Zhang, Q. Lu, J. Ming, H. Dou, Z. Liu, B. Zuo, M. Qin, F. Li, D. L. Kaplan, and X. Zhang, *J. Mater. Chem. B*, 2014, **2**, 3879.

187. N. Kojic, M. J. Panzer, G. G. Leisk, W. K. Raja, M. Kojic, and D. L. Kaplan, *Soft Matter*, 2012, 8, 6897.

188. R. Fourme, E. Girard, and K. Akasaka, *Curr. Opin. Struct. Biol.*, 2012, **22**, 636–42.

189. B. K. Shoichet, W. A. Baase, R. Kuroki, and B. W. Matthews, *Proc. Natl. Acad. Sci.*, 1995, **92**, 452–456.

190. C. Z. Zhou, F. Confalonieri, M. Jacquet, R. Perasso, Z. G. Li, and J. Janin, *Proteins*, 2001, **44**, 119–22.

191. J. O. Warwicker, *Trans. Faraday Soc.*, 1956, **52**, 554.

192. Z. Gong, L. Huang, Y. Yang, X. Chen, and Z. Shao, *Chem. Commun. (Camb).*, 2009, 7506–8.

193. A. Sinsawat, S. Putthanarat, Y. Magoshi, R. Pachter, and R. K. Eby, *Polymer (Guildf).*, 2002, **43**, 1323–1330.

194. R. Valluzzi and H.-J. Jin, *Biomacromolecules*, 2004, **5**, 696–703.

195. M. R. Nilsson, *Methods*, 2004, **34**, 151–60.

196. S. Thomas and Y. Weimin, *Advances in polymer processing*, Woodhead Publishing Limited, 2009.

197. O. S. Fleming and S. G. Kazarian, *Supercritical Carbon Dioxide*, Wiley-VCH Verlag GmbH & Co. KGaA, Weinheim, FRG, 2005.

198. X. Hu, D. Kaplan, and P. Cebe, *Macomolecules*, 2006, **39**, 6161–6170.

199. I. Cherny and E. Gazit, *Angew. Chem. Int. Ed. Engl.*, 2008, **47**, 4062–9.

200. S. H. Waterhouse and J. A. Gerrard, *Aust. J. Chem.*, 2004, **57**, 519.

201. L. J. Domigan, J. P. Healy, S. J. Meade, R. J. Blaikie, and J. A. Gerrard, *Biopolymers*, 2012, **97**, 123–33.

202. J. Torrent, M. T. Alvarez-Martinez, M.-C. Harricane, F. Heitz, J.-P. Liautard, C. Balny, and R. Lange, *Biochemistry*, 2004, **43**, 7162–70.

203. C. D. Wood, A. I. Cooper, and J. M. DeSimone, *Curr. Opin. Solid State Mater. Sci.*, 2004, **8**, 325–331.

204. A. Cooper, *Green Chem.*, 1999, **1**, G167–G168.

205. C. D. Wood, B. Tan, H. Zhang, and A. I. Cooper, *Thermodynamics, Solubility and Environmental Issues*, Elsevier, 2007.

206. M. Ashraf-Khorassani, L. T. Taylor, and P. Zimmerman, *Anal. Chem.*, 1990, **62**, 1177–1180.

207. M. Ashraf-Khorassani, L. T. Taylor, and P. Zimmerman, *Anal. Chem.*, 1990, **62**, 1177–1180.

208. X. Hu, D. Kaplan, and P. Cebe, *Macromolecules*, 2006, **39**, 6161–6170.

209. M. L. Floren, S. Spilimbergo, A. Motta, and C. Migliaresi, *Biomacromolecules*, 2012, **13**, 2060–2072.

210. M. Wang, K. Alberti, A. Varone, D. Pouli, I. Georgakoudi, and Q. Xu, *Adv. Healthc. Mater.*, 2014, **3**, 1398–403.

211. Q. M. Bian, S. Y. Chen, B. T. Kim, N. Leventis, H. B. Lu, Z. H. Chang, and S. T. Lei, *J. Non. Cryst. Solids*, 2011, **357**, 186–193.

212. H. Sun, Z. Xu, and C. Gao, *Adv. Mater.*, 2013, **25**, 2554–60.

213. Q. Lu, X. Hu, X. Wang, J. A. Kluge, S. Lu, P. Cebe, and D. L. Kaplan, *Acta Biomater.*, 2010, **6**, 1380–1387.

214. H. Perry, A. Gopinath, D. L. Kaplan, L. Dal Negro, and F. G. Omenetto, *Adv. Mater.*, 2008, **20**, 3070–3072.

215. H. J. Jin, J. Park, V. Karageorgiou, U. J. Kim, R. Valluzzi, P. Cebe, and D. L. Kaplan, *Adv. Funct. Mater.*, 2005, **15**, 1241–1247.

216. C. Zhao, J. Yao, H. Masuda, R. Kishore, and T. Asakura, *Biopolymers*, 2003, **69**, 253–9.

217. N. Hirota, K. Mizuno, and Y. Goto, *Protein Sci.*, 1997, **6**, 416–21.

218. Z. H. Zhu, *eXPRESS Polym. Lett.*, 2008, **2**, 885–889.

219. D. Roccatano, M. Fioroni, M. Zacharias, and G. Colombo, *Protein Sci.*, 2005, **14**, 2582–9.

220. G. S. Perrone, G. G. Leisk, T. J. Lo, J. E. Moreau, D. S. Haas, B. J. Papenburg, E. B. Golden, B. P. Partlow, S. E. Fox, A. M. S. Ibrahim, S. J. Lin, and D. L. Kaplan, *Nat. Commun.*, 2014, **5**, 3385.

221. B. P. Partlow, C. W. Hanna, J. Rnjak-Kovacina, J. E. Moreau, M. B. Applegate, K. A. Burke, B. Marelli, A. N. Mitropoulos, F. G. Omenetto, and D. L. Kaplan, *Adv. Funct. Mater.*, 2014, **24**, 4615–4624.

222. A. International, *ASTM Int.*, **13**.

223. P. G. Vekilov, A. R. Feeling-Taylor, S.-T. Yau, and D. Petsev, *Acta Crystallogr. Sect. D Biol. Crystallogr.*, 2002, **58**, 1611–1616.

224. M.-E. Rousseau, T. Lefèvre, L. Beaulieu, T. Asakura, and M. Pézolet, *Biomacromolecules*, 2004, **5**, 2247–57.

225. Y. Takahashi, M. Gehoh, and K. Yuzuriha, *Int. J. Biol. Macromol.*, 1999, **24**, 127–138.

226. C. Krywka, I. Krasnov, R. Figuli, M. Burghammer, and M. Müller, *Macromolecules*, 2014, **47**, 7187–7193.